Dynamics of Polariton Wave Packets

David Colas

Advisor
Dr. Fabrice P. Laussy

Committee

Prof. Carlos Tejedor.....UAM Madrid, Spain
Prof. Luis Viña.....UAM Madrid, Spain
Dr. Guillaume Malpuech.....UBP, Clermont-Ferrand, France
Dr. Nina Voronova.....MEPhI, Moscow
Pr. Juan Léon.....Instituto de Física Fundamental, Madrid

Universidad Autónoma de Madrid
Madrid, June 2016

The author can be contacted at davidcolas63000@gmail.com.

Tout hussard qui n'est pas mort à trente ans est un jean-foutre.
Antoine Charles Louis de Lasalle

Preface

In this manuscript I present the work I have done as a Ph. D student in theoretical physics. In September 2013, I came to Madrid to join the group of Dr. Fabrice P. Laussy in the department of theoretical condensed matter physics of the Universidad Autónoma de Madrid. During three years I have studied the polariton dynamics in various contexts.

I have work in collaboration of the experimental group of Daniele Sanvitto in Lecce, Italy, as part of the ERC Starting Grant POLAFLOW, to study the dynamics of microcavity polaritons.

Chapter 1 introduces the general topic but also discusses Research results that I did not elaborate upon in the thesis, to keep the unifying theme of a linear dynamics and/or because they are still work in progress. I invite the interested readers to the published (or to be published) literature for more details.

Chapter 2 gives a pedestrian introduction to the polaritons dynamics since it addresses their Rabi oscillations, that is well known by everybody working in this field, but with a level of details never achieved before, and this is what constitutes the original research of this first part.

Chapter 3 revisits the same physics but adding the polarization degree of freedom, with effect of proposing light pulses with a twist, namely, taking all the states of polarization during during their time duration (so-called "full Poincaré beams", but in time).

Chapter 4 is fully theoretical and introduces a new kind of wave packet, the Self-Interfering Packet (SIP), obtained by using the particular property of the lower polariton branch to have regions with both a positive and a negative effective mass. Spreading over these regions leads to a wave packet interfering with itself while propagating.

Chapter 5 contains the results of my last collaboration with the group of Lecce on the study of polariton vortices. These results are not published yet but are very promising. We have demonstrated and analysed theoretically the generation of precessing vortices powered by the Rabi oscillations.

During my thesis, I had the occasion to present my different results in several international conferences such as GEFES 2014 in Ciudad Real (Spain), PLMCN 2014 in Montpellier (France) and ICQT 2015 in Moscow (Russia).

Acknowledgements

Being in Spain during three years to do my Ph. D was an amazing experience and I have met so many great people that it looks difficult to establish an exhaustive list, but I will try to do my best. To start with, I would like to thank my thesis director, Fabrice P. Laussy, who gave me the opportunity to join his group in Madrid. We first met in Clermont-Ferrand (which looks like a key location in the polariton community) while I was still a master student in the group of Guillaume Malpuech. When he offered me a Ph. D position, he was so sick that I wondered if he would survive long enough to let me accept it, which I finally did less than a week after. Fabrice is an accomplished and talented scientist, and I am glad to have had the chance to work with him. He transmitted me strong physics knowledge as well as his addiction for chess. His biggest disappointment is probably that I still do not drink coffee, despite his repeated efforts to convert me during these three years. Being the only two Frenchmen of the department gave rise to endless debates on the French revolution during lunch at the cafeteria, whose I will remember for long. But also to some clashes, due to his exceptional ability to never recognize when he is wrong. I have, however, to admit that I share it a little bit as well, certainly a common Latin skill.

I also thank my colleagues and friends of the theoretical group of Madrid. Namely, "el señor Carlos Sánchez Muñoz Wolff", a very talented Ph. D student promised to a great scientific career (if he becomes a bit more self-confident). Elena del Valle, who had many times the hard task to balance Fabrice's opinions. Juan Camilo López Carreño, who will probably break the record of PRL published during one's Ph. D. The former members of the Madrid's group: Blanca, Juan Pablo, Dmitri, Guillermo. And a potential future member of the group: Julia, also known as "la Juge".

Bringing this work to fruition would not have been possible without my Italian colleagues from Lecce. The PolaFlow project and collaboration has been leaded masterfully by Daniele Sanvitto, who permanently knew how to motivate his troops. Most of the brilliant experiments that I had to analyse and model were conducted by Lorenzo Dominici. I specially thank him for the quality of the data he sent me and for the beautiful figures he made, I used some of them in the Chapters 1 and 5. I also had the chance to meet and work with the other members of the experimental group : Dario Ballarini, Milena de Giorgi, Stefano Donati and Giovanni Lerario. Grazie mille a tutti.

I am grateful to Professor Carlos Tejedor who has accepted to be the president of my jury, and to the other members: Prof. Luis Viña, Dr. Guillaume Malpuech, Dr. Nina Voronova and Prof. Juan Léon, who will have a long journey to come to Madrid for some of them.

Working in a good atmosphere is important for a scientist and officemates contribute a lot to this. I had the chance to share the "513" with Javi and Miguel, the two pillars of this office. Diego, an international chess Grandmaster (that I can only beat in hyperbullet games) who recently joined us. And former members of

the office, Ricardo and Santiago.

Coming to Madrid and the idea of leaving my home and birthplace, Clermont-Ferrand, was a bit stressful at the beginning, but once arrived, I rapidly encountered many friends from various horizons. Let me mention Agnieszka, Elise, Charlotte, Storm, Alexandra, Chloé, Kristina, Laura, Olga, Alessandra, Andrew, Matthias, Jan that I met the first year and with whom I had crazy times! During my second year, I met a second group of fantastic people with Andrea, Agata, Debora, Cristina, Catherine, Anna, Louis, Matteo, Manuel, Dario, Roberta and Cecile.

Even if I was far from my family during this time, they have always encouraged me to pursue my studies, providing me moral support and tasty Saint-Nectaire. I thank my good old friends from France who came to drink mojitos and visit me in Madrid: Matthieu, Jenny, Hélène, Christophe and Julie. I have a thought for Crina, who will always have a special place in my life. I apologize for those I probably forgot to mention here. Guys, I had a great time with all of you !

Madrid, June 2016

To my grandfather André.

Contents

List of Figures

Abstract

English

This thesis is devoted to the theoretical study of the exciton-polariton wave packets and present joint theoretical and experimental results regarding their Rabi oscillations, their propagation and combination thereof. Quantitative description of the experimental data through a dissipative quantum-optical model allows us to identify and quantify the main channels of decay (including upper-polariton dephasing and incoherent pumping from an excitonic reservoir) along with the coupling mechanism of the exciting laser to the structure. Upgrading the dynamics to polarized fields, we propose the concept for a device that generates light that takes all the states of polarization (Full-Poincaré beams), and implement it in the laboratory. In a purely theoretical exploration of the polariton packet dynamics, we introduce the notion of Self-Interfering Packets (SIP), that add a new member to the family of mechanisms that let particles emerge out of underlying fields, here powered by a mass-wall that folds back diffusion of the field onto itself. Finally, we consider the dynamics of vortices in coupled-fields and show the complex patterns of oscillations that result, both experimentally and theoretically.

Castellano

Esta tesis se ocupa del estudio teórico de los paquetes de ondas de polaritones de excitones, y en ella se presentan resultados teóricos y experimentales concernientes a sus oscilaciones de Rabi, su propagación, y combinaciones de ambas. La descripción cuantitativa de los datos experimentales, a partir de un modelo óptico-cuántico disipativo, nos ha permitido identificar y cuantificar los principales canales de decaimiento (incluyendo el dephasing del polariton superior y el bombeo incoherente desde un reservorio de excitones), así como los mecanismos por medio de los que un laser externo se acopla con la estructura. Al aumentar la complejidad en la dinámica de los campos involucrados, permitiendo que estos estén polarizados, hemos propuesto el concepto de un dispositivo que genera luz abarcando todos los estados de polarización (“haz completo de Poicaré”), y el cual hemos implementado en el laboratorio. De forma completamente teórica, hemos introducido la noción de Paquetes Auto-Interferentes (PAI), añadiendo un nuevo

mienbro a la familia de mecanismos a traves de los que partículas emergen de campos subyacentes, en este caso impulsado por un muro de masa que redirige el campo hacia sí mismo. Finalmente, hemos considerado la dinámica de vórtices en campos acoplados, y hemos mostrado tanto teórica como experimentalmente que de ellos surgen patrones complejos de oscilación.

List of acronyms

This is a list of the acronyms used in the text.

BEC	Bose Einstein Condensate
BS	Bright Soliton
DBR	Distributed Bragg Reflectors
DOP	Degree of Polarization
DS	Dark Soliton
FT	Fourier Transform
FWHM	full width at half maximum
GPE	Gross-Pitaevskii Equation
IFT	Inverse Fourier Transform
LCD	Liquid-Crystal Display
LG	Laguerre-Gauss
LMM	Levenberg–Marquardt Method
LP	Lower Polariton
LPB	Lower Polariton Branch
OAM	Orbital Angular Momentum
PRAXIS	Principal Axis Method
QED	Quantum Electro Dynamics
QW	Quantum Well
SE	Schrödinger Equation
SIP	Self-Interfering Packet
SOP	State of Polarization
STFT	Short-Time Fourier Transform
UP	Upper Polariton
UPB	Upper Polariton Branch
WDF	Wigner Distribution Function
WT	Wavelet Transform

Chapter 1

Introduction

Il n'y a pas de sciences ou de vertus
qui vaillent une goutte de sang.
Honoré de Balzac

Contents

In this introductory Chapter, we present the concept of exciton-polariton, and how these quasi particles composed of light and matter are produced in microcavities. Popular models to describe their behaviour are presented and we show some interesting phenomena arising the from non linearity in polariton systems.

1.1 Exciton Polaritons

A *Polariton* is a generic term that designates a quasiparticle arising from the coupling of an elementary excitation in solid state physics with a quantum of light (photon). This elementary excitation can be for example a phonon, which is an elementary excitation of a crystal and that can be pictured classically with a sound wave. In this case the coupling of light with such vibrating modes gives rise to phonon-polaritons. Another popular polariton is the plasmon-polariton, where the light is coupled to elementary excitation of the electron gas of the solid.

In this thesis, the term polariton stands for another kind of quasiparticles, the exciton-polariton. This arises from the interaction between a photon and a correlated electron-hole pair [2], also called exciton. This concept was introduced by J. J. Hopfield (1958) [3] describing the eigenstates of the system (excited bulk semiconductor) as "*mixtures of photons and excitons*". They are thus obtained by doing two types of quantization. First, a strong confinement of the light must be obtained in order to make it interact. This is achieved by engineering optical cavities into which the light can be trapped. Second, materials with a particular crystal structure has to be chosen to produce excitons. Semiconductor materials have revealed to be good platforms for that, but excitons can also be encountered in some insulators or organic materials.

Both of these two platforms can be engineered in a single semiconductor heterostructure. The epitaxy technology which follows a "bottom-up" approach, *i.e.* based on crystal growth, is now so well established and mastered that it allows the manufacturing of a rich variety of high quality structures.

1.1.1 Planar microcavities

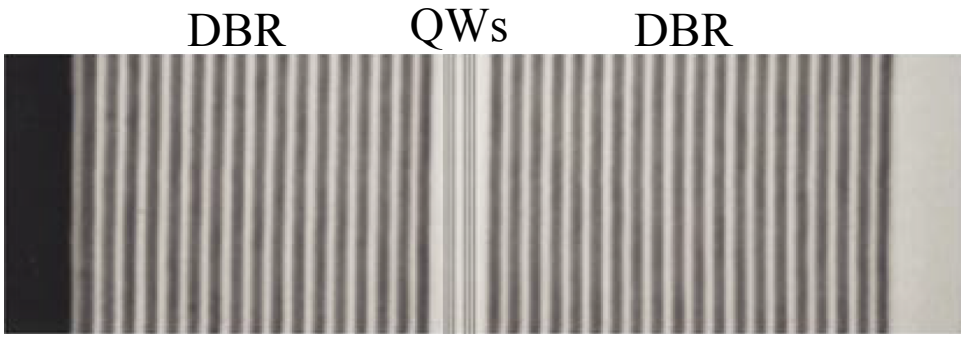

Figure 1.1: Scanning Electron Microscopy picture (from P. G. Savvidis and P. G. Lagoudakis (2003) [1]) of a typical semiconductor microcavity with DBR made of quarter-wave stacks of GaAlAs/AlAs layers.

The optical cavities in which the light is confined to obtain quantum effects are optical resonators whose dimensions are close to the wavelength of the light we want to trap. For submicrometer wavelengths, the common scheme is based on multilayer Distributed Bragg Mirrors (DBR). They consist in a succession of transparent surfaces with different refraction indices acting as ultra-high reflectivity mirrors (reflectivity can reach values $> 99,99\%$). A very efficient light confinement can thus be obtained by opposing two DBR, distant from a few wavelength of light, exactly like a classical Fabry-Pérot cavity. Various microcavity geometries can be designed (spherical, wires, pilars...) but we will focus on the most common ones used for polaritons, that are planar microcavities. This particular geometry provides cavity modes equally spaced in frequency.

A typical example example of a planar microcavity as viewed in electron mi-

croscopy is shown in Fig. 1.1. Two QWs are embedded between two DBRs made of quarter-wave stacks of GaAlAs/AlAs layers. The QWs are often made of III-V type semiconductors like $Al_xGa_{1-x}As$ layers. Various other semiconductors offering different properties such as higher band or different electric conductivity can also be used. As an example, there is an important research effort on the GaN-based microcavity to obtain an efficient polariton lasing at room temperature [4].

One important parameter for a cavity that will be of relevance in the following is its quality factor, which is defined as the ratio of the resonant cavity frequency ω_c and the linewidth of the cavity mode δ_{ω_c}:

$$Q = \omega_c / \delta_{\omega_c}. \tag{1.1}$$

This quantity is important since it measures the optical energy decay rate, in other words the quantity of light that leaks out of the cavity. The different decay sources will be of a particular interest in the different theoretical models we will develop to reproduce polariton experiments.

Quantum wells (QW) can be embedded between the two DBR and at the level of the optical modes to achieve the coupling between photons and excitons, which gives rise to the two new polariton modes when the photonic and excitonic modes are strongly coupled. This occurs when their Rabi splitting—the splitting between the new polariton modes—is greater than the linewidth of the cavity photon γ_C. On resonance, the polaritons are half-light and half-matter, and their wave function is a superposition of the bare states:

$$\psi_\pm = \frac{1}{\sqrt{2}}(\psi_C \pm \psi_X). \tag{1.2}$$

The first evidence of the *strong coupling* in a microcavity was brought by Weisbuch *et al.* (1992) [5]. This description above is the standard presentation of microcavity polaritons. I will show in next Chapter how a more accurate description of these objects is needed when getting at the bottom of their quantum dynamics.

1.1.2 Polariton condensates

Polaritons have bosonic statistics (both the constituting exciton and photon are bosonic) and exhibit the associated effects, starting with Bose stimulation as demonstrated by Savvidis in 2000 [6]. In 2006, the Bose–Einstein condensation of a gas of polaritons has been demonstrated by Kasprzak *et al.* (2006) [7]. This result is certainly the most important one for the field of polaritons, and the theoretical description of such a Bose–Einstein Condensate (BEC) out of equilibrium became one of the main stake of the community. Following this demonstration, various models based on a mean field approximation have been proposed. We will introduce some of the most popular ones in the next Chapter.

There has been some controversy on the terminology from the early days of the fields, since a BEC is a thermodynamical concept while polaritons are intrinsically

out-of-equilibrium particles which can be sustained in a steady-state by pumping. It remains accurate and adequate, however, to describe this out-of-equilibrium state through a coherent and macroscopically occupied polariton wave function. In this case, the minimalistic terminology of "condensate" can be used instead (of BEC), with the understanding that the object is a wave function ruled by a variant of Schrödinger equation (e.g., Gross-Pitaevskii equation when including interactions and turning to a mean-field approximation).

1.2 Nonlinear Phenomena in Quantum Fluids

Interactions are one of the most fascinating aspects and appealing characteristic of polaritons. Thanks to their mixed light-matter constitution, polaritons can benefit from the high coherence of the underlying photon at the same time as the strong interactions of the underlying exciton. This promises considerable improvements over photonic that suffers from weak photon-photon interactions, even in highly nonlinear crystals. In this thesis, I will in fact focus on the dynamics of non-interacting polaritons, leaving to other factors—in particular the dispersion, the polarization and external initial conditions—the role of bringing nontrivial physics. Interactions are, however, so important in polariton physics that one cannot study them without encountering them in one form or the other. I describe now some interesting phenomena that are based on such polariton nonlinearities and which I have encountered in the course of my own Research or that are relevant in the framework of this thesis.

First, a unique behaviour is observed at high pumping in the experimental implementation of the Rabi dynamics (covered at low pumping in Chapter 2). At high pumping, nonlinear effects become important and result in the formation of a "polariton backjet", described in the next paragraph.

Second, I will discuss on the relevance of nonlinearities in several experiments on dark solitons, since another controversy emerged in the field on whether an important phenomenology rooted on interactions could not in fact be described by a linear theory. Finally, I also overview a proposal to implement bright solitons generation, which is a work in progress at the time of writing and that also relies on nonlinearities, unlike the rest of the thesis.

1.2.1 Polariton Backjet

M. Vladimirova *et al.* (2010) [8] have analysed the different mechanisms that rule polariton-polariton interactions, mainly based on the exciton interactions (Van-der-Walls, direct and indirect exchanges). Polaritons are thus strong contenders in the field of quantum fluids, with various phenomena due to nonlinearities already demonstrated, including all the prevailing phases of strongly correlated systems: Bose-Einstein condensation, superfluidity and quantized vortices. Shock waves and solitons are other mainstream concepts induced by strong nonlinearities. How-

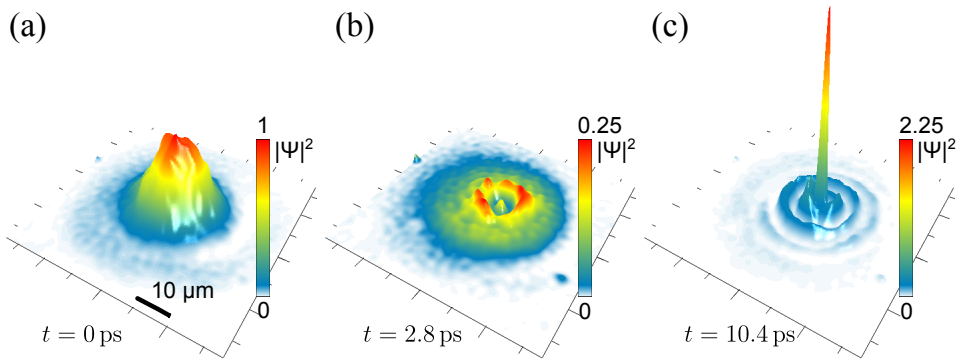

Figure 1.2: 3D view of the density map of the polariton fluid on a 80×80 μm area. The condensate is initially created from a 18.5 μm femtosecond pulse (a). The direction of the flow suddenly reverses to collapse the condensate (b) to later forms a robust and long living sharp peak in the center (c).

ever, and despite the previous observations, the time-resolved dynamics of such effects in strongly correlated gases remains largely unexplored. Polariton condensates differ from other analogues due to the particular dispersion relation they rely on, beside being intrinsically out-of-equilibrium with a very short lifetime. The latter allows to track their dynamics with high temporal resolution.

We reported in collaboration with the experimental group of Daniele Sanvitto in Lecce (Italy) a unique phenomenology that arises from a polariton condensate observed right after its formation in a very high excitation regime. The quantum fluid appears to be redistributed in space leading to a central localisation, going beyond 2 μm, which represents a reduction by one order of magnitude of the initial Gaussian spot injected to excite the cavity. The dynamics of the formation of such a "polariton backjet" (after the similar phenomenology observed by a droplet of water impinging on the surface of a liquid) is shown in Fig. 1.2. The three snapshots show the evolution of the condensate density at three characteristic moments of the backjet formation. Figure 1.2 (a) shows the initial condensate begotten by a 18.5 μm resonant femtosecond Gaussian spot. As expected, a Gaussian profile of the particles is observed. This then quickly collapses, as shown in Fig. 1.2(b) to finally produce a sharp peak at larger times, collecting the particles from the rest of the condensate despite their repulsive interactions, see Fig. 1.2(c). This sharp peak (the backjet) goes well below the initial span of the particles, and is in fact resolution limited. The phase gradient has also been measured and is inverted once the backjet forms, indicating a change of the fluid direction, from waves expanding outwards, to contracting towards the center. The bright peak has shown to be robust to decay, even if the global population has strongly decreased in time, and also when the initial beam is imparted with a momentum or also if the detuning is changed. Another interesting fact here, is that Rabi oscillations seem to play no role in the backjet formation, since essentially the same phenomenology is observed when only the LPB is excited. Furthermore, the backjet is accompanied by dark rings, exhibiting a π phase jump over the dark notches in the condensate den-

sity, suggesting interferences between counter propagating waves. No doubts exist about the nonlinear nature of this phenomenon, since the experiment has been also realized in the linear regime where also nontrivial and interesting phenomenology is observed—that will make the topic of Chapter 2—but that has nothing in common with the above features.

This phenomenon is deeply counter intuitive, since all the different mechanisms observed in previous experiments, such as the blueshift of the condensate or simply the polariton diffusion, support the interpretation of repulsive interactions, as is also predicted by the theory. The physical mechanism at the origin of the backjet is thus hard to explain. Polariton condensates are known to sustain both bright and dark solitons [9], dissipative solitons, moving solitons, etc. All these features are commonly reproduced by most of the models used to described polariton fluids. However, concerning the real-space collapse in the center of the spot, no similar mechanism has been reported in the literature. Various models have been tried in order to reproduce this particular feature but without giving entire satisfaction. We have nonetheless concluded that the most probable cause of the backjet would be the self-trapping of the polariton condensate by a type of collective polaron effect. This shows the potential complexity of the nonlinear physics of polariton fluids and that many mechanisms remain to understand the fluid reaches high-density and ultrafast dynamics. Further details can be found in the published version of this work in *Nature Communications*, see ref. 3 page 131.

1.2.2 The dark solitons controversy

The nonlinearity present in the polariton system is responsible for many strong phenomenologies, as we just seen with the polariton backjet. It has been shown by D. Sanvitto *et al.*(2010) [10] that polariton condensates can also sustain persistent currents and quantized vortices. Another particular feature due to the polariton-polariton interactions is the soliton. They can be generated when the polariton quantum fluid passes an obstacle, a defect in the cavity for instance.

Defects are usually due to a thickness inhomogeneities of the cavity layer, resulting in an attractive potential for the cavity mode. When the fluid velocity is higher than the speed of sound of the quantum gas, the perturbations induced by the defect lead to the emission of quantized vorticies and the nucleation of dark solitons (DS). In such a case, the speed of sound of the fluid directly depends on the interactions between the polaritons and the density via the relation $c_s = \sqrt{\hbar g|\psi|/m_{pol}}$, with g the polariton interaction constant and m_{pol} the polariton mass. A. Amo *et al.*(2011) [11] have reported the formation of oblique dark solitons for an interacting Bose gas of exciton-polaritons. A characteristic phase jump is present along the solitons. These objects have been widely studied theoretically, and extended to the case of spinor BECs, see H. Flayac *et al.* (2011) [12], with the predictions of oblique half solitons, new half integer topological defects. It has been later demonstrated experimentally by R. Hivet *et al.*(2012) [13] that these oblique half solitons could behave like one-dimensional magnetic monopole analogues. The

interaction between the present magnetic field, that arises from the TE-TM splitting in the microcavity, and the pseudo spin texture of the half-soliton leads to their acceleration in opposite direction. Bright solitons (BS) have also been generated in polariton systems by taking advantages of the polariton-polariton interactions. Such behaviours have been reported by A. Amo *et al.*(2009), showing a polariton wave packet with a linear dispersion relation, travelling at high speed and without diffusion. Other experiments have been conducted by the groups of D. Skryabin and M.S. Skolnick showing various cases of bright soliton formation, one can refers to O. A. Egorov *et al.* (2009) [14] and M. Sich *et al.*(2012) [15] and (2014) [16]. The technique used consists in exciting the lower polariton branch around its inflection point, playing on the interplay between the negative effective mass of the polaritons in this region, and the repulsives interactions between them. All of this rich phenomenology has been reproduced theoretically by using Gross-Pitaevskii Equations (GPE), eventually coupled, thus including nonlinear terms.

In 2015, a paper published by P. Cilibrizzi *et al.*(2015) [17] in *Physical Review Letters* brought a controversy in the polariton community. The authors claimed that DS and half DS can be obtained in the linear regime of excitation. Similar features ("*identical qualitative features*") than those obtained in nonlinear systems were observed, such as phase jumps and related intensity profiles. The polaritons were created in a cavity presenting a large detuning and at low pumping, insuring a small excitation fraction and thus avoiding the influence of the interactions. The fluid passing the defect, the generation of depth-preserved and propagating dark notches was observed. These dark and bright traces are accompanied by a particular phase pattern with including phase jump along the traces that result from interferences created by the beam scattering on the defect. These experimental observations have been reproduced with a linear model based the Maxwell equations. All these observations led the authors to invite the community to reconsider the previous results obtained on DSs [11, 13].

A comment signed by fourteen renowned experimentalists and theoreticians from different polariton leading groups was published to challenge the main conclusions of Cilibrizzi *et al.*. A. Amo *et al.*(2015) [18] have reminded that DS appear as solutions of the GPE exhibiting an oblique dark intensity line following the defect, with an abrupt phase jump. Theses solutions can be derived analytically from the GPE [19]. They are expected to appear in the quantum fluid only if the flow velocity is $v_{flow} > c_s$, where the sound velocity depends explicitly on the density. Below this value, other phenomena due to superfluidity occur. This set of conditions is required for the DS generation establishing it as an intrinsic nonlinear object. However, the authors mention that independent features can of course be observed in the linear system and point out that quantitative difference are here present with previous studies, notably in the evolution of the DS width. They conclude that dark traces presenting phase jumps are not an exclusive feature of soliton physics.

In the Cilibrizzi *et al.*(2015) [20] reply, the authors suggest that more experimental evidences should be brought to avoid the ambiguity on the soliton nature,

the previous works showing DS being realised in different conditions. Accurate analysis based on the density and its variation should be done systematically, since it defines the healing length of the solitons and the speed of sound in the condensate.

This interesting debate that shook the polariton community for a year brings important questions. All of the authors of the previous works agree on the fact that the GPE admits solitonic (DS and BS) solutions. Their opinion differs on what is really observed experimentally. An object presenting solitonic features in the linear regime may thus not be considered as a proper soliton. But in the same way, how to be sure that a similar object (with the same features) observed in the nonlinear regime is a soliton and that its features are due to the nonlinearity? In Chapter 4 of this thesis, we show that intriguing solutions behaving with many respect as solitonic objects can be obtained with polaritons in the linear regime. We show that Self Interfering Packets are produced by spreading over the mass divergence of the LPB, *i.e.*, at its inflection point. The typical diffusion cancellation is obtained similarly to bright soliton cases and phase jumps are also observed, which are in this case dislocation lines arising from an interferences phenomenon in the sense of Berry.

1.2.3 Multiple bright soliton generation

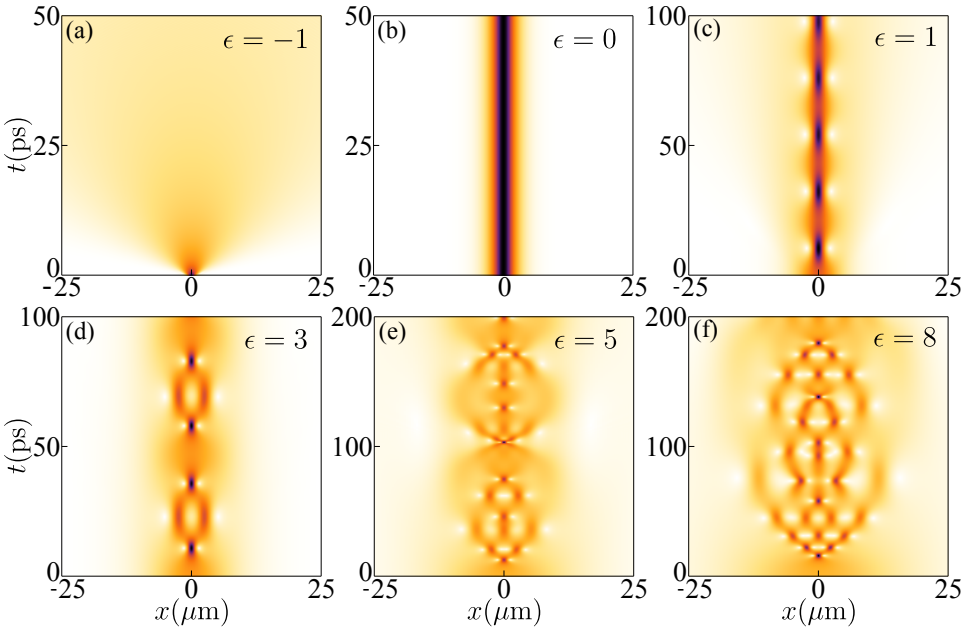

Figure 1.3: Free propagation of quenched bright solitons, using different initial conditions for the 1D-GPE. (a) Shrink soliton, exhibiting the diffusive dynamics of a regular wave packet. (b) Original solitonic solution ($\varepsilon = 0$). (c-f) Stretched solitons as initial condition. The wave function shrinks into a bright peak and then can exhibit more complex oscillations.

To keep going with the solitons, I now introduce a proposal I made during my Ph. D studies and which consists in the generation of multiple bright solitons from a single beam. Working in a nonlinear medium with attractive interactions between the particles, we send a wave packet whose size was initially quenched in order to generate a breathing/oscillating solution against a potential wall. After bouncing on the potential, the wave packet splits in a train of bright solitons with different velocities, the number of produced solitons depending on the initial quench. This work has not been published at the time of presenting this thesis and it will therefore be succinctly described there rather than as an extended Chapter like the rest of my results.

We start with a Bose-Einsten condensate described by the 1D-Gross-Pitaevskii Equation:

$$i\hbar\partial_t\psi = \frac{-\hbar^2}{2m}\partial_x^2\psi + V(x) + g|\psi|^2\psi\,, \tag{1.3}$$

where m is the mass of the particles which are interacting via the coupling constant g and in the presence of an external potential V.

It is established that depending on the sign of the interaction between particles g, different solitonic solutions can be found [19]. In the case of $g > 0$, which means considering repulsive interactions between the particles, dark solitons solutions are obtained. The DS solution reads :

$$\psi(x-vt) = \sqrt{n}(i\beta + \gamma\tanh\left[\gamma\frac{x-vt}{\sqrt{2}\xi}\right])\,, \tag{1.4}$$

where $\beta = v/c$ is the reduced speed, $\gamma = \sqrt{1-\beta^2}$ the Lorentz factor, $\xi = \sqrt{\hbar^2/2mgn}$ is the healing length and $n = |\psi|^2$ is the density of the condensate. DSs present a maximal phase change of π at the density minimum.

In the case of attractive interactions, *i.e* by setting $g < 0$ in the GPE, bright soliton solutions are obtained. Unlike DS, where the soliton consists in a depletion of particles in the condensate density due to their repulsion, the BS features a bright peak in the density. In this case, the wave function is found to be :

$$\psi(x) = \mathrm{sech}(x/\sqrt{2}\xi)\,, \tag{1.5}$$

with the corresponding healing length $\xi = \sqrt{\hbar^2/2m|g|n}$. As a soliton, this packet is shape-preserved in time. A different dynamics could be expected in the case of a quenched bright soliton. The quench dynamics of solitons have already been studied for some cases. We can mention the work by O. Gamayun *et al.*(2015)[21] in which the authors have considered the case of dark and grey solitons (*i.e.* a DS without a full depletion) with a sudden quench on the non linearity parameter. They found that after the quench, a single DS can splits in different dark and grey solitons. This allows the creation of multiple solitons that could be used for protocol in fiber optic devices for the replication of optical signals. Another similar study has been done by quenching the interaction parameter [22] and similar behaviours were found.

Instead of acting directly on the interaction constant g, which can be difficult to achieve experimentally in certain systems, the quenching can be done simply by acting on the size of the initial wave packet. We have solved the GPE considering attractive interactions ($g = -0.2$). We put as initial condition a bright soliton in which we introduce an extra term to modify its size. Our new ansatz thus reads:

$$\psi_\varepsilon(x) = \mathrm{sech}(x/(\sqrt{2}\xi + \varepsilon)), \tag{1.6}$$

with $\varepsilon \neq -\sqrt{2}\xi$. Cases for different values of ε are presented in Fig. 1.3. When $\varepsilon < 0$, the initial size of the soliton is smaller and behaves like a diffusive Gaussian wave packet, as seen in Fig. 1.3(a). When $\varepsilon > 0$, the initial soliton is larger and shows a self-localisation, similarly to a wave packet in a harmonic potential, see Fig. 1.3(c). Similar features, like a simple soliton breather, have been observed in previous theoretical studies [23, 24]. One can increase again the initial size of the soliton, as done in Fig. 1.3(d). After a first shrinkage, the wave function then splits into two other peaks. This behaviours repeats in time, the wave function presenting successively one sharp peak and two less sharp peaks, before coming back to its initial shape. More complicated oscillation patterns can be obtained by taking even largest initial beams, see Fig. 1.3(e,f). For $\varepsilon = 8$, up to four sharp peaks are produced at the same time while the function oscillates.

The breathing solitons and multiple-soliton oscillations presented in Fig 1.3 preserve their shape if the initial wave packet is imparted with a momentum k_0. However, unlike the single soliton solution, the shape of the wave function does not remain the same after colliding against a potential (a Gaussian potential in the present case). Instead, it disperses in multiple solitons. Cases for $\varepsilon = 2, 5$ and 8 are plotted in Fig. 1.4(a,c,e). It seems that it exists a correlation between the size of the initial wave packet and the number of soliton produced after meeting the potential wall, more solitons being produced when the initial packet is larger. The nature of the newly produced bright solitons can be confirmed by looking at the wave function in the Energy-Momentum space ($\psi(k, E)$). Each soliton features a linear dispersion red shifted from the parabolic dispersion of the particles, see Fig. 1.4(b,d,f). We see as well that the solitons travel with different velocities, creating a bright soliton train. All of the different solitons can be fitted at large time by a $\mathrm{sech}(x)$ function. This suggests that the initial oscillating wave packet was in fact in a superposition of many different bright soliton states.

Analytical solutions for such a system can usually be obtained by moving to the Fourier space. Thus it could be interesting to search for analytical solutions since the Fourier Transforms of the initial conditions that we have used are easy to obtain:

$$\mathscr{F}_k(\psi(x)) = \sqrt{\pi}\xi\,\mathrm{sech}(k\pi\xi/\sqrt{2}), \tag{1.7}$$

$$\mathscr{F}_k(\psi_\varepsilon(x)) = \sqrt{\frac{\pi}{2}}(\sqrt{2}\xi + \varepsilon)\,\mathrm{sech}(\frac{1}{2}k\pi(\sqrt{2}\xi + \varepsilon)), \tag{1.8}$$

This system is also interesting from a numerical point of view. For the numerical resolution of the GPE, we have used a split-step Fourier method [25], and it appeared quite hard to obtain a good convergence of the solution. The wave function

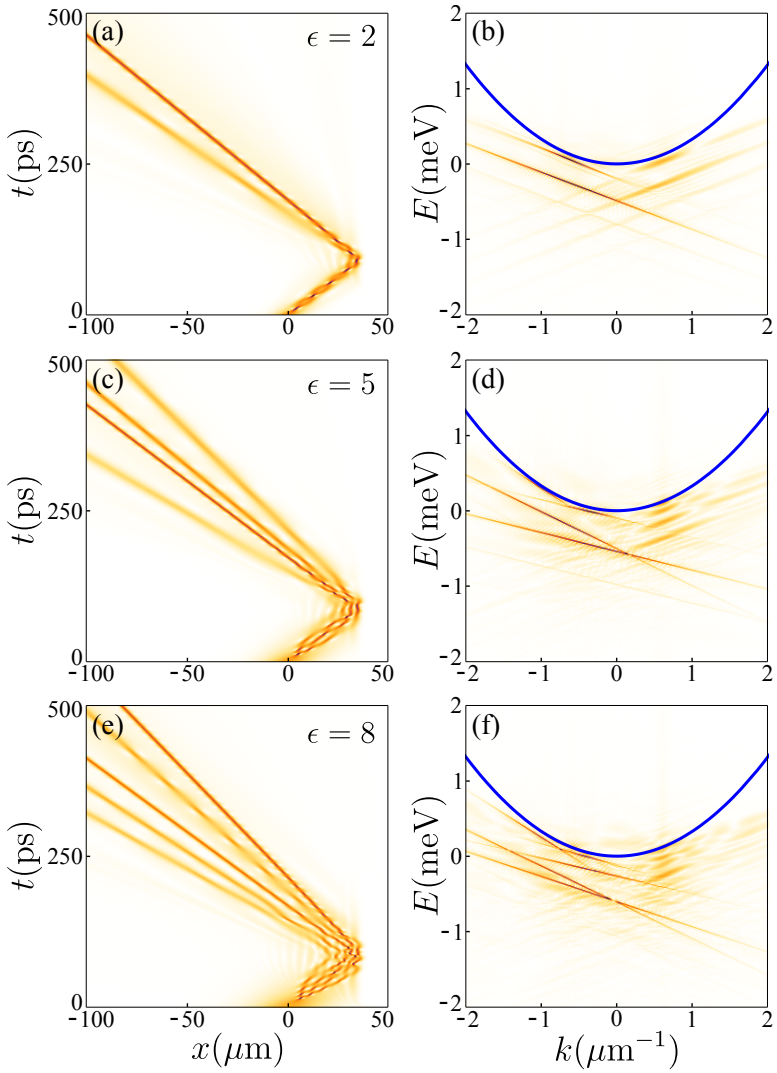

Figure 1.4: (Color online) The collision of the interfering solitons over a potential barrier (here a Gaussian one, center at $x = 50$ µm) splits and disperse the initial packet in a set of bright solitons with different velocities. Left column: space-time propagation for different ϵ. Right column: corresponding dispersion.

self-interaction leads to fast oscillations that present sharp peaks (Fig. 1.2), themselves increasing the local density and being thus a source of numerical instability. Such a case can thus be a good choice to test the robustness of a GPE algorithm.

For a practical implementation, soliton tains can find applications for high-speed optical signal modulation and information coding [26, 27]. A similar idea was used by Y. Zhang *et. al*(2014) [28] where the solitons are produced from interacting Airy beams.

1.3 Summary of contents

The rest of this thesis is organised as followed:

In Chapter 2, we study the polariton Rabi dynamics through a joint theory-experiment approach, under conditions of coherent control by external pulses. We take into account all sources of pumping, decay and dephasing and show through an essentially perfect agreement between the theory and data that the polariton dynamics in the linear regime is completely understood, with some nontrivial effects (such as lifetime-enhancement of the Rabi oscillations through the exciton reservoir). The theory consists in a quantum optical model based on the Linblad formalism. It shows that the polariton dynamics is really that of coupled condensates rather than the usual picture (given above in this introduction, Eq. (1.2)) of a linear superposition of the bare states. We will see as well how the theory allows us to go beyond the experiment and get the full picture of the field dynamics. It confirms that while polaritons remain highly coherent throughout, the upper polaritons are short-lived as they suffer from their own decay channel, independently of that inherited from the bare states lifetimes. The analysis of the experiment also shows that the impinging laser couples not only to the cavity but also directly to the exciton field.

The Chapter 3 is devoted to a similar experiment based on the polariton Rabi oscillations, but this time adding the polarization as a new degree of freedom. We see how the dynamics that results from a combination of polarization and Rabi oscillations yields a new type of light with a time varying polarization that is able, in some conditions, to span the Poincaré sphere, leading to the concept of "temporal full Poincaré beams". This brings together two topical concepts in modern light-engineering, namely "pulse-shaping" (fixing the dynamics of the polarization in time) and "full Poincaré beams" (beams that take all the states of polarization in space). An updated version of our quantum optical model is developed to incorporate the polarization and describe the states that are now accessible. The control of the polarization trajectories on the Poincaré sphere can be fully controlled theoretically by setting a proper initial state. This makes the scheme simple and platform-independent, allowing its implementations for different types of fields and with different timescales. This time, the strong influence of decay and dephasing of the upper polariton on this dynamics is used as an asset, rather than being detrimental. Experimental cases are also presented.

Chapter 4 is purely theoretical, and presents a full-fledged study on a new kind of wave packets, that I call Self-Interfering Packets (SIP). It has long been advertised in the polariton community that the peculiar polariton dispersion is mother to a series of interesting effects. We see indeed that the property of the lower polariton branch of having regions with positive and negative effective mass can lead to the propagation of polariton packet exhibiting self-interferences. Other striking differences due to a non-parabolic dispersion for the particles motion are discussed in details, including finite speeds, limited diffusion and simultaneous localisation of the bare states, etc. Combined with the Rabi oscillations, when the system is

not prepared in an eigenstate, the wave function orders into a honeycomb lattice in space and time. Analytical solution of these different packets are proposed and their structures is studied through different momentum-space representations. The SIP appears to be a new member in the family of mechanisms that embody particles out of fields (along with solitons and self-accelerating wavepackets). The realisation of self interfering packets in realistic system is discussed.

In Chapter 5, we come back to results obtained in collaboration with experimentalists, to present and describe an other striking dynamics observed in Lecce, namely, the generation of Rabi oscillating vortices. We derive the vortex solutions for the uncoupled system and implement the polariton vortex ones for the coupled system, taking into account the decay/dephasing sources. Since the vortex oscillations seem powered by the Rabi oscillations, we investigate the effective coupling between the vortex angular momentum and the Rabi coupling. Interesting effects are theoretically proposed on the propagation and the separation of vortices in the two polaritonic components. Such predictions are then qualitatively retrieved experimentally. At the time of writing, these results are not yet published but their elegance and novelty will no doubt be recognized by the reader, in addition to provide a unifying picture to all the previous Chapters.

In Chapter 6, we summarise the main results of this thesis and draw its main conclusions.

Chapter 2

Rabi Dynamics of Polaritons

L'imagination gouverne le monde.
Napoléon Bonaparte.

Contents

In this Chapter, we study some of the main properties of polaritons: their spacetime dynamics as wave packets, and their Rabi oscillations as coupled states. The first study is pursued using the classical formalism of coupled Schrödinger equations while we have developed a simple optical model based on the Lindblad formalism to describe the coherent control of the Rabi oscillations which was realised experimentally by my colleagues in Lecce. The results presented gave rise to a publicaton in the *Physical Review Letters*, see ref 1 page 131.

2.1 Introduction

Rabi oscillations were initially observed in atomic systems where they have been described by I.I. Rabi (1937) [29]. Later generalised to any quantum two-level system, they have found a particular echo in quantum optics and condensed matter since they are the basic process in the qubits manipulation. The control of the Rabi oscillation is thus expected to be a crucial task for quantum computation. They are the embodiment of quantum interactions: when a system a is excited and is coupled to a second system b, the excitation is transferred from a to b and when the symmetric situation is established, the excitation comes back in a cyclical unitary flow. In a quantum setting, such an oscillation is of probability amplitudes and generates entangled states. The same physics also holds with coherent states of the fields, a situation known in the literature as implementing an "optical atom" [30] or a "classical two-level system" [31]. The oscillation is then more properly qualified as "normal mode coupling" [32, 33] as it is now between the fields themselves.

In the beginning of 2014, our experimentalist co-workers in Lecce provided us with impressive data on coherent control of Rabi oscillations in a polariton microcavity. Their experiment consisted in sending a series of pulses onto the microcavity in order to bring the system in any desired state, by controlling different parameters such as the time delay between the pulses or their relative frequency.

To describe this experiment, we have developed an optical model based on the Lindblad formalism to include all the different dephasing mechanisms involved. Since we were focusing on the Rabi oscillations analysis, and considering that the space dynamics is not playing a significant role, the theory reduces to a 0-dimensional and therefore simple model that admits largely analytical solutions. Beside, the model is suitable both at the quantum and classical levels. We will see in Chapter 4 other configurations where the space dynamics leads to interesting effects. With this work, we show the tremendous control that can be obtained on the light-matter coupling in microcavities, and we bring the first imaging of its spatio-temporal evolution, coherently controlled at the femtosecond level.

The Chapter is organised in the following way. In Section 2.2, we introduce the main models used to describe the polaritons, giving a short overview of the popular ones. In Section 2.3 we present the optical model we have used to fit the data of the coherent control of Rabi oscillations experiment performed in Lecce. We show how the different states that can be obtained in such a system and how the pulses dynamics is treated. An important discussion concerns how to take into account the various sources of decay and dephasing, using the Lindblad formalism. We show as well how the quantum state of the polariton can be represented in a convenient way on the Bloch Sphere or by using the Husimi quasiprobability distribution.

Section 2.4 is devoted to the experimental results. We first bring more details on the experimental setup and the techniques used for the data acquisition. We then come to the results of the one-pulse and two-pulses experiments.

Section 2.5, called "Theoretical Extents", we provide additional materials obtained theoretically and by using the physical parameters previously fitted from the

experimental data. We show the particular effect of the upper polariton dephasing on the population. We then complete the picture of the two-pulses experiment by showing the four-fields dynamics, which is not possible with the experiment alone, only the photonic field being accessible.

The main conclusions of this Chapter are given in Section 2.6.

2.2 Spacetime dynamics

In this Section, we introduce the most popular formalisms to describe Polaritons, giving a short overview of the models most commonly used by the community.

2.2.1 Polariton formalism

Polaritons in the linear regime of excitation are well described by the physics of two-coupled Schrödinger Equations [2], which in real space read:

$$i\hbar\partial_t = -\frac{\hbar^2}{2m_\mathrm{C}}\nabla^2\psi_\mathrm{C} + \frac{\hbar\Omega_\mathrm{R}}{2}\psi_\mathrm{X}\,, \tag{2.1a}$$

$$i\hbar\partial_t = -\frac{\hbar^2}{2m_\mathrm{X}}\nabla^2\psi_\mathrm{X} + \frac{\hbar\Omega_\mathrm{R}}{2}\psi_\mathrm{C}\,, \tag{2.1b}$$

where the photonic field ψ_C and the excitonic field ψ_X are linearly coupled at the Rabi frequency Ω_R, $m_{\mathrm{C,X}}$ being the mass of the particles for each field. They can be described equivalently in the reciprocal space:

$$i\partial_t\begin{pmatrix}\psi_\mathrm{C}\\ \psi_\mathrm{X}\end{pmatrix} = \begin{pmatrix}\frac{\hbar\boldsymbol{k}^2}{2m_\mathrm{C}} & \frac{\Omega_\mathrm{R}}{2}\\ \frac{\Omega_\mathrm{R}}{2} & \frac{\hbar\boldsymbol{k}^2}{2m_\mathrm{X}}\end{pmatrix}\begin{pmatrix}\psi_\mathrm{C}\\ \psi_\mathrm{X}\end{pmatrix}. \tag{2.2}$$

This representation is perhaps more intuitive, in the sense that the operators in this basis are c-numbers (k^2) rather than differentials (∇^2) which turns the Hamiltonian $\mathbf{H}$ (the 2×2 matrix in Eq. 2.2) into a conventional matrix where the coupling between the bare fields appears on the off-diagonal elements (Ω_R). The diagonalization of this Hamiltonian gives us directly the two branches of the polariton dispersion:

$$E_\pm = \frac{\hbar k^2(m_\mathrm{C}+m_\mathrm{X})}{m_\mathrm{C}m_\mathrm{X}} \pm \sqrt{\left(\frac{\Omega_\mathrm{R}}{2}\right)^2 + \left(\frac{\hbar k^2(m_\mathrm{C}-m_\mathrm{X})}{4m_\mathrm{C}m_\mathrm{X}}\right)^2}\,, \tag{2.3}$$

the sign "+" and "-" referring to the Upper Polariton Branch (UPB) and the Lower Polariton Branch (LPB), respectively.

Equation 2.2 can be formally integrated as:

$$\boldsymbol{\psi} = e^{-i\mathbf{H}t}\boldsymbol{\psi}_0\,, \tag{2.4}$$

where the solution $\boldsymbol{\psi} = (\psi_\mathrm{C}, \psi_\mathrm{X})^\mathrm{T}$ is the product of the matrix exponential of the Hamiltonian with the initial condition $\boldsymbol{\psi}_0 = (\psi_\mathrm{C}(t=0), \psi_\mathrm{X}(t=0))^\mathrm{T}$. The wave

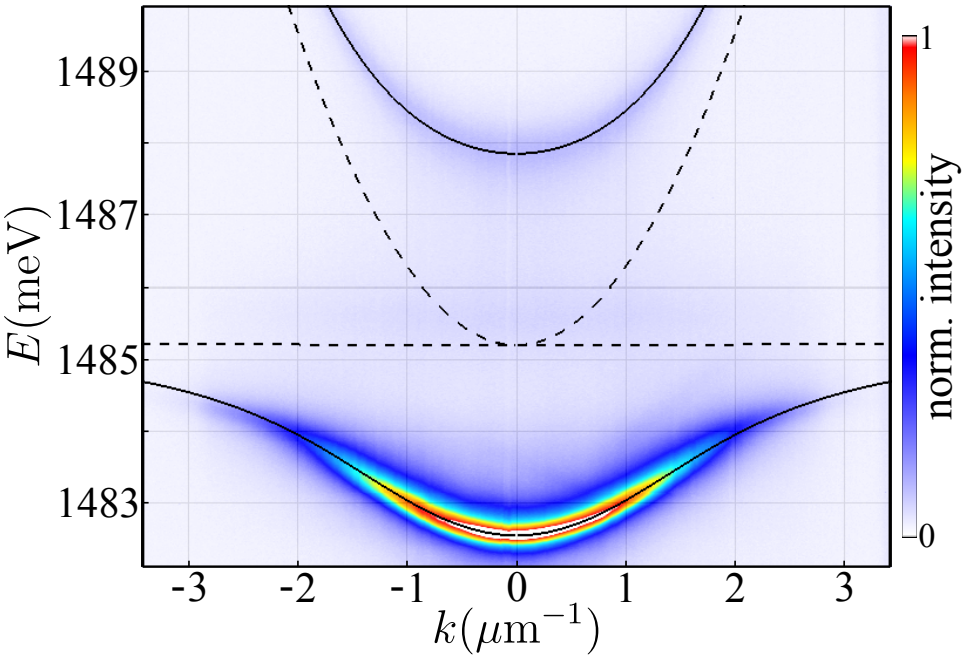

Figure 2.1: In dashed lines are plotted the parabolic dispersion of the bare states. The exciton dispersion is flat compared to the photon one, due to its high effective mass. In full lines are plotted the polaritons branches, the lower polariton dispersion (LPB) and the upper polariton dispersion (UPB). The theoretical lines were adjusted to fit the experimental dispersion.

function dynamics in the real space can thus be easily recovered by applying the Fourier Transform (FT) on its k-components. In the same way, one gets access to the far field (like in Fig. 2.1) by applying the FT on the temporal part of the wave function. The most common and simple way to excite the polariton system experimentally is to shine a laser onto the top of the cavity. Thus, the excitation that acts on the photonic field, which is not an eigenstate of the system, is expected to induce Rabi oscillations, *i.e.* a beating between both fields ψ_C and ψ_X.

More complex and elaborated models have been developed to describe the formation of a polariton condensate out of equilibrium. The most popular one was proposed by Michiel Wouters and Iacopo Carusotto in 2007 [34]. The polariton condensate is described with a macroscopic wave function $\psi(\boldsymbol{r})$ which follows a Gross-Pitaevskii Equation (GPE):

$$i\partial_t\psi = \left(-\frac{\hbar\nabla^2}{2m_{\mathrm{LP}}} + \frac{i}{2}(R(n_{\mathrm{R}}) - \gamma) + g|\psi|^2 + 2\widetilde{g}n_{\mathrm{R}}\right)\psi\,. \tag{2.5}$$

Here, Wouters and Carusotto approximated the LPB with a parabolic dispersion of mass m_{LP}. The decay rate of the particle γ is momentum-independent. The main difference with the Schrödinger Equation consists in the introduction of the non linear term $g|\psi|^2$, describing the polariton-polariton interactions, with g the interaction strength between the particles. As mentioned in the Chapter 1, these

interactions generate a rich phenomenology and a wide range of effects in the polariton systems. The real novelty of this model comes from the introduction of a polariton reservoir n_R, that couples the wave function of the coherent condensate ψ, with a strength $\widetilde{g}$. The polariton reservoir obeys its own dynamics:

$$\partial_t n_R = P - \gamma_R n_R - R(n_R)|\psi|^2 + D\nabla^2 n_R\,, \tag{2.6}$$

that includes a pumping rate P, a decay rate γ_R and a spatial diffusion rate D of the polaritons of the reservoir. Both Eqs. 2.5 and 2.6 include an amplification rate $R(n_R)$ of the condensate describing the stimulated scattering of the polaritons from the reservoir. It is also common to find in the literature the equivalent model written with two coupled-GPE for the photonic and excitonic fields, avoiding the parabolic approximation. This mean field description has proven its accuracy to describe the formation of the polariton condensate.

Another notable model, more recent and that extends the previous one came from D.D. Solnyshkov *et al.* (2014) [35] under the form of an hybrid Boltzmann–Gross-Pitaevskii equation, that describes the Bose-Einstein condensation of a generic driven-dissipative system. The authors used semi-classical rates to describe the coupling between the condensate and the reservoir. This model has, for example, the advantage of describing the condensate superfluidity more accurately than a standard Ginzburg-Landau model.

In the next Section, I introduce a quantum optical model suitable to describe a single-mode only, but, in particular, to describe its quantum state beyond mean-field. Even when the system will remain classical throughout, this allows to describes simply and elegantly the coherence of the system, which is crucial in this sort of experiment.

2.3 Quantum Polariton Dynamics

Equations 2.1 and 2.2 only provide a naked picture of the polariton physics and ignore most of the ingredients present in a realistic experiment, such as the lifetime of the different particles, the optical pumping, the temporal profile of the exciting pulses, the relaxation processes etc. Furthermore, the Wouters-Carussoto types of models are cumbersome when no particular spatial dynamics is involved and when the system is in the linear regime, hiding the relevant physical ingredients with a heavy formalism. In this Section, I present an elegant quantum-optical model that we have developed to fit the experiment done by the experimentalists in Lecce on the Rabi oscillations control. In order to include the physics intrinsic to the experiment (laser pulses, decay sources, etc.), we use the convenient Lindblad formalism. Useful representations of the quantum state evolution on the Bloch Sphere or through the Husimi quasiprobability distribution are also provided.

2.3.1 Quantum Optical Model

The experiment performed in Lecce does not involve the propagation of packets by imparting momentum. Thus, even if the different wave functions we are dealing with have an extension in both real and reciprocal spaces, the system remains linear and there is no significant dynamics induced by the spatial degrees of freedom. Thus, the polariton dynamics can be reduced to a zero dimensional problem between two single harmonic modes. The oscillations of the fields are fully captured through the simpler order parameters:

$$\langle a(t)\rangle = \langle\psi|a|\psi\rangle = \int \psi_{\mathrm{C}}(\boldsymbol{r},t)\mathrm{d}\boldsymbol{r}, \tag{2.7a}$$

$$\langle b(t)\rangle = \langle\psi|b|\psi\rangle = \int \psi_{\mathrm{X}}(\boldsymbol{r},t)\mathrm{d}\boldsymbol{r}. \tag{2.7b}$$

The Hamiltonian describing these coupled modes is:

$$H_0 = \hbar\omega_0(a^\dagger a + b^\dagger b) + \frac{\hbar\Omega_{\mathrm{R}}}{2}(a^\dagger b + ab^\dagger), \tag{2.8}$$

where Ω_{R} stands for the Rabi coupling strength between the photonic mode a and the excitonic mode b, with the commutation relation $[c,c^\dagger] = 1$, for both $c = a,b$. The two bosonic modes are excited resonantly at the energy ω_0. In order to describe the dynamics of two linearly coupled oscillators from a quantum point of view, one has to take into account the various quantum states responsible for the oscillations pattern. To do so, let us consider the wave function as an infinite linear combination of Fock states, weighted by a set of coefficients $|nm\rangle$, containing n quanta of excitation in the oscillator a and m in the oscillator b, it reads:

$$|\psi(t)\rangle = \sum_{n,m=0}^{\infty} \alpha_{nm}(t)\,|nm\rangle\,. \tag{2.9}$$

However, looking only at the coherent states reduces the previous expression to two complex numbers:

$$|\psi(t)\rangle = |\alpha(t)\rangle\,|\beta(t)\rangle\,. \tag{2.10}$$

This assumption makes sense in the present case as the experiment we are describing involves essentially coherent states. Indeed, the system is excited resonantly by a laser pulse creating coherent states. It was found *a posteriori* that the dephasing has a small impact, given the large population and the short time durations involved. We will address this point more in details in Section 2.5.1.

The excitation scheme is provided by the following Hamiltonian:

$$H_\Omega = \sum_{c=a,b} P_c(t)e^{i\omega_{\mathrm{L}}t}e^{i\phi_c}c^\dagger + \mathrm{h.c.}, \tag{2.11}$$

where the pulses $P_c(t)$ are sent at the laser frequency ω_{L} and carrying a phase ϕ_c, with $c = a,b$. The total Hamiltonian of the system is thus expressed as:

$$H = H_0 + H_\Omega\,. \tag{2.12}$$

The system can be solved from the vacuum, sending a first pulse to trigger its dynamics. As we are mainly interested in the effect of the pulse on an ongoing dynamics, it is also possible to solve it for a given initial condition (assumed prepared by a previous pulse acting on, say, the vacuum):

$$|\psi(t=0)\rangle = |\alpha(0)\rangle|\beta(0)\rangle\,, \tag{2.13}$$

where $\alpha_0, \beta_0 \in \mathbb{C}$ (possibly zero). The states $\alpha(t)$ and $\beta(t)$ can be thus obtained by solving the Schrödinger equation $i\hbar\partial_t\psi = H\psi$ with the Hamiltonian of Eq. 2.12 and will follow:

$$\begin{aligned}\gamma(t) =& \gamma_0 \cos\left(\frac{\Omega_R t}{2}\right) - i\bar{\gamma}_0 \sin\left(\frac{\Omega_R t}{2}\right)\\ &-G^+ \exp\left(-i\frac{\Omega_R t}{2}\right)\left(\mathrm{erfi}\left(\frac{it_1+\tau^+}{\sqrt{2}\sigma}\right) - \mathrm{erfi}\left(\frac{-i(t-t_1)+\tau^+}{\sqrt{2}\sigma}\right)\right)\\ &\mp G^- \exp\left(i\frac{\Omega_R t}{2}\right)\left(\mathrm{erfi}\left(\frac{it_1+\tau^-}{\sqrt{2}\sigma}\right) - \mathrm{erfi}\left(\frac{-i(t-t_1)+\tau^-}{\sqrt{2}\sigma}\right)\right).\end{aligned} \tag{2.14}$$

In our notation γ stands for α and β with the convention $\bar{\alpha} = \beta$ and $\bar{\beta} = \alpha$. Are also defined:

$$G^\pm = \frac{1}{4}\exp\left(-\frac{\tau^\pm(2it_1+\tau^\pm)}{2\sigma^2}\right)(P_a \pm P_b e^{i\phi})\,, \tag{2.15a}$$

$$\tau^\pm = \sigma^2\left(\mp\frac{\Omega_R}{2} + \omega_L\right). \tag{2.15b}$$

In the experiment, the pulses are assumed to be Gaussian:

$$P_c(t) = \frac{P_c e^{i\phi_c}}{\sigma\sqrt{2\pi}} e^{-\frac{(t-t1)^2}{\sigma^2}}\,, \tag{2.16}$$

with $\phi = \phi_b$ and $\phi_a = 0$. The particular form of Eq. 2.14 arises from the pulse component of the Hamiltonian. Indeed, error functions erf appear naturally to describe the pulse arrival and its transient behaviours:

$$\int_0^t e^{-\frac{(t'-t_1)^2}{2\sigma_t^2}}\,\mathrm{d}t' = \frac{\mathrm{erf}\left(\frac{t_1}{\sqrt{2}\sigma_t}\right) - \mathrm{erf}\left(\frac{t_1-t}{\sqrt{2}\sigma_t}\right)}{\sqrt{2}\pi^{-1/2}}\,. \tag{2.17}$$

Let us digress for a moment to comment a proposal published by Demirchyan *et al.* (2014) [36], where the authors propose the creation of a state such that the excitation scheme generates a non-factorizable product, unlike the coherent states in Eq. 2.10, that is, a quantum superposition of "*macroscopically* occupied orthogonal states". The Authors therefore propose a way to implement "polariton cat states", i.e., entanglement of coherent states. This is quite different from our "normal mode coupling" states above, that are essentially classical states. But even

without going into the quantum superposition of condensates, it is worth delving into the details of a populare representation of polaritons, namely, as a linear superposition of bare states. Any Fock state of polaritons constitutes such a quantum superposition, starting with the building blocks of one-particle states:

$$\|1,0\rangle\rangle = \cos\theta\,|0,1\rangle - \sin\theta\,|1,0\rangle\,, \tag{2.18a}$$

$$\|0,1\rangle\rangle = \sin\theta\,|0,1\rangle + \cos\theta\,|1,0\rangle\,, \tag{2.18b}$$

writing $|n,m\rangle$ as a shortcut for $|n\rangle\,|m\rangle$ the pure state with n photons and m excitons, and $\|n,m\rangle\rangle$ the pure state with n lower polaritons and m upper polaritons. Such a genuinely quantum state is indeed produced any time that, from the vacuum, one quantum of excitation excites the microcavity. But despite the true quantum nature of these one-particle states, building a coherent superposition of them does cancel their entanglement and results in coherent states, in any considered basis. For instance, a coherent state of lower polaritons reads:

$$\|\alpha,0\rangle\rangle = e^{-|\alpha|^2/2}\sum_{n=0}^{\infty}\frac{\alpha^n}{\sqrt{n!}}\|n,0\rangle\rangle\,, \tag{2.19}$$

which is nothing more than a product of coherent states of photons and excitons:

$$\begin{aligned}\|\alpha,0\rangle\rangle &= e^{-\frac{|\alpha|^2}{2}}\sum_{n=0}^{\infty}\frac{\alpha^n}{\sqrt{n!}}\sum_{k=0}^{n}\sqrt{\binom{n}{k}}\cos^k\theta\sin^{n-k}\theta\,|k,n-k\rangle \\ &= |\alpha\cos\theta,\alpha\sin\theta\rangle\,.\end{aligned} \tag{2.20}$$

These states could not be used for applications in quantum information processing, as they essentially describe a classical phenomenon. However, they can find an interest for fundamental purposes and semi classical applications, like classical qubits, also called "cebits" and proposed by R.J.C. Spreeuw (1998) [37]. The same holds true with thermal excitation. Unless there is an internal strong nonlinearity that can turn a classical external excitation into an internal quantum state, polaritons are in classical states unless excited quantum-mechanically, even though they are intrinsically quantum superposition of light and matter. The problem of achieving a quantum polariton therefore reduces simply to that of how the system is excited, as has been recently discussed by López Carreõ *et al.* [38].

We now come back to the states of Eq. 2.14, if the system is prepared in the state $|\alpha_0\rangle\,|\beta_0\rangle$, then the wave function subsequently evolves as:

$$|\psi(t)\rangle = |\alpha_0\cos(\Omega_R t/2) - i\beta_0\sin(\Omega_R t/2)\rangle\,|-i\alpha_0\sin(\Omega_R t/2) + \beta_0\cos(\Omega_R t/2)\rangle\,. \tag{2.21}$$

From Eq. 2.21, two particular cases of interest can be obtained. First, if $\alpha_0 = \mp\beta_0$ the state becomes:

$$|\psi(t)\rangle = \left|\alpha_0 e^{\pm igt}\right\rangle\left|\mp\alpha_0 e^{\pm igt}\right\rangle\,, \tag{2.22}$$

which correspond to the freely propagating lower $\left\|-\sqrt{2}\alpha e^{igt},0\right\rangle\rangle$ and upper $\left\|0,\sqrt{2}\alpha e^{-igt}\right\rangle\rangle$ polariton condensates, respectively. The second case stands for $\alpha \neq 0$ and $\beta = 0$ (or

vice versa), in this configuration the wave function becomes:

$$|\psi(t)\rangle = |\alpha_0 \cos(gt)\rangle |-i\alpha_0 \sin(gt)\rangle \,, \tag{2.23}$$

corresponding to Rabi oscillations between the two fields. These oscillations are clear and direct counterpart of two-coupled oscillators cast in a quantum formalism, making it clear how they constitute normal mode coupling [32] even though they hold in a quantum system. The denomination of Rabi oscillations remains however popular. In Section 2.3.4 we will see how theses states evolve in the Husimi representation.

2.3.2 Dissipative Dynamics

So far, our optical model contains the ingredients needed to describe the coupling of the two fields and their dynamics under pulse excitations, which is good enough to account qualitatively for the motion of the system. However, the experiment involves various sources of decay and dephasing that have to be included in the model to provide a quantitative agreement.

The main change in the description concerns the mathematical object we were dealing with until now, namely the wave function. We now describe the system through a density matrix ρ, ruled by Liouville–von Neumann Equation:

$$\dot{\rho} = \frac{i}{\hbar}[\rho, H] + \mathscr{L}\rho, \tag{2.24}$$

where $\mathscr{L}$ is the Lindblad super-operator that, for a generic operator c, reads [39]:

$$\mathscr{L}_c\rho = 2c\rho c^\dagger - c^\dagger c\rho - \rho c^\dagger c\,. \tag{2.25}$$

If c is an annihilation operator, the Lindblad term induces a decay, *i.e.* of loss of particles. On the contrary, if c is a creation operator, it acts as a pumping, *i.e.* an injection of particles. One can also describe pure dephasing, with corresponding Lindblad operator $\mathscr{L}_{c^\dagger c}\rho$ containing both a creation and an annihilation operator. This implies a constant population but it kills the off-diagonal terms of the density matrix, removing the coherence from the system. In our system, to include all these types of terms, we recourse to a sum of super-operators:

$$\mathscr{L}\rho = \frac{\gamma_a}{2}\mathscr{L}_a\rho + \frac{\gamma_b}{2}\mathscr{L}_b\rho + \frac{\gamma_{\mathrm{U}}^{\mathrm{R}}}{2}\mathscr{L}_u\rho + \frac{\gamma_{\mathrm{U}}^{\phi}}{2}\mathscr{L}_{u^\dagger u}\rho + \frac{P_b e^{-\gamma_{P_b} t}}{2}\mathscr{L}_{b^\dagger}\rho\,, \tag{2.26}$$

with γ_a and γ_b stands for the radiative decay of the modes a and b, respectively. The term $\gamma_{\mathrm{U}}^{\mathrm{R}}$ is the radiative decay of the upper polariton u, that could be also expressed as a combination of photonic and excitonic mode as $u = (a+b)/\sqrt{2}$. However, it remains more clear if one can see directly which decay or dephasing acts on which modes. The term $\gamma_{\mathrm{U}}^{\phi}$ describe the pure dephasing of the upper polariton. Clearly, one could have considered all the possible terms, e.g., exciton pure dephasing,

photon pumping, etc. Here we have written the dynamical equation that takes into account the most likely dynamical effects, which are an incoherent excitation from the excitons (from the exciton reservoir) leading to a pumping rate γ_{P_b} (that comes with a finite lifetime $1/\gamma_{P_b}$ from the reservoir lifetime) and additional decay terms for the upper polaritons. From a physical point of view, the origin of the upper polariton dephasing is commonly attributed to the vicinity of the interband absorption edge and the phonon assisted relaxation of polaritons from the bottom of the UPB to high-k states of the LPB [40, 41]. Here we are mainly concerned with the dynamical effects, described at a phenomenological level, rather than microscopic derivations.

Such a description with a density matrix generates a huge amount of informations, while most of it is not needed in our case. Experimentally, the only accessible quantity is $|\langle a(t)\rangle|^2$ which can be fitted in order to recover $\langle a(t)\rangle$ intrinsically related to $\langle b(t)\rangle$. For the general case of two-pulses excitations, the full dynamics can be recovered by solving numerically their coupled set of equations:

$$\partial_t\langle a(t)\rangle = -i\left(\frac{P_a^{(1)}\,e^{i\phi_1}\,e^{-\frac{1}{2}(\frac{t-t_1}{\sigma_1})^2}}{\sqrt{2\pi}\sigma_1} + \frac{P_a^{(2)}\,e^{i\phi_2}\,e^{-\frac{1}{2}(\frac{t-t_2}{\sigma_2})^2}}{\sqrt{2\pi}\sigma_2}\right) + \frac{1}{4}(-2\gamma_a - \gamma_U + 4i\,\omega_L)\langle a(t)\rangle - \frac{1}{4}(2i\Omega_R + \gamma_U)\langle b(t)\rangle, \tag{2.27a}$$

$$\partial_t\langle b(t)\rangle = -i\left(\frac{P_b^{(1)}\,e^{-\frac{1}{2}(\frac{t-t_1}{\sigma_1})^2}}{\sqrt{2\pi}\sigma_1} + \frac{P_b^{(2)}\,e^{-\frac{1}{2}(\frac{t-t_2}{\sigma_2})^2}}{\sqrt{2\pi}\sigma_2}\right) - \frac{1}{4}(2i\Omega_R + \gamma_U)\langle a(t)\rangle + \frac{1}{4}(2P_b e^{-\gamma_{P_b}t}H(t-t_1) - 2\gamma_b - \gamma_U + 4i\omega_L)\langle b(t)\rangle, \tag{2.27b}$$

where the initial condition is set to the vacuum for both fields: $\langle a(0)\rangle = \langle b(0)\rangle = 0$. The term $P_c^{(i)}$ denotes the first ($i = 1$) or the second ($i = 2$) pulse exciting the photonic ($c = a$) or the excitonic ($c = b$) field. The pumping term comes with a Heaviside function that set it to zero until the first pulse arrives. The Eqs. 2.27 are the ones we used to fit the experimental data for the one and the two-pulses experiment. The equations to fit the one-pulse experiment being simply obtained by setting the second pulse to zero $P_a^{(2)} = P_b^{(2)} = 0$. Note that even if the system is experimentally excited with a laser pulse, which ostensibly drives only the photonic field, we need to introduce a the similar term $P_b^{(i)}$ to fit well the data. The excitonic field is not excited directly by the laser, however the coupling strength of the two fields induces an immediate transfer between them when one starts to be filled, or with a short response time in good approximation. More details on the fitting methods are given in the Section. 2.5.3.

Equations 2.27 can be integrated exactly in the case of an infinite lifetime of the exciton reservoir $\gamma_{P_b} = 0$, however, these expression are too cumbersome to be written here. Further simplifications can lead to practical solutions. For instance by

considering the initial conditions $\langle a(0)\rangle = a_0$ and $\langle b(0)\rangle = b_0$ instead of the pulses, the dynamics of Eqs. 2.27 can be reduced to a simple form that still catch most of the phenomenology:

$$\langle a(t)\rangle = \left[a_0\cosh(\frac{1}{4}Rt) - \left(\frac{b_0 G + a_0\Gamma}{R}\right)\sinh(\frac{1}{4}Rt)\right]\exp(-\frac{1}{4}\gamma t)\,, \tag{2.28a}$$

$$\langle b(t)\rangle = \left[b_0\cosh(\frac{1}{4}Rt) + \left(\frac{-a_0 G + b_0\Gamma}{R}\right)\sinh(\frac{1}{4}Rt)\right]\exp(-\frac{1}{4}\gamma t)\,, \tag{2.28b}$$

where we have introduced the reduced parameters:

$$\gamma = \gamma_a + \gamma_b + \gamma_\mathrm{U} - P_b\,, \tag{2.29a}$$

$$\Gamma = P_b - \gamma_b + \gamma_a\,, \tag{2.29b}$$

$$G = 2i\Omega_\mathrm{R} + \gamma_\mathrm{U}\,, \tag{2.29c}$$

$$R = \sqrt{G^2 + \Gamma^2}\,, \tag{2.29d}$$

and, since only the sum of radiative decay $\gamma_\mathrm{U}^\mathrm{R}$ and pure dephasing γ_U^ϕ of the upper polariton plays a role in the coherent dynamics, the total upper polariton dephasing rate:

$$\gamma_\mathrm{U} = \gamma_\mathrm{U}^\mathrm{R} + \gamma_\mathrm{U}^\phi\,. \tag{2.30}$$

The solutions Eqs. 2.28 can be related to the ones of Eq. 2.14 in the sense that they now contain the dissipation (both radiative lifetimes and pure dephasing of the upper polariton) and the incoherent pumping from the exciton reservoir (assume constant). The coherent excitation is however neglected as we consider an initial state instead.

2.3.3 Bloch Sphere Representation

We now discuss the problem of the visualization of the polariton dynamics. We basically have to deal with the oscillations that arise from an effective two-level system, or more practically, two complex numbers from the fields' wave functions. The coherent amplitudes of any two-level system can be mapped on the Bloch sphere. A pure state $|\psi\rangle$ can be decomposed over its eigenstates $|0\rangle$ and $|1\rangle$ as:

$$|\psi\rangle = \alpha|0\rangle + \beta|1\rangle\,, \tag{2.31}$$

where α and β are complex numbers such that $|\alpha|^2 + |\beta|^2 = 1$, in order to maintain $|\langle\psi|\psi\rangle|^2 = 1$. Thus, the following parametrization can be chosen:

$$|\psi\rangle = \cos(\theta/2)|0\rangle + \sin(\theta/2)\exp(i\phi)|1\rangle\,, \tag{2.32}$$

with θ and ϕ the asimuthal and radial angles in polar coordinates, respectively. In the case of a polariton system, the two basis vectors are the upper and lower

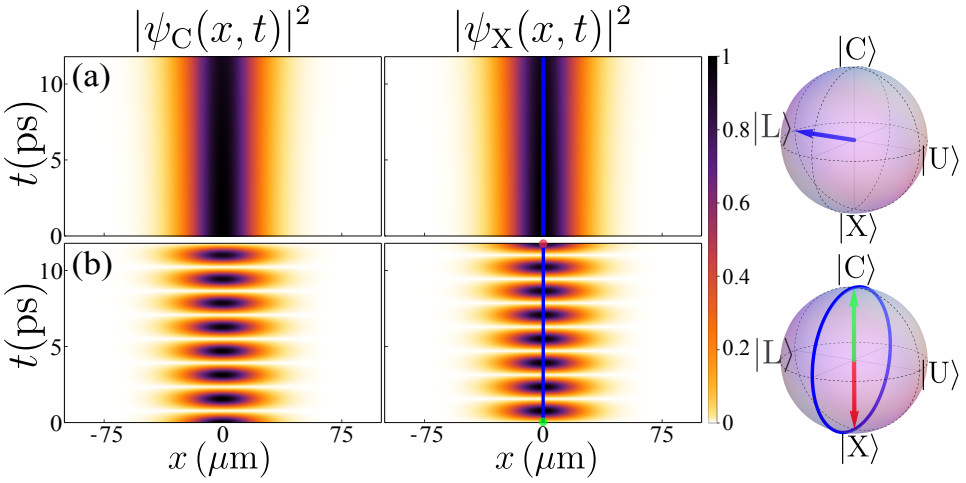

Figure 2.2: Polariton propagation of delocalized wavepackets, as seen through the photonic (ψ_C) and excitonic (ψ_X) components for the cases of (a) upper row: a lower polariton at $t = 0$ and (b) lower row: a photon. The diffusion is negligible over the selected time window and the staggering on the dispersion too small to evidence polariton self-interference effects. Parameters: $\Omega_R = 2$ meV, $m_C = 0.025$ meV ps^2 μm^{-2}, $m_X = 2$ meV ps^2 μm^{-2}, $\sigma_x = 20$ μm.

polariton states.

The Bloch sphere representation will be used in the same way to show the state of polarization in Chapter 3, where we will refer to it as the *Poincaré sphere of polarization* or simply *Poincaré sphere*. In the following, the term *Bloch sphere* will always refer to the sphere on which are mapped the quantum states of the polaritons.

In order to always lie on the surface of the sphere, we chose to keep the states normalized at all times:

$$\langle a\rangle_N = \frac{\langle a\rangle}{\sqrt{|\langle a\rangle|^2 + |\langle b\rangle|^2}}\,, \tag{2.33a}$$

$$\langle b\rangle_N = \frac{\langle b\rangle}{\sqrt{|\langle a\rangle|^2 + |\langle b\rangle|^2}}\,. \tag{2.33b}$$

Then, the corresponding angles $\theta(t)$ and $\phi(t)$ can be simply obtained by solving the following system:

$$\langle a(t)\rangle_N = \cos(\theta/2)\,, \tag{2.34a}$$

$$\langle b(t)\rangle_N = \sin(\theta/2)e^{i\phi}\,. \tag{2.34b}$$

In such a representation, the couple of states $|C\rangle$–$|X\rangle$ and $|U\rangle$–$|L\rangle$ are displayed on opposite poles of the sphere. A convenient aspect of the Bloch Sphere is that its orientation depends on the basis on which the states are calculated, thus a simple rotation of the sphere corresponds to a change of basis.

In Fig. 2.2, we present the most trivial cases of the polariton dynamics, that are when the system is in an eigenstate (a) (here the LP state) and when the sys-

tem exhibits simple Rabi oscillations (b). The quantum state taken over a path (blue straight lines) on the space-time charts are mapped on a corresponding Bloch sphere. Both the photonic and excitonic density probabilities $|\psi_C|^2$ and $|\psi_X|^2$ are plotted, but only the first one will be accessible experimentally.

In the first case (a), one can see that the system is always in the LP state, pointing the $|L\rangle$ pole of the Bloch sphere, as expected. In the second case (b), the initial state was prepared by putting a Gaussian wave packet into the photonic state $\psi_C(x, t = 0) = (1/\sigma_x\sqrt{2\pi})\exp(-x^2/2\sigma_x^2)$, with σ_x the spatial spread of the packet. As this state is not an eigenstate of the system, Rabi oscillations occur and we see a typical beating in time between the two fields, the intensity going to zero for a field when it is maximum into the other one. This yields loops onto the Bloch sphere between the $|C\rangle$ and $|X\rangle$ states, passing through the opposite cardinal points. The green arrow indicates the initial position of the path (green dot) and the red arrow the final one (red dot).

2.3.4 Husimi Representation

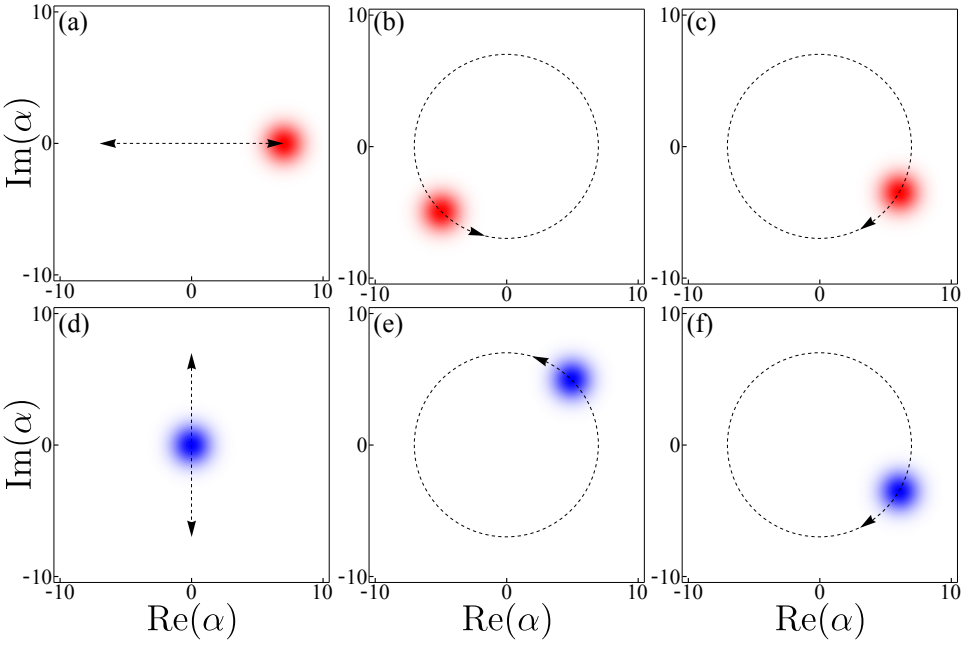

Figure 2.3: Husimi representation of polariton states calculated in the rotating frame, with the complex amplitude of the photon (exciton) in red (blue). The (a,d) column corresponds to the excitation of a bare states, that induces Rabi oscillations. The (b,e) column is obtained from a lower polariton state and the column (c,f) from an upper polariton state. In these cases, dephasing of the upper is not involved.

Introduced by Kôdi Husimi in 1940 [42], the now so-called Husimi representation is one of the popular representation of the density matrix, that projects the state in a phase space more intuitive than, say, the Fock basis. It consists in a simple

distribution of quasiprobabilities, that is generally more convenient to work with as compared to other representations, such as the Wigner or the Glauber distributions, where one has to deal with complex integrals. On the opposite, the Husimi representation is simply a dotting of the density matrix with coherent states:

$$Q(\alpha,\beta) = \langle \alpha\beta | \rho | \alpha\beta \rangle \,, \tag{2.35}$$

and it is therefore particularly apt to our case that precisely consists of products of coherent states. Its reduced form is obtained by tracing over all but the mode of interest:

$$Q(\alpha) = \int Q(\alpha,\beta)\mathrm{d}\beta \,, \tag{2.36a}$$

$$Q(\beta) = \int Q(\alpha,\beta)\mathrm{d}\alpha \,. \tag{2.36b}$$

When it is a product of coherent states, the factorization is exact and no information is lost. A coherent state in the Husimi representation being simply a Gaussian distribution, it is relatively easy to picture and to understand its subsequent dynamics. Unlike the Wigner Transform, the Husimi distribution is always positive and unique. Thus, it cannot be considered as a true probability distribution over the quantum-mechanical phase space, in consequence it is considered as a quasi probability distribution.

In order to apply it to our polariton case, we put ourselves in the rotating frame, *i.e.* by setting our reference at the optical frequency of the laser ω_L. The polariton states such as the ones described by Eq. 2.21 oscillate counter-rotating in a circle for the lower polariton and rotating for the upper polariton. Indeed, the upper and lower polaritons oscillate faster and slower, respectively, by a factor $\pm\Omega_R/2$ over the optical frequency ω_L (with $\Omega_R \ll \omega_L$). In contrast, the states described by Eq. 2.23 oscillate radially and perpendicularly, the two fields being $\pi/2$ out-of-phase. The general case is a combination of these two kind of motions and results in an elliptical oscillation in the phase-space, therefore with a reduced contrast.

One can see in Fig. 2.3 the Husimi representation for these different polariton states. The first row corresponds to a bare state excitation whereas the second and the third rows show the representation for a lower and upper polariton state, respectively. In the absence of dephasing, the field distribution remains localised in a Gaussian shape. A polariton state can thus be simply modelled by a trajectory in phase space.

2.4 Experimental Rabi Oscillations Control

In this Section, we present the results of the Lecce experiments on the coherent control of polariton Rabi oscillations. The experimental setup and the acquisition technique are introduced first. We then give the results and the analysis of the one-pulse and two-pulses experiments. In the last part, we discuss the theoretical extents developed from the fitted data.

2.4.1 Experimental Setup and Simple Dynamics

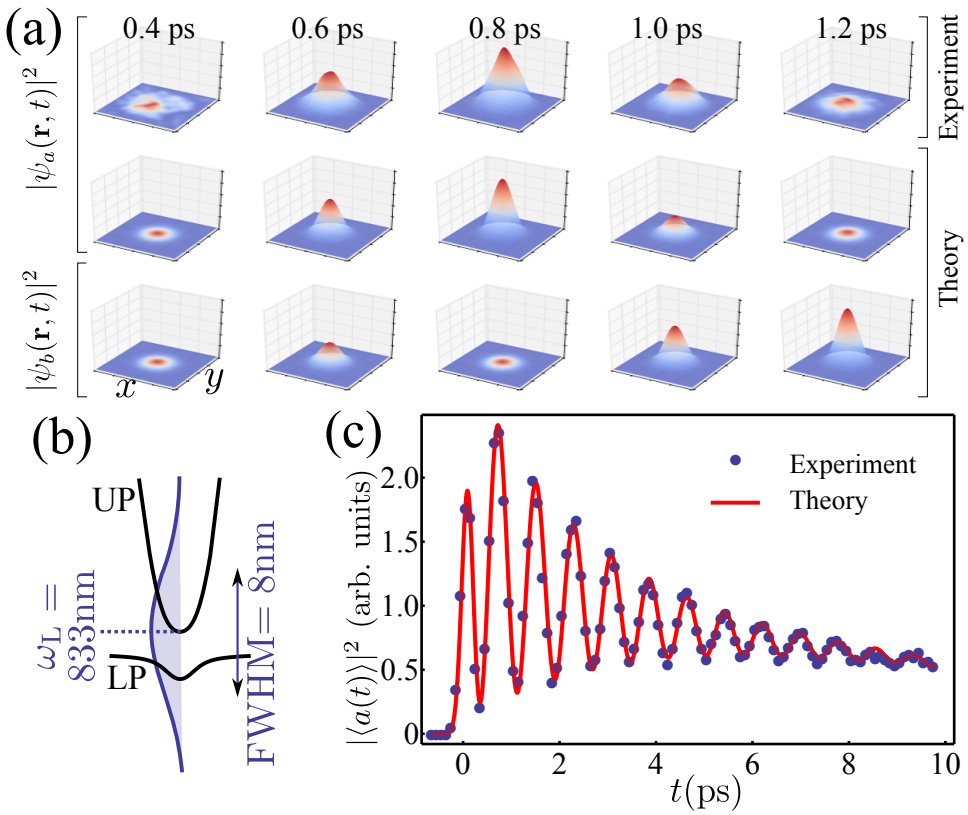

Figure 2.4: (a) Oscillations observed experimentally in the cavity field and reproduced theoretically in both the cavity and exciton fields. (b) The lower (LP) and upper (UP) polaritons excited by a Gaussian pulse which overlap with the branches determine the effective state created in the system. (c) The dynamics can be reduced to that of $|\langle a(t)\rangle|^2$ alone and described quantitatively by the theory.

For this experiment, my colleagues of Lecce used a microcavity sample composed of two high quality GaAs/AlAs Distributed Bragg Reflectors (DBR) of 21 and 24 pairs into which were embedded three $In_{0.04}Ga_{0.096}As$ Quantum Wells (QW) positioned at the antinodes of the cavity mode, setting the exciton resonance at 835 nm. Such a structure allows the formation of two polariton modes characterised by a Rabi splitting of $\Omega_R = 5.3$ meV, inducing Rabi oscillations with a period of ~ 800 fs. They used an elaborate off-axis digital holography technique allowing them to acquire both the amplitude and phase information. The different pulses sent on the sample have a typical width of ~ 130 fs, which give spread of 8 nm in energy, impinging on both polariton branches. A sketch of the excitation scheme is shown in Fig. 2.4(b). For this experiment, the temporal step resolution was set to ~ 100 fs. Each image results from a time-integration of over 10^5 experimental realizations.

One can see on the first row of Fig. 2.4(a) a typical experimental observation.

The laser pulse spreads in energy over the two branches, preparing the system in a bare state and not in an eigenstate, inducing oscillations between its two components. Here the polaritons have quite a large spatial extension, given by the exciting laser, which is here around 10 µm. It is important to remind that this experiment does not rely on nonlinear polariton-polariton interactions, as it is the case in many other polariton experiments. To do so, the excitation power was set at a low enough density in order to maintain their bosonic properties in the linear regime. The robustness of the different linear features will be analysed through a power experiment later. We have thus access to the subpicosecond linear Rabi oscillations through the coherent fraction $|\psi_C(r,t)|^2$ of the photonic field in both space and time. If only the photonic field is accessible experimentally, its excitonic counterpart can be recovered through the polaritonic equations we have detailed in the previous Section (see Eqs. 2.27). Still in Fig. 2.4(a), second and third rows, is plotted the reconstructed dynamics of both the photon and the exciton. As expected, the exciton field arises as the photon field vanishes, initiating a Rabi cycle. As we already said in Section. 2.3.1, the system is linear, presents a minimal diffusion and is not imparted by any momentum. Thus, the dynamics can be reduced to zero dimension. In the following we consider only $\langle a(t)\rangle$ and $\langle b(t)\rangle$, defined previously in Eqs. 2.7. The accessible field $|\langle a(t)\rangle|^2$ is shown in Fig. 2.4(c) now for the full duration of the experiment. Twelve oscillations are clearly resolved after the arrival of the pulse and until t = 10 ps. These data have been fitted with the optical model developed in the Section 2.3, see as well Section 2.5.3 for the details of the fitting methods. The fit provides an essentially perfect agreement with the experimental data.

In the following, I present other experimental results, namely, a single pulse experiment performed by exciting the system at different energy levels, with different powers and a two-pulse experiment where the coherent control of the oscillations is demonstrated.

2.4.2 One Pulse Experiment at Different Energy Levels

We have seen before how, by exciting with a broad laser in energy, one can excite both polariton branches to induce Rabi oscillations. This brings several first questions: how does the excitation scheme matter? How can the oscillations be affected by exciting one branch more than the other one? To answer these questions, the experimentalists have excited the polariton branches at various energy levels. With this sample, the UPB is located at 833.5 nm while the LPB is at 836.5 nm. The system was excited from 825 nm until 841 nm with a 2 nm increment. We remind that, in energy, the laser pulse has a FWHM of 8 nm, thus, even exciting far from the polariton branches, the energy distribution of the laser still "touches" both of them. The corresponding series of fitted data is displayed on Fig. 2.5. Again, the fits are essentially perfect. Parameters that are fixed are consistent throughout, showing that the procedure is consistent.

We have seen in Section 2.3 how by fitting the experimental $|\langle a(t)\rangle|^2$ one can

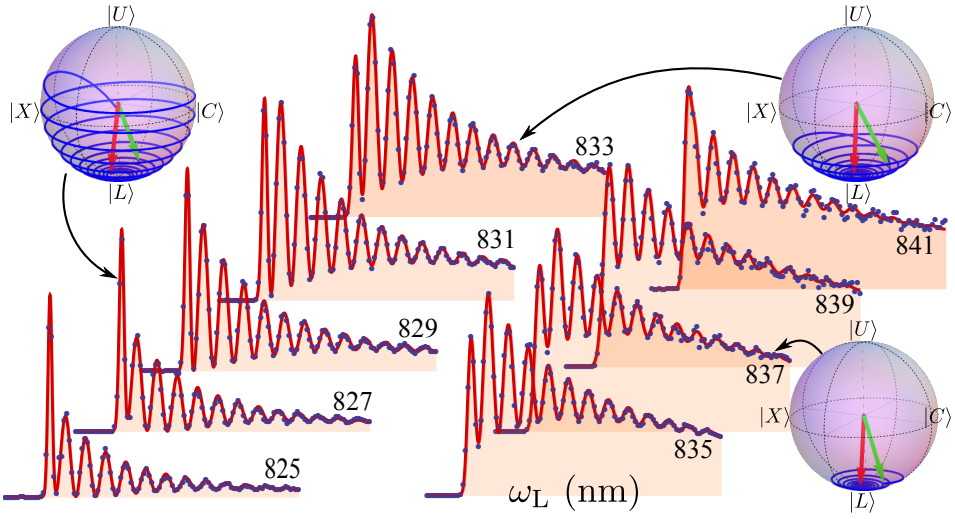

Figure 2.5: Various states created in the system by varying the pulse energy and their evolution on the Bloch sphere, showing the systematic relaxation towards the LP. The experimental data (blue dots) is fitted with the optical model presented in Section 2.3.1

get access as well to the entire dynamics of oscillations, that includes the excitonic field $|\langle b(t)\rangle|^2$, but also to the phases $\langle(a^\dagger a)(t)\rangle$ and $\langle(b^\dagger b)(t)\rangle$. The full density matrix ρ becomes actually accessible. In Fig. 2.7(a), we plot the case of 833 nm excitation, with the fitted photonic intensity (in red) and the reconstructed excitonic part (in blue). We are now free to vary the different parameters (lifetimes, pumping, etc.) and see their physical effects on the Rabi oscillations.

We start in panel (b) with the effect of the exciton reservoir in black-dashed lines. The effective pumping rate P_b has been set to zero. We see that the effect of the pump on the oscillation pattern is small but is really needed to reproduced quantitatively the experimental data.

We show in panel (c) which of the parameters has a dominant effect on the oscillations, that is the upper polariton decay/dephasing γ_U. Here, the pump P_b has been set to its original fitted value and the upper dephasing γ_U to zero. Without this parameter, the lifetime of the oscillations is drastically extended, assisted by the incoherent reservoir. This effect can be highlighted, as done in panel (d), by setting the pump to a higher value, for instance three times the fitted value. This brings the oscillations lifetime to the scale of nanoseconds. Such a mechanism of lifetime enhancement of the Rabi oscillation has been suggested by Demirchyan [36], but regarded as qubits, while we are here sustaining classical oscillations. The pumping to do so is incoherent, so the result nevertheless appears to be nontrivial. However, this is because we are here focusing on the coherent fraction of the dynamics. The total population diverges in time as the lifetime of the Rabi oscillation becomes infinite [49]. It is therefore particularly important to consider the quantum state that supports such oscillations, for instance at different energies. Still on Fig. 2.5, we have mapped the quantum state on a Bloch Sphere for three different

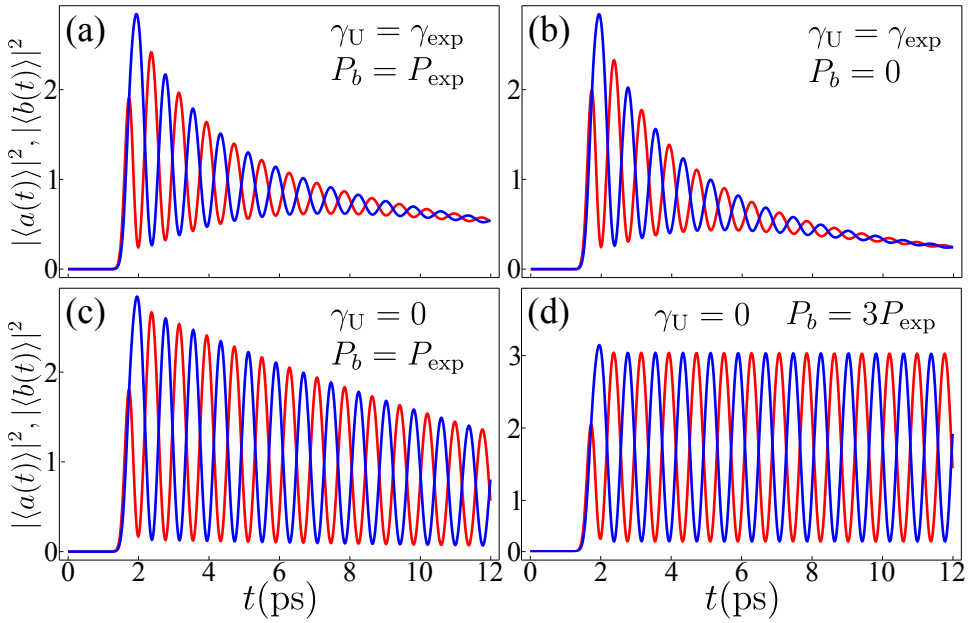

Figure 2.6: The full exciton-photon dynamics is reconstructed theoretically for the case $\omega_L = 833$ nm (photon in red, exciton in blue). (a) Experimental case. (b) The effect of the exciton reservoir is removed by setting $P_b = 0$. (c) The effect of the upper polariton decay-dephasing is removed by setting $\gamma_U = 0$. (d) The effect of the reservoir is enhanced to obtain long-lived oscillations, by setting $\gamma_U = 0$ and $P_b = 3P_{exp}$.

case. The first one where the energy distribution of the pulse is located above the UPB at 827 nm. A second case where the two branches are excited symmetrically at 833 nm, and a third case where the laser excites below the LPB in energy at 837 nm. It is clearly seen in the first case how the pulse swings the coupled oscillators towards the upper state and, in all cases, how the system quickly reaches the LPB. The observation is fundamental as it confirms one of the most fundamental assumptions of microcavity polariton physics: the upper polariton is unstable and the system relaxes towards the LPB, even though it retains strong coupling. In our quantum optical model, the upper dephasing rate γ_U (see Eq. 2.30) can be either a decay rate, a pure dephasing rate or a combination of both, as only their sum enters in the equation of the coherent fraction. This also shows that even if the impinging laser is very wide in energy, we are able to prepare the polariton state in a large tunable range, from a state almost entirely upper polaritonic, at least for a short time after the excitation, to a state entirely lower polaritonic, which is also the state at long times. All of this passing through photonic and excitonic states due to the upper dephasing.

For this energy series experiment, we have listed in the Table. 2.1 the different physical parameters. They have been optimized through a multi-pass fitting procedure that we detail in Section. 2.5.3.

Parameters	Physical Meaning	Best Fit
Ω_R	Coupling Strength	2.65 ps^{-1}
γ_a	Cavity decay rate	0.2 ps^{-1}
γ_b	Exciton decay rate	0.001 ps^{-1}
γ_U	Upper polariton dephasing rate	0.43 ps^{-1}
P_b	Exciton reservoir pumping rate	0.11 ps^{-1}
γ_{P_b}	Exciton reservoir decay rate	0.01 ps^{-1}

Table 2.1: System parameters and their best fit values for the energy series experiment (varying ω_L, cf. Fig. 2.5). The same parameters apply for the pumping series, only with $\gamma_U = 1/0.41$ ps

2.4.3 One Pulse Experiment at Different Power Levels

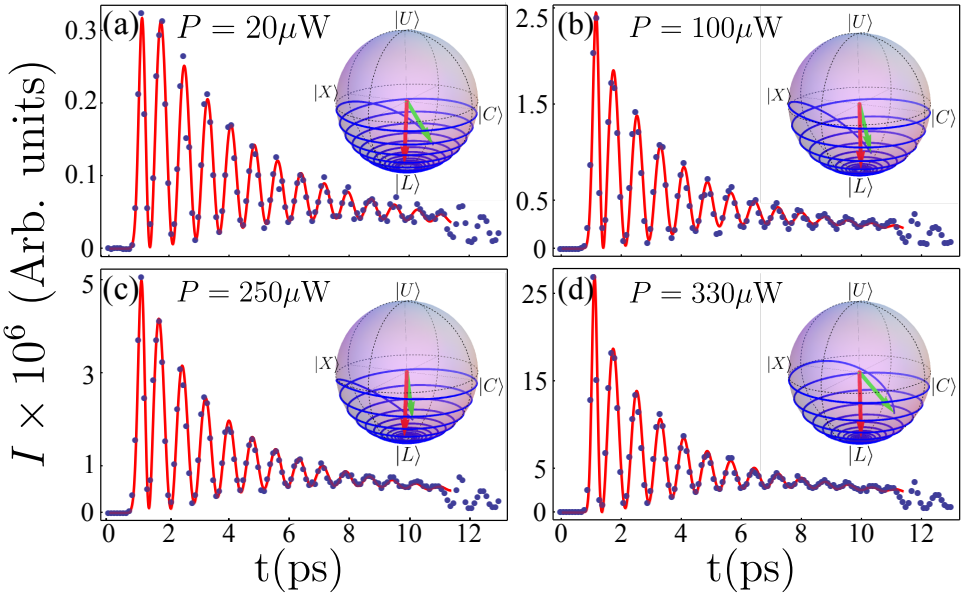

Figure 2.7: The microcavity is excited at different powers. The corresponding quantum state is reconstructed from the fit (red) of the experimental data (blue dots). On the spheres, the green (red) arrow points to the initial (final) state. It shows that the polariton state is barely not affected by a power variation.

The same one-pulse experiment was performed at a fix energy of $\omega_L = 829$ nm but this time varying the power, in order to study the pumping dependence. The power was set in a range going from 20 µW to 330 µW, increasing *de facto* the population of the system. However, such power values still leave the system into the linear regime. A higher pumping would lead to the long-living and ultrasharp "backjet" phenomenology [43] that we have discussed in the Introduction. The results are presented in Fig. 2.8 and Fig. 2.7. The same multi-pass fitting procedure was applied to fit the experimental data, with again an essentially perfect agreement. It shows a strong resilience and stability of the quantum state to power

variations over one order of magnitude. In Fig. 2.7, one can see that the contrast of the oscillations is similar whatever is the applied pumping, we have seen in the previous Section how the pump induces a small change of the contrast. *Idem* for the quantum states, whose trajectories on the Bloch Sphere follow the same behaviours. The different physical parameters, fitted from this experiment, show the same values than the one obtained with the energy series experiment, only the upper polariton dephasing varies slightly, see Table 2.1. The parameters related to the excitation mechanism are displayed in Fig. 2.8. The pump $P_a^{(1)}$ that acts on the photonic field (in red) increases linearly with the applied pumping, as expected, since this is precisely the variable that is tuned experimentally. However the ratio $P_a^{(1)}/P_b^{(1)}$ and the relative phase ϕ_1 remain roughly constant. This means that the excitation mechanism of both the photonic and excitonic fields does not suffer from a variation of the pumping value. This gives us an important indication on how the laser couples to the system, which is crucial for the coherent control of the oscillation realised with various pulses. This information is not easy to obtain but we deduce that the laser couples almost equally both the photon and the exciton (a little bit more the photon), both being almost in optical antiphase.

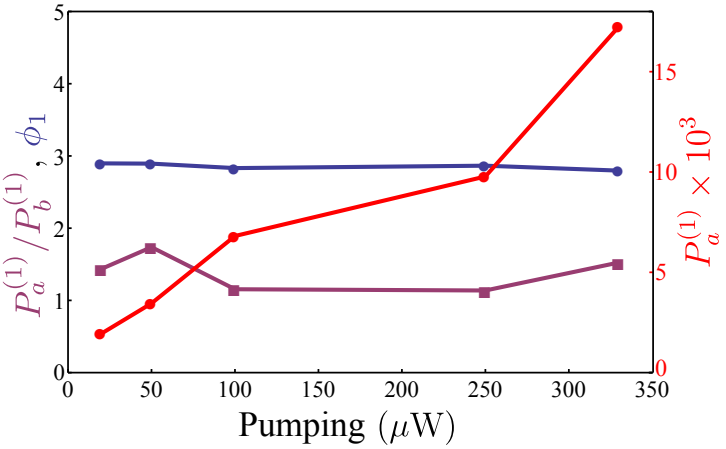

Figure 2.8: Best fitting numerical value for the pumping parameters $P_a^{(1)}$ (red), right axis, and the ratio $P_a^{(1)}/P_b^{(1)}$ (purple), left axis, which is roughly constant. The relative phase between ϕ_1 plotted in blue, left axis, is almost constant as well.

2.4.4 Two Pulses Experiment and Rabi Oscillations Control

We have learnt precious informations from the one-pulse experiments on the excitation mechanism and on the role of the different physical parameters, either in the energy series or in the power series. With such an accurate command of the system, we have been able to control precisely the time arrival of a second pulse and perform a comprehensive coherent control on the coupled dynamics. If the laser was only coupling to the cavity, this would be achieved for most operations

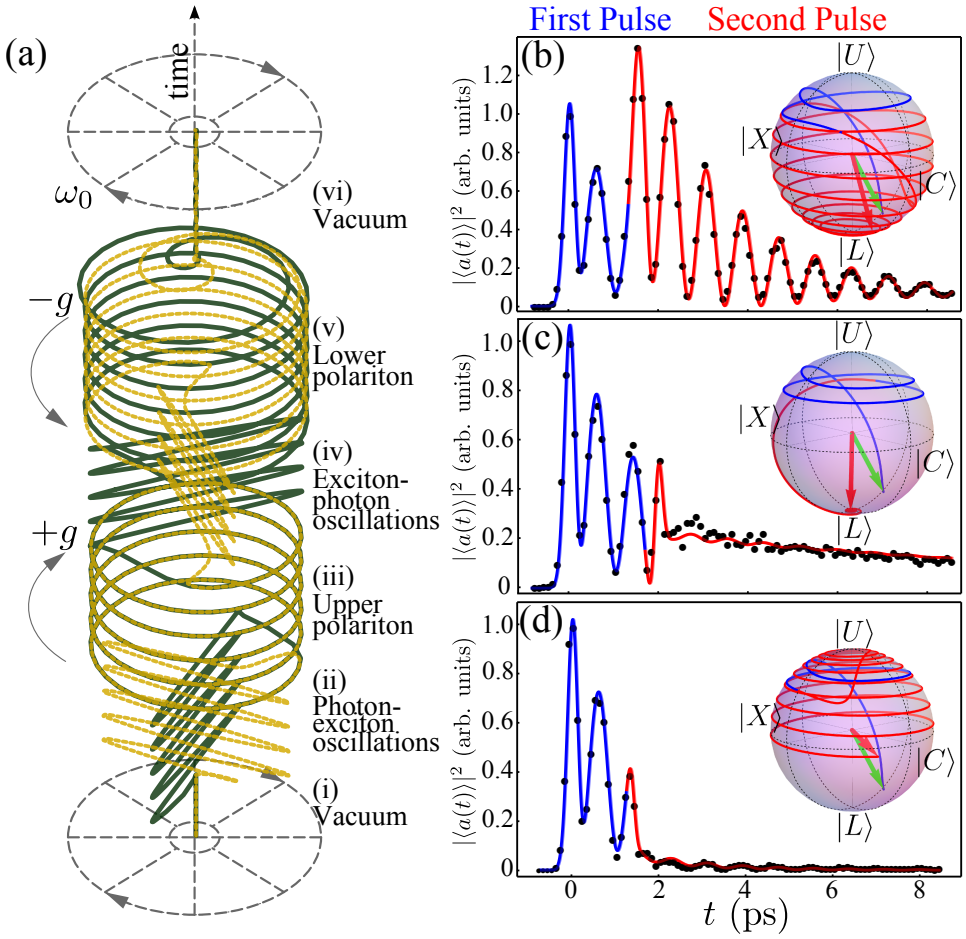

Figure 2.9: (a) Succession of various dynamical evolutions in time of the photon (dashed yellow) and the exciton (green) complex amplitudes (here with fixed modulus) that can be passed from one to the other with an appropriate pulse excitation. Normal mode-coupling features a $\pi/2$ dephasing in both time and optical phase and oscillate radially while polaritons oscillate circularly. Furthermore, they oscillate jointly and with (π out of phase with each other and against) the rotating frame in the case of a UP (LP). (b)–(d) Experimental realization (points) and theoretical fit (solid curve) of three two-pulses excitation, showing (b) amplification, (c) transition from an exciton-photon Rabi oscillation to a LP, and (d) field annihilation.

by sending the control pulse when the cavity field is empty and the state fully excitonic. In the present case sending a second photonic pulse in optical (anti-optical) phase with the exciton bring the system to the UP (LP) state. These kinds of transitions between the different states can be conveniently represented with the joint photon and exciton fields' complex phases, in the rotating frame. In Fig. 2.9(a), we plot the dynamical evolution of these complex amplitudes, with the photon in dashed yellow and the exciton in green, for a sequence of pulse bringing the system in the various states. It starts with a first pulse, turning the states from the vacuum to photon-exciton oscillations by pumping the photon. The complex amplitudes,

initially located in the center of the plane are now oscillating radially and perpendicularly with a $\pi/2$ dephasing. A second pulse brings the system in an upper polariton condensate. Unlike the previous case, the UP does not oscillate radially but circularly, since it is a free mode that adds its free energy to that of the rotating frame, as already described in the single-pulse experiment. A third pulse brings again the system in an oscillatory regime between photon and exciton, this time by pumping the exciton. This is followed by a fourth pulse that brings the system in a lower polariton condensate. Both of the complex amplitudes are oscillating circularly, but this time counter-clockwise and with a π dephasing, since the upper polariton is obtained by making the difference of the bare states ($l = (a-b)/\sqrt{2}$). Finally a last pulse brings again the states into the vacuum. To summarise, the sequence of pulses brings the system into the successive states:

1. vacuum,
2. excitation of a photon condensate,
3. transfer to an upper polariton condensate,
4. transfer to an exciton condensate,
5. transfer to a lower polariton condensate,
6. annihilation and return to the vacuum.

An animated version of the corresponding sequence in the Husimi representation is available on-line, in the supplementary material of ref. [44].

In the actual experiment, where the laser couples to both fields (exciton *and* photon), some corrections are needed to get the corresponding proportions, but the concept remains the same. The Rabi oscillations are triggered by sending a first pulse quite broad in energy that initiates a dominant photon or exciton fraction. One can refine the state by sending a second pulse, similar to the first one, to any desired configurations. In Fig. 2.9(b) is shown a simple case of Rabi oscillation amplification, where the oscillations cycle is magnified with the second pulse. Here, the experimental data (black dots) have been fitted with the full version of Eqs. 2.27, *i.e.* with the two pulses. The dynamical evolution of the quantum state has been thus reconstructed and displayed on the Bloch Sphere. The blue (red) line (fit and trajectory on the Bloch sphere) corresponds to the state created after the arrival of the first (second) pulse. The case of Fig. 2.9(c) is more interesting, it shows the transformation of a bare state, created by the 1st pulse, into a Lower polariton state when the second pulse arrives. The Rabi oscillations are then switched off and the population decreases with the lifetime of the Lower polariton. One can see on the Bloch Sphere how fast is the transition to reach the $|\mathrm{L}\rangle$ pole. Another case of interest is presented in Fig. 2.9(d), where the second pulse annihilates the field. This is achieved by sending a pulse optically out of phase but in phase with the Rabi oscillations, inducing destructive interferences that cancel the field intensity. As we normalise the states to lie on the surface on the Bloch Sphere, a dynamics is still present, that tends to reach the $|\mathrm{L}\rangle$ state, but corresponds to very small field

intensities. These three different cases exhibit a similar trend, namely, their quantum state evolve towards the $|\mathrm{L}\rangle$ state, due to the dephasing of the upper polariton. This is actually why bringing the system in a $|\mathrm{U}\rangle$ state is harder to achieve and was not clearly observed experimentally. All these cases demonstrate the possibility to do coherent control of the strong light-matter coupling dynamics.

The general sequence in Fig. 2.9(a) remains the theoretical, ideal version of what the experiment realizes with one operation at a time, since the time-window available to the experimentalists is not currently large enough to chain up various pulses. However the proof of principle has been fully demonstrated and there would be no fundamental difficulty in sending more than two pulses. Interesting perspectives are now opened, notably at the single-particle level to perform quantum information processing.

2.5 Theoretical Extents

In this Section, we discuss theoretical considerations and how the model we have developed allows us to go beyond the experimental observations. By solving the master equation, we get access to variables not within reach of the experiments. This allows to clarify the physics of the upper polariton dephasing, and explain its impact on the different populations. The dynamics of the four fields (exciton/photon and the polaritons) can be entirely reconstructed by using the fitted parameters.

2.5.1 Upper polariton dephasing

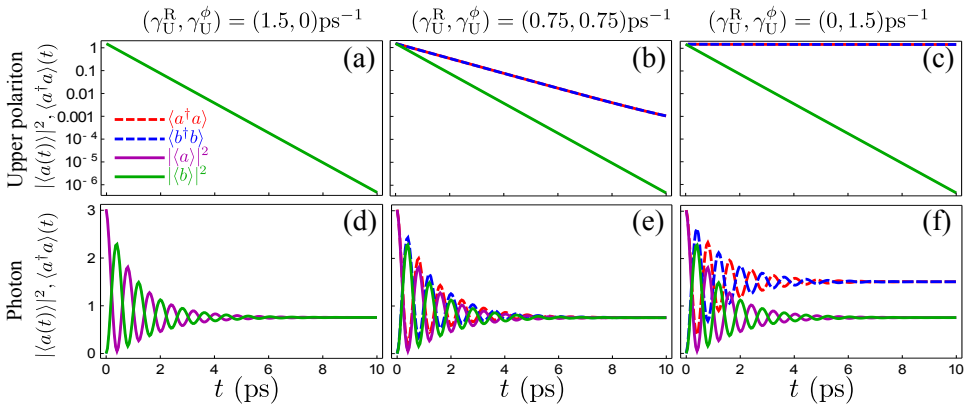

Figure 2.10: Effect of dephasing on the polariton population. The three cases shown in three columns for two different initial conditions (rows) keep the total rate $\gamma_{\mathrm{U}} = 3/2$ ps constant but balances radiative and pure dephasing from Eq. (2.30) as indicated in the header of each column. The evolution of the coherent (solid green & purple) and total, i.e., coherent+incoherent (dashed red & blue) populations of exciton and photon are shown as a function of time, starting from a condensate of upper polaritons (upper row) and of photons (lower row). The coherent fraction is the same, and looses its particle either radiatively or transferred to the incoherent fraction.

Let us consider some cases where the dephasing plays a more important role than in the experiment. In Fig. 2.10 is shown the dynamics of the system prepared in the upper polariton state, which is the one that suffers the most from dephasing. We plot it for a constant total rate γ_U (given by Eq. 2.30), but for different ratios between the radiative upper polariton and the upper polariton pure dephasing γ_U^R/γ_U^ϕ. The upper row stands for an upper polariton as the initial condition and the lower row to a photon instead. These calculations were performed by solving the master equation, and as we are now dealing with a full quantum system that has the complexity of a large Hilbert space, only few particles have been considered, namely, three particles at $t = 0$ (truncated at ten particles). In the experiment, the number of particles is orders of magnitude higher and the effect would not be significant on the considered time scales. There is no other source of decay introduced here. One can see that the coherent fractions $|\langle a\rangle|^2$ and $|\langle b\rangle|^2$ remain the same whatever is the repartition between the radiative decay and the pure dephasing of the upper polariton, as they are only sensitive to the total decay rate. The situation becomes more interesting when we look at the total population, which includes both the coherent and incoherent parts of the states. One sees how the polaritons are transferred to the incoherent fraction when a pure dephasing is present. In the last case (third column), the population remains constant when starting as a polariton or becomes so when the polariton fraction has vanished to leave a fully incoherent mixture. In the same way, when starting with a photon as an initial condition, the total of the photon and exciton populations $\langle a^\dagger a\rangle + \langle b^\dagger b\rangle$ is constant, the Rabi oscillations between them being lost because of the upper dephasing. The supplementary material of ref [44] provides an animation of the Husimi representation corresponding to the last case (f). In such a case, the Gaussian cloud does not remain localised any more and spreads into a ring as it rotates, a consequence of the dephasing.

2.5.2 Dynamics of the four fields

As we have seen in the previous Sections, the full dynamics of the four fields can be reconstructed by fitting the single photonic amplitude $|\langle a(t)\rangle|^2$. Indeed, all the needed parameters can be extracted from the photonic field intensity measured in the experiment, which is actually the only one accessible experimentally. The exciton is not directly measurable (it could be in principle but geometry, lifetimes and numerous other factors make it out of direct reach), and the polaritons can only be approximatedly recovered by frequency-filtering the photonic field. In Fig. 2.11, we present a set of cases of interest, computed numerically by using the physical parameters obtained with the different fits, acting only on the time delay between the pulses and their respective optical phases. Thus, in addition to $|\langle a(t)\rangle|^2$, we also plot the squared amplitude of the exciton condensate $|\langle b(t)\rangle|^2$, of the upper $|\langle u(t)\rangle|^2$ and the lower $|\langle l(t)\rangle|^2$.

The four cases start in the same way, exactly like in the experiment, exhibiting Rabi oscillations between the photonic (red line) and the excitonic (blue) fields. One can see as well how the polaritonic fields , the upper (dashed purple) and the

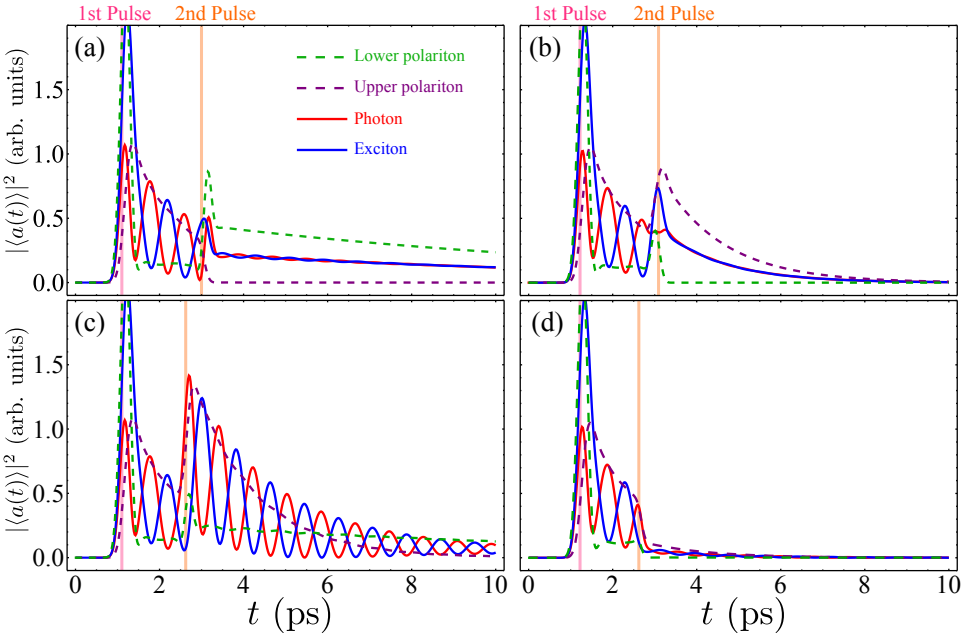

Figure 2.11: Two-pulses experiment as seen through all the theoretical variables: bare states in solid and eigenstates in dashed lines. The experimentally available variable is the photon field, in red. The three cases correspond to: (a) switching-off of the Rabi oscillation by bringing the state into a lower-polariton condensate, (b) revival of the oscillations and (c) annihilation of the field.

lower (dashed green), do not oscillate and decay at their respective rates.

The first case, panel (a), shows how the state is brought from the oscillating exciton-photon dynamics to a lower polariton state, the oscillations being switched-off and the bare fields decaying with the rate of the upper. The second case in panel (b) is the equivalent of the first one, but this time the system is brought in an upper state, instead of a lower one. This case has not been achieved experimentally, so far. The panel (c) shows a case of Rabi oscillations amplifications, exceeding their usual time duration. This show particularly how the upper polariton is the limiting factor here, although, from the fit, the upper polariton appears easily set in motion and populated, more than the lower polariton itself. Since it decays so quickly, ultimately, the system is driven into a lower polariton state only, regardless of its excitation at initial time. This influences the contrast of the oscillations, the upper polaritons tending to disappear, the system evolves into a non-oscillating state. The last panel (d) demonstrates the annihilation of all of the four fields. In this configuration, the optical phases of the pulses are in opposition. Because of the states normalisation that we do, this effect cannot be seen clearly on the Bloch Sphere (Fig. 2.9). This is a beautiful polariton-implementation of a famous apparent paradox of two waves that cancel each others by destructive interferences: where does the energy go?

2.5.3 Fitting Methods

Fitting the experimental data of the Lecce experiments consisted in numerical fits from the model we have developed in Section. 2.3.1, namely, a set of two differential equations (see Eqs. 2.27) for the photonic and the excitonic fields, taking into account the various parameters for which we seek the numerical values.

The experimental data have been fitted using two main techniques:

- The Levenberg–Marquardt Method
- The Principal Axis Method

The Levenberg–Marquardt Method (LMM), was named from Kenneth Levenberg who first published the algorithm in 1944 [45]. It was later improved and republished by Donald Marquardt in 1963 [46]. This method is now considered as a standart one for minimisation problems that arise in least squares curve fitting. It presents many advantages, such as a higher stability than a typical Gauss-Newton method. The convergence can be found even if the starting point is far from the minimum value. Let us introduce the main ideas of this method.

We consider first a fitting function $f(\vec{x},\vec{p})$ of some independent variables $\vec{x} = \{x_1,...,x_n\}$ and of a vector of n parameters $\vec{p} = \{p_1,...,p_n\}$. What is usually done is to look for the minimisation of the squared difference between the measured data $f(\vec{x})$ and the curve-fit function $f(\vec{x},\vec{p})$:

$$\Phi(\vec{p}) = \sum_{i=1}^{n} |f(x_i) - f(x_i,\vec{p})|^2 . \tag{2.37}$$

The procedure being iterative, one has to define first an initial vector $\vec{p}$. This initial guess is supposed to be close to the solution, however the algorithm gives a good convergence for standard values. At each iteration, the vector $\vec{p}$ is replaced by a new estimated $\vec{p}+\vec{\delta}$. Thus, one can do the Taylor expansion of the fitting function:

$$\begin{aligned} f(x_i,\vec{p}+\vec{\delta}) \approx & f(x_i,\vec{p}) + \frac{\partial f(x_i,\vec{p})}{\partial_{\vec{p}}}\vec{\delta} \\ \approx & f(x_i,\vec{p}) + \boldsymbol{J}\vec{\delta}\,, \end{aligned} \tag{2.38a}$$

that can be written with the Jacobian matrix $\boldsymbol{J}$. Note that the Taylor series is limited to linear terms. The minimization function of Eq. 2.37 can thus be expressed as:

$$\Phi(\vec{p}+\vec{\delta}) \approx \sum_{i=1}^{n} |f(x_i) - f(x_i,\vec{p}) - \boldsymbol{J}_i\vec{\delta}|^2 . \tag{2.39}$$

Then, one has to find the vector $\vec{\delta}$ that minimizes our new Φ, by solving $\nabla_\delta \Phi = 0$. This leads to:

$$(\boldsymbol{J}^{\mathrm{T}}\boldsymbol{J})\vec{\delta} = \boldsymbol{J}^{\mathrm{T}}(f(\vec{x}) - f(\vec{x},\vec{p}))\,, \tag{2.40}$$

which is nothing more than a set or linear equations that can be solved easily by inverting the matrix $\boldsymbol{J}^{\mathrm{T}}\boldsymbol{J}$. Here, an important factor to take into account is the

conditioning number of this matrix that we need to inverse, that measures the robustness of the algorithm to the propagation of numerical errors. The nice idea of the LMM consists in the introduction of a damping factor to approximate the Eq. 2.40 and then soften these errors:

$$(\boldsymbol{J}^{\mathrm{T}}\boldsymbol{J} + \lambda \mathbf{diag}(\boldsymbol{J}^{\mathrm{T}}\boldsymbol{J}))\vec{\delta} = \boldsymbol{J}^{\mathrm{T}}(f(\vec{x}) - f(\vec{x},\vec{p}))\,. \tag{2.41}$$

A small value of the damping parameter λ leads to a Gauss-Newton update whereas a large λ results in a gradient descent update. The LMM is thus interplaying between these two methods. The parameter λ is taken with large values in the first steps so that the update of the functions is small. If at a given iteration, the update of Φ leads in a worse approximation than the previous one, then λ is increased in order to approach the Gauss-Newton method, insuring the convergence of the algorithm.

The Principal Axis Method (PRAXIS) was popularized by Richard P. Brent in 1973 [47]. It is a popular derivative-free algorithm (unlike the LMM or the conjugate gradient method) based on finite differences which combines several aspects of the the bisection method, the secant method and inverse quadratic interpolation.

Brent's algorithm for function minimization is based on a set of search directions $\vec{u}_1,..,\vec{u}_n$, for the n parameters, that is repeatedly updated until a set of conjugate direction is reached. Let us set first $\vec{x}_0$ as an initial approximation of the minimum and an initial set of search direction $\vec{u}_1,..,\vec{u}_n$. We compute λ_i to minimize $f(\vec{x}_{i-1}+\lambda_i\vec{u}_i)$ for all i from 1 to n. We then set $\vec{x}_i = \vec{x}_{i-1}+\lambda_i\vec{u}_i$. The search directions are updated as $\vec{u}_i = \vec{u}_{i+}$, for all i from 1 to $n-1$. Then $\vec{u}_n$ is replaced by $\vec{x}_n - \vec{x}_0$, and we compute λ to minimize $f(\vec{x}_0+\lambda\vec{u}_n)$, and, after, $\vec{x}_0$ is replaced by $\vec{x}_0+\lambda\vec{u}_n$. This procedure is repeated until the convergence is reached. If we deal with a quadratic function, the minimum is reached after n iterations. Unlike the LMM, the PRAXIS requires two starting points. Two starting conditions in each variable are required for this method because these are used to define the magnitudes of the vectors $\vec{u}_i$.

In most of the cases, both the LM and the PRAXIS methods gave excellent results with a very accurate fitting of the experimental data. As the system could contain an important set of parameters to fit (~ 18 to fit the two-pulses experiments), the two methods were complementary to select the different initial points and to check the consistency of the results. The intrinsic physical parameters of the sample we have used were optimized first from the data of the single pulse experiment, namely the photon lifetime γ_{C}, the upper polariton decay/dephasing γ_{U}, the coupling strength Ω_{R}, the excitons pumping rate P_b and its decay rate γ_{P_b}. These parameters, listed in Table 2.1, were then fixed to fit the other parameters which depend on the experiment settings. In this way, only few parameters, the pulses intensity $P_c^{(i)}$ and their relative phase ϕ_c (with $c = a,b$ and $i = 1,2$), were let free and whose values remained to determine. The fit was not sensitive to the exciton lifetime, as it is usually two order of magnitude larger than the one of the photon, typically $\gamma_{\mathrm{X}} \sim 1$ ns. While the fitting problem was not trivial and involved global optimization, the results turned out to be surprisingly robust and efficient. This,

we believe, proves the quality of the theoretical model that captures the polariton dynamics which, may be surprisingly, turns out to be extremely fundamental.

2.6 Conclusions

In this Chapter, we have seen the polariton dynamics with an accuracy never observed before. Despite the fact that the Rabi oscillations have been put under close scrutiny since the early days of the field, by Weisbuch himself, attempts at their fitting (by Savona) produced only a fair qualitative agreement [48]. Nowadays, with better samples and better techniques, we are able to witness essentially perfect Rabi oscillations (accurately, normal-mode coupling oscillations), of states that remain coherent throughout, with a loss of visibility of the oscillations much like those observed from two-level systems in genuine quantum superpositions, but due in our case to an altogether different mechanism: the loss of the upper polaritons, bringing the state of the system into a pure condensate of lower polaritons, retaining strong-coupling throughout.

In Section 2.2 we have seen the general formalism to describe exciton-polaritons, through mean-field theories. The main models used by the exciton-polariton community have been briefly introduced. Most of them rely on a Gross-Pitaevskii Equation to describe nonlinear polariton-polariton interactions, which is actually not always necessary, as we have shown in our experiment that are ruled by other factors (dissipation, reservoir, etc.) In order to describe the Lecce experiments, in Section. 2.3, we have developed a quantum-optical model based on a master equation and on the Lindblad formalism. While a fully classical description would be technically possible, the quantum formalism is very convenient to include the various decay and dephasing sources present in a real experiment, without turning to classical formalisms implying, e.g., stochastic terms. We have also seen how the quantum state can be visualised through the Bloch Sphere and the Husimi representation.

The experimental results and their analysis have been presented in Section 2.4. First of all, we introduced the experimental setup and discussed the simple Rabi dynamics (with no decay). The oscillations of the cavity field $|\langle a(t)\rangle|^2$ have been fitted by our model with essentially perfect agreement (Fig. 2.4). The different physical parameters have been obtained from the fit of two series of experiment, informing on the nature and extent of the various mechanisms. The first one consisted in a variation of the energy of excitation ω_L carried by the laser. We have highlighted the major role of the upper polariton dephasing and of the exciton pumping on the Rabi oscillations dynamics (Fig. 2.5). The second one was performed by varying the excitation power, over one order of magnitude by remaining in the linear regime, to avoid nonlinear effects. The system presents a great robustness to the power variations. The results of the two-pulses experiment allowing the coherent control of the Rabi oscillations are given in Section 2.4.4. We have shown how one can, with a judicious choice of parameters, bring the system in

a desired state, such as a polariton (upper/lower), amplifying the oscillations or even annihilating the field. Our optical model was again able to perfectly fit the data. This proof of principle paves the way to further experiments involving more than two pulses, and interesting quantum computation scheme could be obtained by performing this kind of Rabi coherent control at the single-particle level.

Knowing the different parameters allowed us to go theoretically beyond the experiment and deeper in the understanding of the polariton oscillations physics. In Section 2.5, we have studied more in details the central role of the upper polariton radiative decay and pure dephasing. We showed in a fully quantum regime (beyond mean-field) how the population is affected by the amount of pure dephasing, in comparison to only the decay rate (see Fig 2.10). With the optical model, we were also able to reconstruct the full dynamics of the polariton through their four fields, bare states and eigenstates (2.11). It appears again that the upper polariton is the limiting factor that brings the system inevitably in a lower state.

Since this work, further studies have appeared on the Rabi oscillations control. We have already mentioned the work from Chestnov *et al.*(2016) [49] in which a mechanism to get permanent Rabi oscillations for driven-dissipative condensates of exciton-polaritons has been proposed. The authors explained that the permanent non-decaying oscillations may be due to the PT symmetry of the coupled exciton-photon system realized in a specific regime of exciton pumping. We have emphasized however that one must bear in mind the difference between normal-mode coupling (an essentially classical effect) and genuine Rabi oscillations (involving a quantum superposition and entanglement). Notably, we must also mention the work of Voronova *et al.*(2015) [50] on the effect of detuning on the exciton-photon oscillatory dynamics. In this text, the full measure of the Rabi dynamics as seen from the viewpoint of two coupled condensate was made to bring the problem into the thematics of Bosonic Josephson oscillations, namely, of the internal type since internal degrees of freedom are coupled (here the exciton and photon fractions). These authors have shown that a nonzero detuning induces nontrivial patterns of oscillations between the relative phase of ψ_C and ψ_X and linked this observation to the celebrated Bosonic Josephson Junctions. Their work, in turn, inspired further studies from Rahmani and Laussy who deepened even further the connection between Rabi and Josephson dynamics. As simple as it might seem to be, the problem of polariton Rabi oscillations is therefore still an ongoing one, and this thesis, while providing its most comprehensive account to date, is certainly not exhausting it.

Chapter 3

Polarization Shaping with Polaritons

L'opinion est le crépuscule, la science est le jour,
et l'ignorance la nuit.
Voltaire, Les pensées philosophiques.

Contents

In the previous Chapter, I presented the Rabi dynamics from a fundamental point of view. In this Chapter, I apply this knowledge to realize a new kind of light, whose polarization can vary temporally to cover selected areas of the Poincaré sphere. The results presented here have also been experimentally demonstrated by my colleagues of Lecce and fitted with an extended version of the quantum optical model presented earlier. This work gave rise to a publication in the *Nature* review *Light: Science and Applications* (see reference 2 page 131).

3.1 Introduction

The control and the manipulation of light has been one of the main goals in the history of physics. The vectorial nature of light can be perceived through its phase and amplitude, but a great insight is reached by looking at its polarization state. The polarization is a property of light known since the XVIIth century and it has been extensively used in plenty of scientific fields. Historically, experiments based on polarized light have contributed to major advances in optics, of course, giving precious clues on the oscillatory nature of light (Young 1817), but also in astronomy. We can mention for example the discovery of the linear polarization of the light emitted from the solar corona (Liais 1858) or from the M31 galaxy (Öhman 1942). Many other examples in chemistry, biology or geology could be given. Thus, the development of a source emitting an arbitrary polarized light is an important step. Even with the modern development of lasers and coherent sources of light, achieving the control and the manipulation of the polarization at the scale of the femtosecond is still an ongoing research problem.

Almost two decades ago, a new area of light's manipulation was opened by Brixner and Gerber (2001) [51] who demonstrated the first realisation of a light pulse whose intensity, momentary frequency and polarization can vary in time and being computer-controlled at the scale of the femtosecond. Thereby was opened the era of "polarization pulse shaping" with a huge number of potential applications.

Another class of polarized beams has been theoretically developed later in order to cover the whole Poincaré sphere of polarization. The so-called *"Full Poincaré Beams"* have been introduced by Beckley *et al.* (2010) [52] and consists in a superposition of a Gaussian mode and a spiral-phase Laguerre-Gauss mode having orthogonal polarizations. In this case, and unlike the Brixner pulses, all the polarization states are displayed spatially into the beam.

Last year, Alexei Kavokin made an interesting proposal to link these two concepts of polarized light by using the oscillating property of the microcavity polaritons. By combining two Rabi-oscillating and orthogonally polarized polaritonic fields, one could theoretically obtain a tunable and time-varying source of polarized light that can cover entirely the Poincaré sphere. This principle was then experimentally demonstrated by my colleagues in Lecce. It shows the emission of time varying polarized light, that, for instance, can cover a whole hemisphere of

the Poincaré sphere. This insightful idea still required a formalism to provide an accurate description of the dynamics, that are more subtles in their full complexity and generality than it appears from the mere statement of the basic principle. The formalism itself is simply the linear superposition of the solutions presented in the previous Chapter for unpolarized Rabi oscillations. The experimental data have been fitted with such an updated version of our quantum-optical model, extended to the polarized case, and indeed showed a perfect agreement between theory and experiment. The theory also allowed to provide the ideal excitation conditions to reach the full-Poincaré-beam limit.

This Chapter is organised as followed. In Section. 3.2, I give an overview of the different kinds of polarized light that have been developed in the past years. I detail the two main approaches that are the polarization pulse shaping, in the sense of Brixner, and the full Poincaré beams. I then present the way to obtain with polaritons a new kind of light, sharing and combining some aspects of the two previous kinds.

Section 3.3 is devoted to the theoretical model we have developed to describe this polarized light and fit the experimental results. As this model can be viewed as an extension of the one developed for the unpolarized case, and because of their similarities, we will refer many times to Section 2.3.1 of Chapter. 2. We show how the superposition of simple polarized Rabi oscillating beam results in oscillations of the emitted light's polarization.

In Section 3.4, I describe the trajectories obtained on the Poincaré sphere, that are circles in the conservative case and swirling trajectories when the particles decay is taken into account. All the initial and final points of the trajectory on the sphere can be parametrized exactly as functions of the initial quantum state of the system. Such a parametrization is one important result of the model. For this purpose, I explain in Section. 3.4.4 how to prepare the states corresponding to any desired trajectories with realistic parameters, and I explain the different constrains.

In Section 3.5 are presented the results of the polarized Rabi experiment obtained in Lecce. It demonstrates the technological feasibility to produce such a kind of light, with the generation of polarized beams covering temporarily selected areas of the Poincaré sphere, like a whole hemisphere. This result is discussed as a proof of principle and I discuss the advantages of this technique and its possible extensions.

The last Section 3.6 contains the main conclusions of this Chapter.

3.2 Polarized light sources

In this Section, we dress a short overview of the different kinds of polarized light pulses that have been developed in the last years. We detail the principles on which is based the polarized pulses shaping that Brixner developed to produce femtosecond time-varying polarized light. In the same way, we present the theoretical description of the *Poincaré beams*.

3.2.1 Polarization shaping

The first realization of a shaped pulse produced light whose intensity, momentary frequency and light polarization were varied as a function of time in a timescale of femtoseconds. This was reported by Brixner and Gerber in 2001 [51]. Before that, only simple polarization profiles could be achieved by using interferometric combinations of two polarization components. It has been demonstrated by Zhuang *et al.*(1997) [53] that a stack of three homogeneous nematic liquid-crystal cells, or Liquid-Crystal display (LCD) could be used as a controller to bring any state of polarization of light from one arbitrary state to another. The idea of Brixner and Gerber was thus to build a device based on a set of many-pixel (256) two-layer LCDs to obtained a time varying polarized light, each pixel changing the state of polarization (SOP). By applying a suitable voltage to the separated pixels, one tune individual frequency intervals throughout the laser spectrum. The phases differences leasing to a complex polarization-modulated laser pulses in the time domain. The desired sequence of voltage modulations, that correspond to the various SOPs, can be computer-controlled with a corresponding algorithm.

The range of applications is potentially huge since the interaction between light and matter is polarization sensitive. This technique was thus used to increase the performances of many applications based on polarization. In a later study, Brixner *et al.* (2004) [54] reported the ionization of potassium dimer molecules, where dipole transitions are favoured by different directions of the exciting laser field. With this example, we understand directly the advantages of having a single laser beam whose polarization varies in time. Polarization pulse shaped lasers are also an efficient method for nano-optical manipulation. Aeschlimann *et al.*(2007) [55] have achieved subwavelength dynamic localization of electromagnetic intensity on the nanometre scale, overcoming the spatial restrictions of conventional optics by using adaptive polarization shaping of femtosecond laser pulses. This technique has also been used for the generation of ultrashort laser pulse pairs, whose time delay between them is controlled with a zeptosecond precision [56]. Dozens of other further studies based on this principle have been done in the last fifteen years, feeding a rich literature.

This technique of pulse shaping allows one to reach a huge variety of different time varying polarized pulses, but it suffers also from some limitations. The number of SOP contained in the resulting pulse depends directly on the number of LCD, as they are independently tuned to obtain the desired ellipticity. This cannot be enough to cover entire parts of a Poincaré sphere. It also requires a complex setup, involving LCDs, all-reflective zero-dispersion compressor, interferometers and computer resources, the desired polarization being computed with special algorithms.

3.2.2 Full Poincaré Beams

Unlike the pulse shaping technique developed by Brixner, which provides a pulse's polarization varying in time, an other kind of beam has been designed to contain a time-independent but spatially varying polarization. The so-called cylindrical-vector beams have been distinguished by their spatially non uniform polarization [57]. When all the SOP are provided to cover the whole Poincaré sphere of polarization, such beams thus realised *Full Poincaré beams*. They have been introduced by Beckley *et al.* (2010) [52]. Such beams can span the entire surface of the Poincaré sphere in a way that the coverage is conserved under propagation. They also demonstrate advantages in similar endeavors, such as boosted scattering or sub-wavelength localization. The Full Poincaré (FP) beams consist in a superposition of a Gaussian mode and a spiral-phase Laguerre-Gauss (LG) mode having orthogonal polarizations. The lowest order scalar LG beam is actually a Gaussian beam, expressed as:

$$L_{00}(\vec{r}) = \frac{l_0}{\xi(z)} \exp\left(ikz - \frac{x^2+y^2}{\omega_0^2 \xi(z)} \right), \tag{3.1}$$

where l_0 defines the beam amplitude, ω_0 its waist size and $\xi(z) = 1 + 2iz/k\omega_0^2$. This function taken at the next order to carry an angular momentum reads:

$$L_{01}(\vec{r}) = \sqrt{2} \frac{x+iy}{\omega_0 \xi(z)} L_{00}(\vec{r}). \tag{3.2}$$

A general family of FP beams is thus defined as:

$$E(\vec{r}, \gamma) = \cos(\gamma)\vec{e_1} L_{00}(\vec{r}) + \sin(\gamma)\vec{e_2} L_{01}(\vec{r}), \tag{3.3}$$

with $\vec{e_1}$ and $\vec{e_2}$ two arbitrary orthogonal unit polarization in the x–y plane. The parameter γ was introduced to regulate the intensity profile of the beam. It can be demonstrated that such beams of Eq. 3.3 have a polarization at each point of any tranverse plane that covers the surface of the Poincaré sphere. This has been as well demonstrated experimentally [52].

An other proposal has been made to generate arbitrary space-varying vector beams with structured polarization and phase distributions [58]. Beckley *et al.* (2012) [59] have also proposed a partially polarized version of their beam, spanning a disk-like region within the Poincaré sphere, which rotates during propagation, covering again the full sphere.

As in the previous case, plenty of applications arose from these new polarized beams, such as in optical trapping, laser machining, high-resolution metrology, or electron acceleration [60].

3.2.3 Polarized Light with Polaritons

We now come to the way to obtain time-varying polarized light with exciton-polaritons. In 2015, Alexey Kavokin from Southampton University, maybe the

most renowned experts on the topic of polaritons polarization, made an interesting proposal to generate new states of light by using this most fundamental of properties from the polaritons, their Rabi oscillations. The idea is the following: a light whose polarization is varying in time can be emitted from a microcavity by exciting it with two orthogonally polarized pulses and with a suitable time delay between them. Working with orthogonally polarized pulses ensures that no interactions between the fields of different polarizations will occur. The superposition of the oscillating fields results in the precession of the Stokes vector of the emitted light. Polaritons being particles with finite lifetime, it results in a drift of the polarization from a circle on the Poincaré sphere (whose radius and position can be controlled) to a single point at long time. This leads to the generation of a new kind of polarized light, suitable to cover selected area of the Poincaré sphere, and possibly the whole sphere, in a range of a few picoseconds. This effect would thus provide both of the mechanisms we have mentioned before, namely (i) full Poincaré beams, (ii) in time. The effect has been demonstrated as a proof of principle with microcavity polaritons at the femtosecond time scale by my colleagues of Lecce. But as it relies on the Rabi oscillations, thus it could be transposed and obtained with other platforms exploiting the same property. This aspect will be discuss in the Section. 3.5.3.

3.3 Quantum Optical Model for Polarized Rabi Oscillating Light

In this Section, we present an extended version of the quantum optical model we have developed in the Chapter 2 to describe the Rabi oscillations coherent control experiment. Instead of sending two pulses in the same state of polarization as we did before in order to control the quantum state of the particles, we send this time two pulses with orthogonal polarizations, that are furthermore non-interacting so their combination is simply vectorial addition of their polarization. We show the different trajectories on the Poincaré sphere that one can obtained with this light and how to prepare the corresponding initial states to achieve it.

3.3.1 Theoretical Description of Light

The time-varying polarization of this light arises from the coherent superposition of two fields of different polarizations. Both of these fields arise themselves from the light-matter coupling present in the microcavity and are thus in a regime of Rabi oscillations. So we are actually dealing with four fields, two coupled photon-excitons fields in a different state of polarization, say left ($\circlearrowleft$) and right ($\circlearrowright$) circular polarization. As long as the two fields are in orthogonal states of polarization, they are not interacting between them. Also, the effect is obtained in the linear regime of excitation, at low pumping, in which no polariton-polariton interactions are involved. We can thus describe the system with four complex amplitudes α_p and β_p

with $p = \circlearrowleft, \circlearrowright$ the state of polarization of the photonic (α) and excitonic (β) fields. In the quantum regime, they describe a probability for the quantum states $|i,j\rangle_p$, with a determined number of photons i and material excitons j in the polarization p. The general wave function describing these states can thus be written as:

$$|\psi(t)\rangle_{\mathrm{Q}} = \left(\alpha_p(t)\,|0,1\rangle_p + \beta_p(t)\,|1,0\rangle_p\right) \otimes \left(\alpha_q(t)\,|0,1\rangle_q + \beta_q(t)\,|1,0\rangle_q\right), \tag{3.4}$$

where the polarizations q and p are orthogonal.

These states of light can be also perfectly described in the classical regime as electromagnetic waves, directly through their respective amplitudes and phases. In this case, the states are written in any of the familiar forms to represent polarization, such as Stokes or Jones vectors. In terms of the latter, the state of polarization reads:

$$\begin{pmatrix} \alpha_{\leftrightarrow}(t) \\ \alpha_{\updownarrow}(t) \end{pmatrix} = \frac{\alpha_{\circlearrowleft}(t)}{\sqrt{2}} \begin{pmatrix} 1 \\ i \end{pmatrix} + \frac{\alpha_{\circlearrowright}(t)}{\sqrt{2}} \begin{pmatrix} 1 \\ -i \end{pmatrix}. \tag{3.5}$$

However, as we did before in Chapter 2 and following the same arguments, we will use the quantum formalism. Indeed, we will follow the same reasoning, knowing that the quantum formalism is more general and unifies both regimes, and that for technical reasons, due to the particular experimental setup, we have to deal with incoherent pumping and dephasing that are more conveniently treated in this form.

By considering a basis of coherent states:

$$|\alpha_p\rangle = \exp(-|\alpha_p|^2/2) \sum_{k=0}^{\infty} \alpha_p^k\,|k\rangle\,/\sqrt{k!}, \tag{3.6}$$

we can now rewrite our four fields wave function of Eq. 3.4 in this basis, that gives:

$$|\psi(t)\rangle_{\mathrm{C}} = \left|\alpha_{\circlearrowleft}(t), \beta_{\circlearrowleft}(t)\right\rangle \otimes \left|\alpha_{\circlearrowright}(t), \beta_{\circlearrowright}(t)\right\rangle. \tag{3.7}$$

From the last expression, we see that no quantum superposition or any other quantum effects are involved. The quantum dynamics of the fields is describe by a similar Hamiltonian than the one used in the previous Chapter, it reads:

$$H_0^p = \sum_p \frac{\hbar\Omega_{\mathrm{R}}}{2} (a_p^\dagger b_p + a_p b_p^\dagger), \tag{3.8}$$

for the ladder operators a_p (for the photon) and b_p (exciton), with $\Omega_{\mathrm{R}}/2$ the coupling strength. It differs slightly from Eq. 2.8 in Chapter 2 since we work directly in the rotating frame here. As we know, the coupling between the photons and the excitons gives rise to two new modes:

$$u_p = \frac{a_p + b_p}{\sqrt{2}}, \tag{3.9a}$$

$$l_p = \frac{a_p - b_p}{\sqrt{2}}, \tag{3.9b}$$

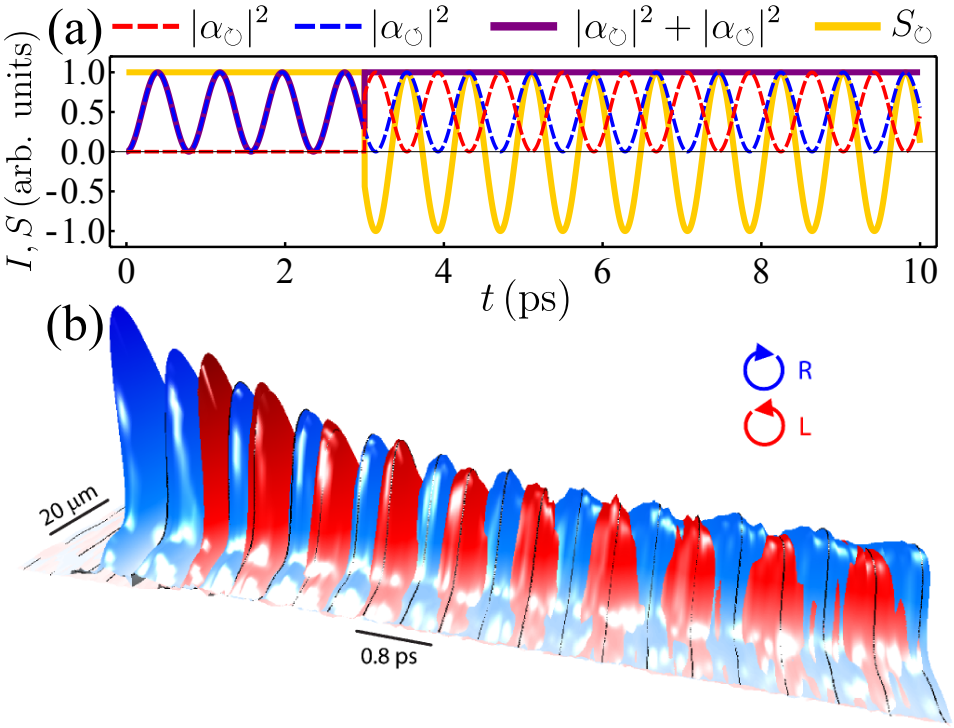

Figure 3.1: (a) Polarized Rabi oscillation obtained theoretically from Eq. 3.14. The system evolves in the $\circlearrowleft$ polarization till $t \approx 3$ ps (blue dashed line), resulting in an oscillating total intensity (purple line) and in a constant circular DOP (yellow line). Then a second field in the orthogonal polarization $\circlearrowright$ is brought (dashed red line), reversing the pattern of oscillations, *i.e.* inducing a constant total intensity and a varying circular DOP. (b) Experimental observation of the effect through the cavity field (along the diameter of the Gaussian spot of 20 µm a 10 ps duration) with left (red) and right (blue) circular polarization as a false color plot.

the upper and lower polariton, respectively. The light intensity emitted by the cavity in a given polarization basis p is thus directly given by $\langle a_p^\dagger a_p \rangle$. We also define an important quantity, namely the circular degree of polarization (**DOP**):

$$S_p = (\langle a_p^\dagger a_p \rangle - \langle a_q^\dagger a_q \rangle)/(\langle a_p^\dagger a_p \rangle + \langle a_q^\dagger a_q \rangle)\,, \tag{3.10}$$

whose value varies between -1 and 1. It gives directly the proportion of the polarization of the light. For example, $S_{\circlearrowright} = 1$ means that the light is at 100% in the polarization $\circlearrowright$, while $S_{\circlearrowright} = -1$ means a light polarized 100% in $\circlearrowleft$, and $S_{\circlearrowright} = 0$ means being polarized 50% in both $\circlearrowleft$ and $\circlearrowright$.

All the previous definitions can be written in an other polarization basis through the relationships:

$$a_{\leftrightarrow} = (a_{\circlearrowleft} + a_{\circlearrowright})/\sqrt{2}, \tag{3.11a}$$

$$a_{\updownarrow} = i(a_{\circlearrowleft} - a_{\circlearrowright})/\sqrt{2}, \tag{3.11b}$$

$$a_{\nearrow/\searrow} = ((1 \pm i)a_{\circlearrowleft} + (1 \mp i)a_{\circlearrowright})/2. \tag{3.11c}$$

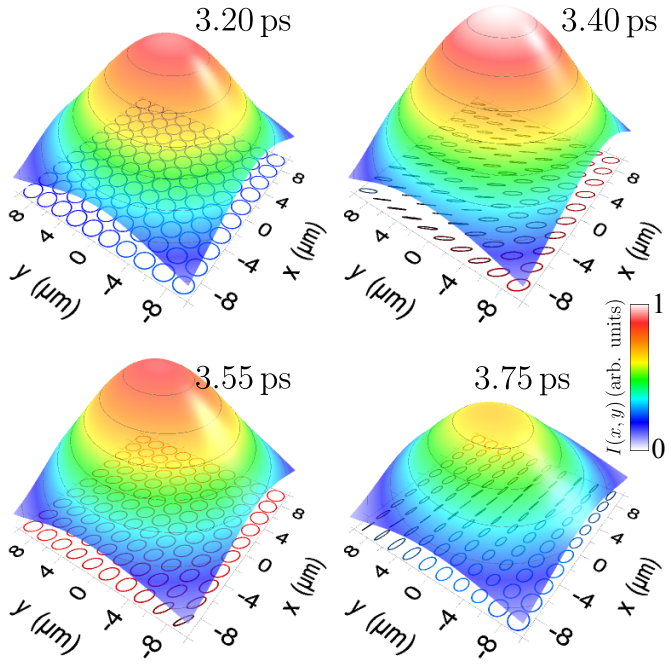

Figure 3.2: Spatial distributions of the density and polarization at 200 fs time intervals during one of the initial cycles after the second pulse arrival. The emitted intensity remains roughly constant while the resulting polarization is strongly affected by the Rabi oscillations. The polarization can also be made homogeneous or not spatially.

These relationships are suitable both in the quantum formalism and in the classical one with the Jones calculus.

The pulse excitation is described with the following Hamiltonian:

$$H_{\Omega}^{p} = \sum_{p} \sum_{c=a,b} P_c(t) e^{i\omega_{\mathrm{L}} t} e^{i\phi_c} c_p^{\dagger} + \mathrm{h.c.}\,, \tag{3.12}$$

where the pulses $P_c(t)$ are sent at the laser frequency ω_{L} and carrying a phase ϕ_c, with $c = a, b$ and in the polarization p.

The total Hamiltonian of the system reads:

$$H^{p} = H_0^{p} + H_{\Omega}^{p}\,. \tag{3.13}$$

The system can be solved analytically in a simple way by considering as initial conditions the fields with amplitudes $\alpha_{p,q}(0)$ and $\beta_{p,q}(0)$ instead of a pulse excitation. Their time evolution will thus follow:

$$\alpha_p(t) = \alpha_p(0)\cos\left(\frac{\Omega_{\mathrm{R}} t}{2}\right) - i\beta_p(0)\sin\left(\frac{\Omega_{\mathrm{R}} t}{2}\right). \tag{3.14}$$

One can see typical polarized Rabi oscillations in Fig. 3.1. On the panel (a) are plotted the photonic field intensities in the different polarizations, their sum and

the circular DOP. In this case, the system is prepared in a single polarization $\circlearrowleft$. We see the Rabi oscillations on the photonic field $|\alpha_{\circlearrowleft}|^2$ (in blue), that induces a constant DOP (in yellow). At $t \approx 3$ ps is sent another excitation in the $\circlearrowright$ polarization, created new polarized Rabi oscillations. This new field is brought in a way such that the total fields intensity $|\alpha_{\circlearrowright}|^2 + |\alpha_{\circlearrowleft}|^2$ remains constant. On can see how now the circular DOP varies while the total intensity is constant in time. This is the heart of the effect. The superposition of non-interacting Rabi oscillating polarized fields leads to the generation of light whose polarization varies temporarily. In Fig. 3.1(b) is shown an experimental observation of the effect. The sample is excited with a 20 μm spot and the cavity field is detected in both left (red) and right (blue) circular polarizations. The main difference with the theoretical case of panel (a) is the exponential decay of the signal, due to the leakage of the photons out of the cavity. This can be treated mathematically exactly as we did in the Chapter 2, by using the Lindblad formalism.

We also point out that in the present experiment, we have used essentially spatially homogeneous profiles. This can be seen in Fig. 3.2 on the space-time charts, where the polarization is measured to be essentially the same in the region covered by the polarized beam. There are however no restrictions to work with a spatially dependent polarization that could be combined with the temporal dynamics.

3.3.2 Dissipative Channels

We know how the different decay sources and dephasing present in this polariton system affect the Rabi oscillations patterns and the quantum state of the particles. Without surprises, they have also a strong effect on the polarization of the light emitted from the cavity. We use again the Lindblad formalism that is introduced in the master equation as [61]:

$$\dot{\rho} = i[\rho, H] + \mathscr{L}\rho\,, \tag{3.15}$$

for the four-fields density matrix, with $\mathscr{L}\rho$ a sum of super-operators

$$\mathscr{L}_c\rho = 2c\rho c^\dagger - c^\dagger c\rho - \rho c^\dagger c\,, \tag{3.16}$$

for the generic operator c. We include here as well the main ingredients that act on the polariton dynamics, namely the radiative decay rates of the bare fields $\gamma_{a,b}$, the incoherent pumping P_b from the exciton reservoir, the upper polariton decay rate $\gamma_{\mathrm{U}}^{\mathrm{R}}$ and pure dephasing $\gamma_{\mathrm{U}}^{\phi}$. We are thus brought to a Liouvillian in the form [44]:

$$\mathscr{L}\rho = \sum_{p=\circlearrowright,\circlearrowleft} \left[\frac{\gamma_a}{2}\mathscr{L}_{a_p} + \frac{\gamma_b}{2}\mathscr{L}_{b_p} + \frac{P_b}{2}\mathscr{L}_{b_p^\dagger} + \frac{\gamma_{\mathrm{U}}^{\mathrm{R}}}{2}\mathscr{L}_{u_p} + \frac{\gamma_{\mathrm{U}}^{\phi}}{2}\mathscr{L}_{u_p^\dagger u_p} \right]\rho\,. \tag{3.17}$$

We remind that the introduction of these relaxation parameters is motivated by the experiment and is needed to reproduce it quantitatively. We refer to Chapter 2 for

further details on the physical effect of the different parameters. The field amplitudes dynamics can again be solved analytically. For the observables of interest, the solution remains fully defined by complex amplitudes:

$$\alpha_p(t) = \Bigg[\alpha_p(0)\cosh(Rt/4) - \left(\frac{\beta_p(0)G + \alpha_p(0)\Gamma}{R}\right)\sinh(Rt/4) \Bigg] \exp(-\gamma t/4)\,, \quad (3.18)$$

where, for our particular choice of dissipative channels:

$$\gamma = \gamma_a + \gamma_b + \gamma_U - P_b\,, \qquad \Gamma = P_b - \gamma_b + \gamma_a\,, \quad (3.19a)$$

$$G = 2i\Omega_R + \gamma_U\,, \qquad R = \sqrt{G^2 + \Gamma^2}\,, \quad (3.19b)$$

$$\gamma_U = \gamma_U^R + \gamma_U^\phi\,. \quad (3.19c)$$

3.4 Polarization Dynamics

In this Section, we see how the polarization dynamics arises thanks to the polariton dynamics powered by the Rabi oscillations. We study theoretically which are the trajectories on the Poincaré Sphere of polarization obtained form the superposition of two Rabi oscillating photonic fields.

3.4.1 Closed trajectories on the Poincaré Sphere

We have seen before how the quantum states of the polaritons could be well displayed on the Bloch Sphere. In the same way, the polarization dynamics can be conveniently pictured on the Poincaré Sphere of polarization. In this case, instead of using a photonic field $\langle a(t)\rangle$ and an excitonic field $\langle b(t)\rangle$, we calculate the trajectories from two polarized photonic fields $\alpha_p(t)$ and $\alpha_q(t)$, where p and q are orthogonal polarizations. The orientation of the sphere is thus given by the polarization basis from which the trajectories are computed. In this case, the north pole of the sphere corresponds to the p polarization and the south pole to the q one. In the following, we will always display the Poincaré Sphere in the circular polarization basis ($\circlearrowleft$, $\circlearrowright$), as it was the basis chosen for the experiment.

The simplest trajectories on the Poincaré Sphere are circles. They correspond to polarization oscillations from two photonic fields without decay or with the same decay rate, as the polarization is given by the sum of their intensities. This can be seen on Fig. 3.3 in green, where various circles are realised from an equator for full-amplitude Rabi oscillations (a) down to a single point for polaritons in both polarizations (b). The orientation and the position of the circles depend on the polariton states chosen in the two polarizations. The circle thus formed can be defined on the sphere, in a given basis (we keep the circular one) by two couples of angles

(θ_ξ, Φ_ξ), for $\xi = \alpha,\ \beta$, defined by the ratios of polarization $R_\alpha = \alpha_{\circlearrowleft}/\alpha_{\circlearrowright}$ and $R_\beta = \beta_{\circlearrowleft}/\beta_{\circlearrowright}$ of the photon α and matter β fields at $t = 0$, respectively. The angles can thus be obtained by geometric constructions (see Section 2.3.3 of Chapter 2) as:

$$\theta_\xi = 2\arccos(1/\sqrt{1+|R_\xi|^2}), \tag{3.20a}$$

$$\Phi_\xi = \phi_\xi + \arg R_\xi . \tag{3.20b}$$

In Fig. 3.3(c), we show a case with $\Phi_\xi = 0$, $\theta_\alpha = \pi/4$ and $\theta_\beta = 3\pi/4$. Each loop over this circle corresponds to one period of oscillations, which is 800 fs in our experiment. We have also mentioned the case of the panel (b), where the circle reduces to a single point, defining a polariton, *i.e.* an eigenstate of the system that does not involve a temporal dynamics. In this case $\theta_\alpha = \theta_\beta$ and $\Phi_\alpha = \Phi_\beta$.

3.4.2 Swirling on the Poincaré Sphere

We can now take advantage of a feature that is usually regarded as a shortcoming of microcavity polaritons, but that in our case will turn the simple effect just proposed into a mechanism that powers a new type of light. We have already discussed the significant lifetime imbalance between the two types of polaritons. We know that the upper polariton $|\mathrm{U}_p\rangle = |\alpha_p, \alpha_p\rangle$ enjoys a much shorter lifetime than its homologue the lower polariton $|\mathrm{L}_p\rangle = |\alpha_p, -\alpha_p\rangle$, regardless of the polarization p. From the fits realised on the previous experiment, we have found the upper polariton lifetime is typically of the order of 2 ps while it is of the order of 10 ps for the lower polariton. However these short values can be now tuned by orders of magnitudes in different samples. As an example, microcavities presenting particles lifetime of the order of the hundred of picoseconds have been demonstrated by M. Steger *et al.*(2013)[62]. In our case, the lifetime imbalance between the polaritons leads to time-dependent Rabi oscillations converging toward a monotonously decaying signal as the population of the upper polaritons "evaporates" and only lower polaritons remain, see Section 2.5.2 of Chapter 2 for further details. The decay of the polariton fields leads to a continuous drift on the Poincaré sphere, starting by describing the initial circle of the Rabi dynamics in the absence of dissipation, toward a final point defined by the polarized lower polaritons. This has, as an interesting consequence, the emission of a light "visiting" a plethora of states of polarization. In Fig. 3.3 are shown various cases spanning different areas of the Poincaré sphere. One can see how the polarization evolves, starting from the green cicles and drifting (in blue) on the sphere toward the final state, pointed by red arrows. By choosing wisely the parameters, one can obtain the case of panel (b), where a full mapping of the sphere is realized from one pole to the other. In this case, the initial circle is reduced to a single point, and the time to drift between the two poles directly depends on the lifetime of the particles. More the lifetime is short, more the time needed to drift from one pole to the other is small. Thus, a longer lifetime provides a higher covering of the sphere. Such a case provides a full Poincaré beam in time.

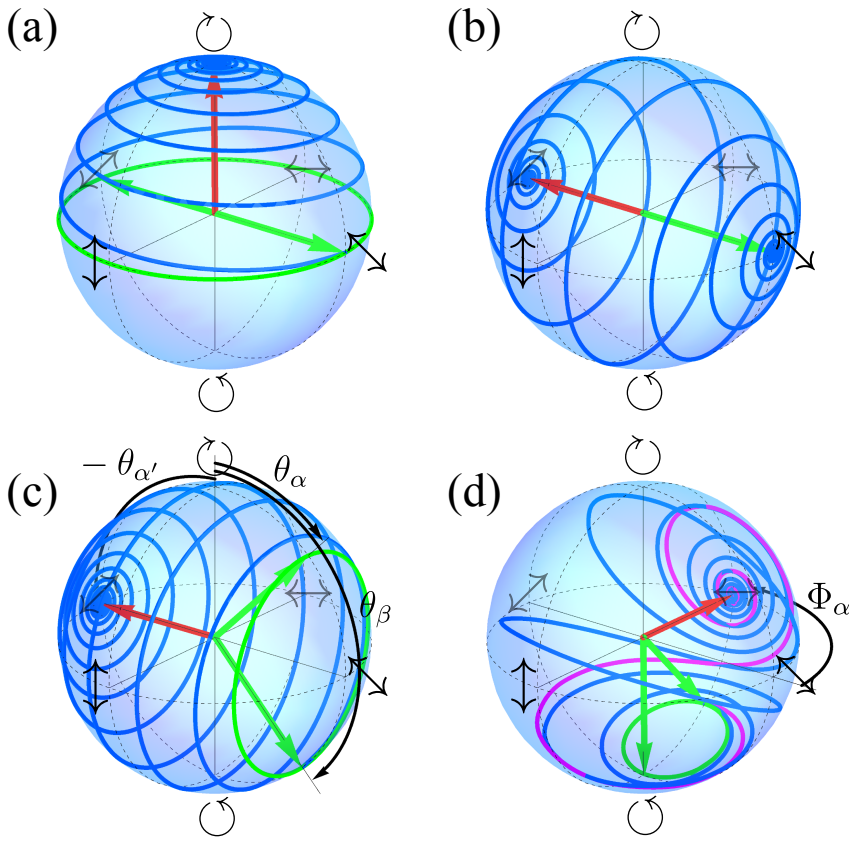

Figure 3.3: Polarization dynamics on the Poincaré sphere (theory). The green arrows, defined by the angles θ_α and θ_β, fix the circle of polarization in absence of decay ($\gamma = 0$) by intersecting the meridian of azimuthal angle ϕ_α. The red arrow, defined by the angle θ'_α, fixes the point of long-time polarization. In presence of decay, $\gamma \neq 0$, the trajectory of the polarization, in blue, drifts from the green circle to the red final point. (a) Span of the northern hemisphere of the Poincaré sphere in circular polarization, by setting $R_\alpha = 1-\varepsilon$, $R_\beta = -1$ and $R'_\alpha \to \infty$ with $\varepsilon \to 0$. (b) Span of the full Poincaré sphere from the ↘ to the ↗ pole, by setting $R_\alpha = 1-\varepsilon$, $R_\beta = 1+\varepsilon$ and $R'_\alpha = -1$ for $\varepsilon \to 0$. (c) Span of the Poincaré sphere excluding a spherical cap of antidiagonal polarization, by setting $R_\alpha = 0.41$, $R_\beta = 2.41$ and $R'_\alpha = -1$. (d) Distorted spanning of the sphere by choosing close initial and final points, by setting $R_\alpha = 0$, $R_\beta = -2/3$, $R'_\alpha = 1$ and $\Phi_\alpha = \pi/2$. Parameters common to all cases: blue trajectories with $\gamma = 1$ and the purple trajectory with $\gamma = 3$.

3.4.3 Final State of Polarization

The final state of polarization can be parametrized in the same way as the initial one without decay—with a couple of angles $(\theta'_\alpha, \Phi'_\alpha)$—by making a rotation of the polariton basis. This introduces the parameters $\alpha'_p = (\alpha_p - \beta_p)/\sqrt{2}$ and $R'_\alpha = \alpha'_{\circlearrowleft}/\alpha'_{\circlearrowright}$ from which one obtains the angles:

$$\theta'_\alpha = 2\arccos\left(1/\sqrt{1+|R'_\alpha|^2}\right), \tag{3.21a}$$

$$\Phi'_\alpha = \phi_\alpha + \arg R'_\alpha, \tag{3.21b}$$

obtained similarly than Eqs. 3.20. Indeed, the state converges to the polarization of the lower polariton, which is obtained by making a change of basis, or equivalently a rotation on the sphere. In this way, the final point (red arrows) correspond to the initial one calculated in the polariton basis.

Any polarization trajectory can thus be defined by three (possibly complex) numbers: R_α and R_β for the initial point and $R_{\alpha'}$ for the final point. To obtain the desired polarization trajectory, we thus have to define the way to bring the system into the states $|\alpha_p, \beta_p\rangle$ with a pulsed excitation, as it is the way the microcavity is excited. These states are obtained from the different parameters ratios R through the relations:

$$\beta_{\circlearrowleft} = \frac{R_\alpha - R_{\alpha'}}{R_\beta - R_{\alpha'}} \alpha_{\circlearrowleft} , \tag{3.22a}$$

$$\alpha_{\circlearrowright} = R_\alpha \alpha_{\circlearrowleft} , \tag{3.22b}$$

$$\beta_{\circlearrowright} = R_\beta \frac{R_\alpha - R_{\alpha'}}{R_\beta - R_{\alpha'}} \alpha_{\circlearrowleft} , \tag{3.22c}$$

for an arbitrary (nonzero) $\alpha_{\circlearrowleft}$.

3.4.4 Preparation of the Initial State

The preparation of the initial state can be easily achieved for coupled oscillators (assumed here at resonance for simplicity) excited with Gaussian pulses [63]. We remind that the pulse excitation scheme is given by the Hamiltonian H_Ω^p in Eq. 3.12. Consequently, the laser frequency has to be adjusted as follow:

$$\omega_{\mathrm{L}}^p = \frac{\sigma^2}{\Omega_{\mathrm{R}}} \ln \frac{|\alpha_p + \beta_p|}{|\alpha_p - \beta_p|} . \tag{3.23}$$

If one looks on the Bloch Sphere that describes the quantum state, the system evolves in time, in absence of dissipation, in a circle parallel to the equator (with lower and upper polaritons as south and north poles, respectively), as shown in Fig. 3.4(b). It is therefore enough to prepare the corresponding circles, in both polarizations, with an adjustable time-delay $\Delta\tau = R_\alpha/(\Omega_{\mathrm{R}}|R_\alpha|)$ between them so that at any moment in time, the two points on the respective circles have the phase relationship of Eqs. 3.22. The time delay should be small enough to maintain the first polarization closed to the circle defined by the first pulse, which is always possible whenever the optical frequency is much higher than the Rabi frequency. The angle of one circle that results from a pulse of frequency ω_L and width in frequency σ is given by:

$$\theta = 2 \arccos\left(1 / \sqrt{1 + \exp\left(\frac{2\Omega_{\mathrm{R}} \omega_L}{\sigma^2} \right)} \right) . \tag{3.24}$$

This can be seen in Fig. 3.4(a). Broad pulses require large detuning from the polaritons to span all the Bloch sphere while sharp pulses result in a step function,

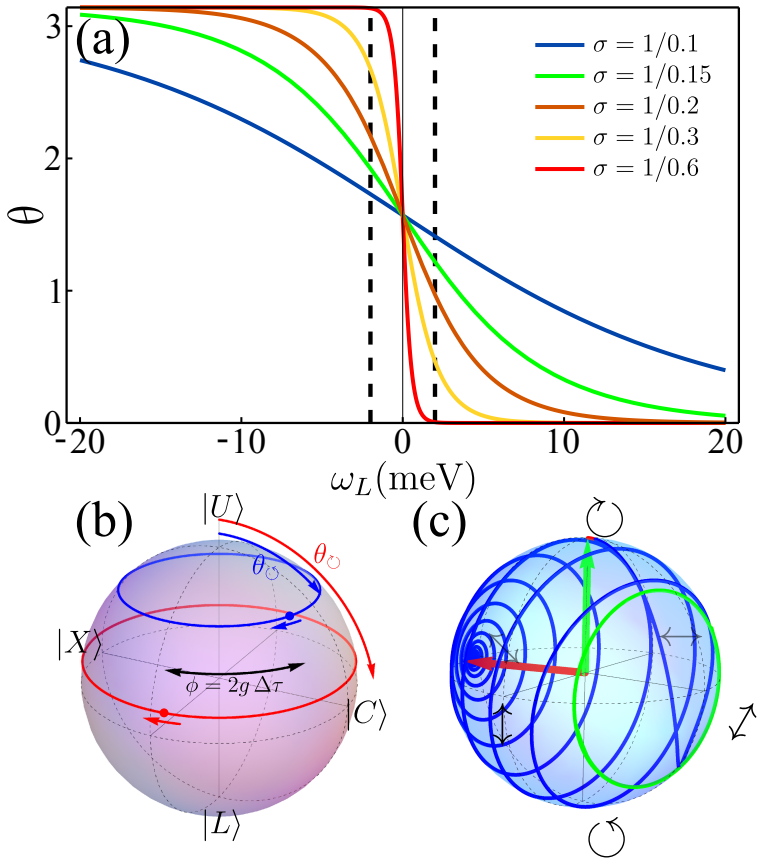

Figure 3.4: (a) Energy of the laser pulse ω_L to prepare a state $|\alpha\beta\rangle$ defined by an angle $0 \leq \theta \leq \pi$ on the Bloch sphere, for various pulse widths in frequency σ. The dashed vertical lines show the two polariton resonances. The green trace corresponds to the experiment. A good compromise is obtained for widths of half size, with all angles θ realized for excitations close to the polariton resonances. (b) The states in both polarization describe circles on the Bloch sphere, going round at the Rabi frequency. The relative phase is shown here at a given (arbitrary) time as two points along their trajectory. (c) Numerical simulation with two pulses corresponding to the case of Fig. 3.3(c) that was obtained for an initial condition. The green arrow corresponds to the first pulse and the red one to the sought final state.

with pure LP excitation below resonance, pure UP excitation above and bare-state excitation in between. A good compromise is found for pulses width $\sigma \approx \Omega_R$. The absolute phase of the first pulse is random and plays no role. However the relative phase between the pulses is important and adjustable by the time-delay between them, as shown in Fig. 3.4(b). For a zero time delay, or a multiple of the Rabi periods, the two states would be perfectly in phase. For the scheme to work, one only needs that when the second pulse arrives, the state left by the first one, in the other polarization, has not departed significantly from its circle, so that the

parameters $(R_\alpha, R_\beta, R_{\alpha'})$ are accurately defined. This is however easily ensured for pulses close enough in time as compared to the polariton lifetime, which can always be enforced since the optical phase oscillates much faster than any other polariton timescale. To assure that the procedure is accurate and that Gaussian pulses excitation provide an adequate implementation of some initial states, we show in Fig. 3.4(c) the two-pulses simulation corresponding to the scenario of Fig. 3.3(c). Both the initial condition or its two-pulses excitation indeed provide the same result. The only difference is the transient from the state with one polarization only to that on the green circle, showing the sought initial state. This confirms that the initial states can be prepared by Gaussian pulses.

All the trajectories are thus theoretically available, however if some configurations cannot be reached directly in practice, because of constrains on the parameters like an excitation too far from the polaritons, they can be achieved more easily by working in a different polarization basis, *e.g.* in $\nwarrow\!\!\searrow/\nwarrow\!\!\searrow$.

One can find online a Wolfram demonstration applet to see and control the dynamics of polarization as function of the different parameters of the system, see ref. 6 page 131.

3.5 Experimental Realisation of full-Poincaré beams with Polaritons

In this Section, we first briefly describe the modifications brought to the experimental setup before coming to the experimental results. Two experimental case of Poincaré sphere spanning are presented, along with their theoretical fits.

3.5.1 Experimental Setup

To perform this experiment, we have chosen the same microcavity sample we used in the unpolarized Rabi oscillations experiment presented in the Chapter 2. The different physical parameters (energy of the branches, coupling strength, etc.) are thus the same. The detection of the fields remains based on the time-resolved digital holography technique. The substantial difference is the way to send and polarize the different femtosecond pulses. In this setup, they are initially linearly-polarized and passed through quarter wavelength plates to make them counter-circularly polarized. Like in the unpolarized experiment, the two pulses spread in energy to overlap both polariton branches, triggering the Rabi oscillations between excitons and photons.

3.5.2 Experimental results and fits

Two cases of interest have been realised experimentally. They are shown in Fig. 3.5 and 3.6. The polarization was detected in the different basis, namely (a) $\leftrightarrow/\updownarrow$, (b) $\nwarrow\!\!\searrow/\swarrow\!\!\nearrow$ and (c) $\circlearrowleft/\circlearrowright$. In each case, the light intensity $\langle a_p^\dagger a_p \rangle$ emitted from the cavity

is shown and the corresponding DOP S_p. For the latter, we only show the theoretical line, since it is obtained by combination of the two polarized fields, whose experimental data (black dots) are perfectly fitted by our model. These two cases were obtained by selecting particular initial conditions, namely with Rabi oscillations in both polarizations either in-phase or anti-phase. The time delay has been adjusted to obtain a peak-to-peak correspondance between the two circular polarizations ($\Delta\tau \approx 4\pi/\Omega_R$) in the case of Fig. 3.5, and peak-to-node correspondence ($\Delta\tau \approx 3\pi/\Omega_R$) in the case of Fig. 3.6. This results in two distinct behaviours. In the first case, the intensity is oscillating while the polarization is essentially fixed. For instance on the panel (b), one sees that the DOP shows quickly an essentially $\swarrow\!\!\nearrow$ polarized light, but with few variations of the DOP in the other basis. In the second case, the polarization tends also to a $\nwarrow\!\!\searrow$ state (panel b), but with strong oscillations of the DOP in the other basis, particularly in the circular one (panel (c)).

The light emitted from the cavity has been measured in all the polarization basis, with each time an excellent fit of the data. Two polarizations are actually needed by the theory to obtain the other ones, see Eqs. 3.11a. We have checked the consistency of the model and the observation by fitting polarizations in all bases and by their reconstruction from one basis only.

From the fit of the photonic fields intensity, the theory allows us the access to the full complex fields (photonic and excitonic), and we are thus able to reconstruct the polarization dynamics on the Bloch sphere (d) or through a $3D$ ($2D$ + time) representation (e). The last one, that displays the envelopes of the electric field, shows that various states of polarization are visited in succession in short time range (≈ 10 ps). This kind of light can be of a particular interest for the excitation of molecules only sensitive to certain polarizations, that are ultimately all provided in a single beam in the case of full Poincaré beams, providing an optimised exciting light, even for a gas of randomly oriented emitters. For instance, the case of Fig. 3.6(d) shows the spanning of a hemisphere of the Poincaré sphere. In Fig. 3.5(d) however, the polarization performs a fast transition between the initial and the final state.

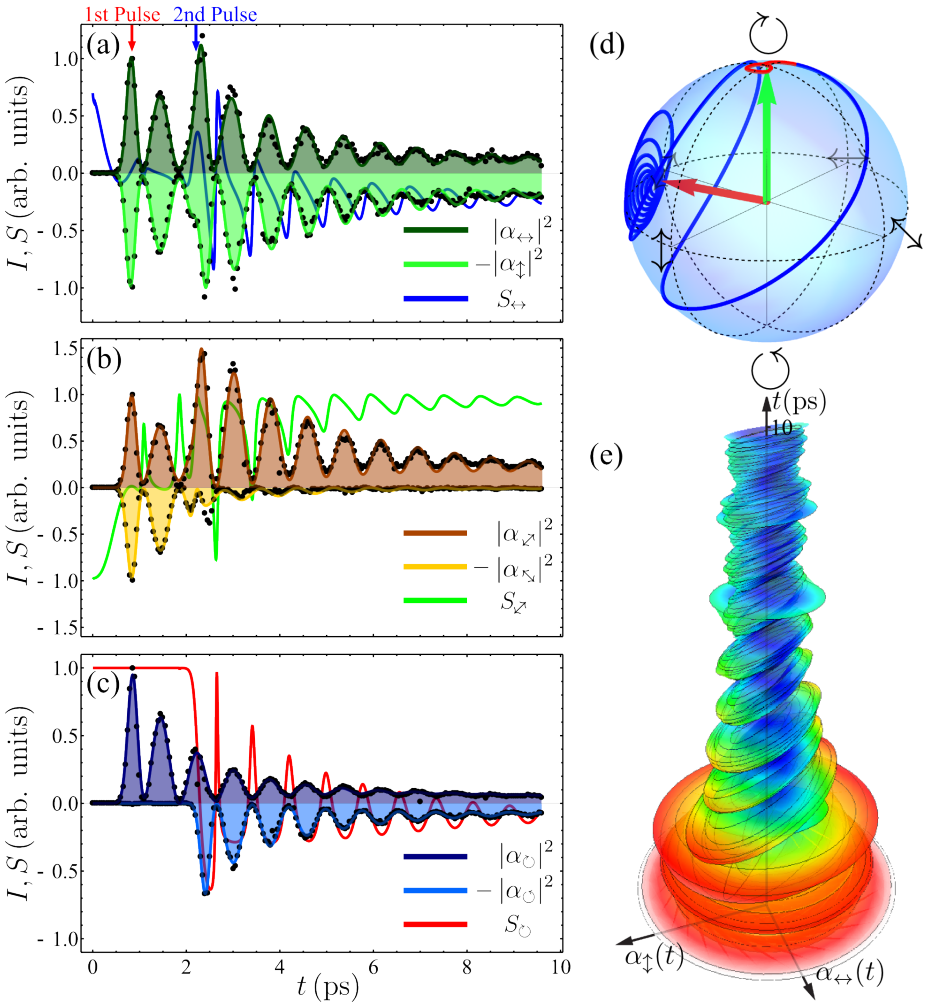

Figure 3.5: The Rabi oscillations from the two different pulses start with the same phase. The experimental data (a–c, black dots) is fitted by the theoretical model (solid lines), providing the amplitudes $I = |\alpha_{p,q}|^2$ and degrees of polarizations S_p. The dynamics of polarization is displayed on the Poincaré sphere (d), demonstrating the rapid transition to the linear polarization. (e) 2D + t representation of the polarization flow over a 10 ps time span: the surface represents the envelope of the electric field and the color (from red to blue) is scaled on the instantaneous field amplitude. Fitting parameters: $g = 4.02\ \text{ps}^{-1}$, $\gamma_a = 0.2\ \text{ps}^{-1}$, $\gamma_U = 0.43\ \text{ps}^{-1}$, $\omega_L^p = 829$ nm, $\sigma = 1/0.15\ \text{ps}^{-1}$, $\Delta\tau = 1.55$ ps .

3.5.3 Discussion

Polarization shaping is now a hot research topic and has already generated a vast literature. In parallel, the community of full-Poincaré beam has also produced many interesting results, developing its own set of techniques. Nonetheless, both of the two communities have to deal with their respective limitations. A conventional solid state laser generally emits light with a fixed polarization as is it the case for nano-antennas [64], for which the polarization is determined by their geometrical

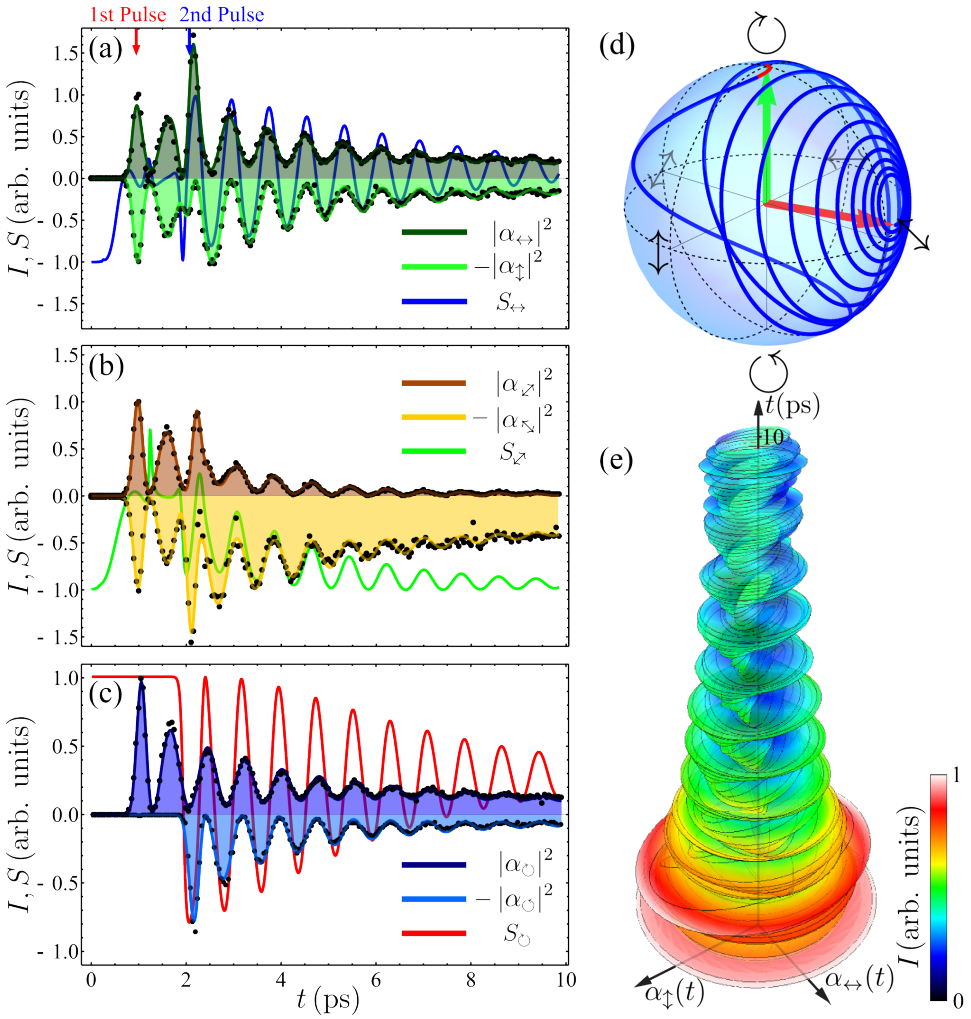

Figure 3.6: The Rabi oscillations from the two different pulses start with an opposite phase.(a) The dynamics of polarization is displayed on the Poincaré sphere (d), demonstrating the spanning of the full hemisphere of polarization. Fitting parameters: $g = 4.02\ \mathrm{ps}^{-1}$, $\gamma_a = 0.2\ \mathrm{ps}^{-1}$, $\gamma_U = 0.43\ \mathrm{ps}^{-1}$, $\omega_L^p = 829$ nm, $\sigma = 1/0.15\ \mathrm{ps}^{-1}$, $\Delta\tau = 1.13$ ps .

structure. The generation of an arbitrary state of polarization requires thus a bit of engineering. Polarization shaping techniques as the ones imagined and designed by Brixner [51, 54] are particularly demanding and require combinations of liquid crystals, spatial light modulators, interferometers, and computer resources working with special algorithms. A complex setup is thus involved, with its respective restrictions, such as the duration of the pulse in this case.

In our case, working with microcavity polaritons leads us to deal with the Rabi-oscillation phenomenon. Rabi oscillations are the building block on which our effect relies, and are also present in a great variety of platforms, occurring at different time scales or with different type of polarized fields. For the purpose

of our experiment, this was implemented in a semiconductor planar microcavity. These micrometer size devices are full self-integrated and do not rely on extrinsic processing of the signal unlike the other setups we have mentioned, reducing drastically the complexity of the platform. With this particular sample, the polarization dynamics occurs at the femtosecond time scale, similarly to the many pulse shaping systems. However, there are no intrinsic restrictions to perform it at other time scales. As we said, the effect relies on the Rabi oscillations and thus on the Rabi frequency, which allows the same dynamics to be realized at a different magnitude on another platform. For example, with today's technologies, this could be obtained from the attosecond level with plexcitons [65] to the millisecond with nanomechanical oscillators [31].

Also, since one cannot distinguish Rabi oscillations from the beating between two modes, our effect could also be implemented by using two independent filters and by tuning their lifetimes. But this would not be so straightforward since in practice, the two beams have to be sent into the filters and phase-locked onto the target. For this purpose, the polariton system offers many advantages. First, it provides the phase locking of two independent beams self-consistently. Secondly, in a polariton system, the Rabi frequency can be tuned by external means, like the use of an external electric or magnetic field or by changing the detuning between the bare excitons and photons. Finally, polariton provide a convenient way of tuning the lifetime imbalance by dephasing of one of the two branches. We have seen in with Eq. 3.19c that only the total decay rate of the upper polariton coherent fractions affects the loss of UP, no matters what is the responsible mechanism.

As we have mentioned before, the pulses we used in the experiment were essentially spatially homogeneous, see the space-time charts of Fig. 3.2, in order to focus on the time dynamics only. In the literature, one can find plenty of examples of spatially polarized beams with various profiles. As an example, we can mention the work done by Cardano *et al.* (2012) [66] where the generation of radial or azimuthal polarization field states by using Q-plate devices. For polaritons, such states could be implemented by sending the second pulse with a slight angle of incidence (*i.e.*, a Δ_{k_α}) with respect to the first one. One would thus obtain Rabi oscillating interference fringes. Each fringe could be made time-oscillating in polarization and with a phase offset with respect to each other giving rise to a flow of polarization waves with Rabi time period and settable space period, the whole drifting toward the fixed polarization state of the LP polariton. This shows how polaritons, in addition to the effect we have already demonstrated, could be use to generated more complicated states of polarization.

Since this work, many other studies and experiments have been done following similar directions. We can mention the interesting and very recent work of A. She and F. Capasso (2016) [67] for which the authors have developed a parallel architecture to generate time-varying states of polarization.

3.6 Conclusions

In this Chapter, we have seen how to generate and shape Poincaré beams by using the polariton system and its main properties, Rabi oscillations. The phase and time delay between the two non-interacting counter-polarized pulses is adjusted in order to produce a desired trajectory on the Poincaré sphere of polarization.

We first have seen in Section 3.2 the different kinds of enhanced polarized light available on the market. Most of the systems generating time-varying light beams are based on the work of T. Brixner, that opened and built an entire field in the manipulation of light polarization. Applications of this polarized light shaped at the scale of the femtosecond were demonstrated in the following years (post-2000s). In parallel, full Poincaré beams have been developed by a different community, with beams containing spatially all the states of polarization that could be mapped onto the Poincaré sphere. We then come in Section. 3.2.3 with our proposal based on polariton oscillations that brings together the interesting aspects of these two fields, with effect of generating a new kind of light: full-Poincaré beams in time.

In Section 3.3, we have presented the optical model we used to describe this new polarized light. The model is an extension of the one we used to describe and fit the unpolarized Rabi experiment of Chapter 2. In the present case, all of the fields intensities have been fitted independently since the effect relies on the superposition of non-interacting fields, since the two pulses we sent were orthogonally polarized. We have seen that by superimposing two polarized Rabi oscillating fields one could obtain a time-varying polarized light, see Fig. 3.1.

In Section 3.4, we have given the details of the polarization dynamics and how to tune the trajectories on the Poincaré sphere. We have seen that in the conservative case, without any decay or dephasing, the trajectories on the Poincaré sphere are given by circles that can be parametrised with Eqs. 3.20. The decay of polaritons has for interesting consequence to make the polarization swirl onto the sphere, until it reaches a final point. Various theoretical cases have been presented in Fig. 3.3. As it was done for the initial circle, we provided the parametrization of the final state on which the polarization converges on the sphere. This gave us access (theoretically) to a huge variety of trajectories, including the ones that cover the whole sphere, reaching *de facto* a full Poincaré beam in time. In order to also achieve it experimentally, we discuss in Section. 3.4.4 the way to prepare the initial states corresponding to the desired trajectories. The main experimental limitations arise from the laser excitation, for which some configurations could be hard to reach. However, changing the chosen basis of polarization could provide an issue.

The Section 3.5 is devoted to the experimental results and the realisation of Poincaré beams. We have presented two cases of interest (see Figs. 3.5 and 3.6). The first case shows the rapid drifting between two cardinal points of the sphere while the second one shows a half spanning of the Poincaré sphere, drifting slowly (in 10 ps) between two poles. The different dynamics have been reconstructed from the excellent fits of the experimental data. We have discussed on the possibility

to implement more complicated types of time-varying polarization by imparting a momentum on the second beam, that would create polarized Rabi oscillating interferences fringes, or by using beams with a non homogeneous polarization in space.

Chapter 4

Self-Interfering Wave Packets

Oh man, I shot Marvin in the face.
Vincent, Pulp Fiction.

Contents

In this Chapter, we study the propagation of non-interacting polariton wave packets. We show how two qualitatively different concepts of mass that arise from the peculiar polariton dispersion lead to a new type of particle-like object, shaped out of Gaussian initial states by the Rabi coupling. We also describe how such

Self-Interfering Packets can be obtained, and study their different representations notably with the use of the Wavelet Transform. This study gave rise to a publication in *Physical Review Letters* (see ref. 4 page 131).

4.1 Introduction

Field theories unify the concept of waves and particles. The nature of the wave function was a central topic of the pre-second-quantization era, and it found its apogee with the debate between Schrödinger and Heisenberg. Schrödinger developed the concept of coherent state to prove Heisenberg that his equation could describe particles with localised solutions (correspondence principle).

However, the connection between fields and particles is not exclusively quantum. With the discovery of solitons, it has been shown that classical fields could also provide a robust notion of particles. In this case, the cohesion of the particle is supported by the interactions, allowing a free propagation and surviving collisions with other solitons. For decades, these have been the major examples of how to define a particle using a classical field framework. Novelty came in 1979 [68] with Berry and Balázs (Balázs was an assistant of Schrödinger himself) who discovered similar behaviours in the non-interacting context : the Airy Beams. These solutions remained a mathematical curiosity for almost three decades. The field of non-trivial wave packets regained a huge interest with the experimental demonstration of the first truncated Airy beam, by Siviloglou *et al.* [69] in 2007 and many other results stemmed from it.

With the results presented in this Chapter, we add another member to the family of mechanisms that provide non-interacting fields with particle properties. We show how polaritons can support Self-Interfering Packets (SIP), resulting in the propagation of a train of sub-packets, much like the Airy beams, but without acceleration, fully normalizable and self-created out of a Gaussian initial state. The mechanism relies on the peculiar lower polariton dispersion, whose diffusive effective mass possesses regions in the k-space with both positive and negative values. Spreading in these regions induces self-interferences, reshaping the whole packet.

The Chapter is organised as follows. In Section 4.2 we discuss the contribution of Berry and Balàzs and how their new concept of particle described with classical fields was established. Even if this original work was published almost 40 years ago, it has found little echo in the optics community until the 2000s. We will mention the last research developments and applications. Later in this Section we see how this idea was generalised to other beam families.

In Section 4.3, we present the new concept of SIP. We start by showing the localisation properties of the polaritons in Section 4.3.1. Then, in Section 4.3.2 we dedicate an important discussion on the concept of the particles effective mass in a cavity, and how it has to be considered in a system with a nonlinear dispersion. In Section 4.3.3, we present the main result of this work, the generation of SIPs by spreading over the inflection point of the lower polariton dispersion. In Sec-

tion 4.3.4, we show how merging a SIP with Rabi oscillations leads to the ordering of a space-time honeycomb lattice. Possible ways to obtain analytical solutions for these results are then discussed in Section 4.3.5.

Section 4.4 is devoted to momentum-space representations of the SIP, bringing a clearer visualisation of the phenomenon. The first part, Section 4.4.2, treats of the Wavelet Transform, commonly used in signal processing but also useful when applied to a wave packet. We will compare it in Section. 4.4.2 with the more popular representation that is provided by the Wigner representation.

In the last Section 4.5, we discuss the realisation of a SIP in a realistic context, *i.e.* including radiative decay (see the Sec. 4.5.1) on the particles and physical mass parameters (Sec. 4.5.2). We also provide a way to generate SIP using potentials (Sec. 4.5.3).

Section 4.6 contains the main conclusions of this Chapter.

4.2 Non Trivial Wave Packets

In this section, we give an overview of some recently reported non trivial wave packets, starting with a first original result that challenged many accepted notions on the nature of fields: the Airy beam. We present the different properties that arise from these surprising solutions of the Schrödinger Equation. We see as well how the original idea of Berry and Balázs was then extended and generalised.

4.2.1 Airy Beams

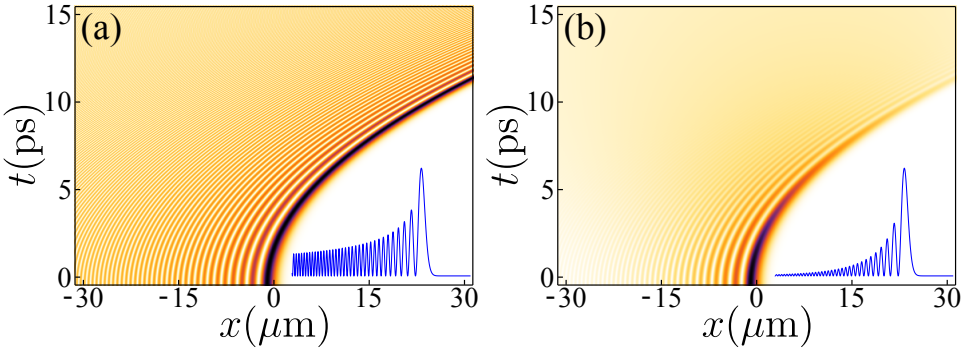

Figure 4.1: (a) Original Airy beam solution derived by Berry and Balàsz in 1979 [68]. (b) Truncated version proposed by Siviloglou *et at.* in 2007 [69]

In 1979, Berry and Balazs published [68] a remarkable paper that challenged the vision that the physicists had of the nature of the Schödinger wave packet. Considering the simple one dimensional Schrödinger equation without any potentials or exterior forces:

$$i\hbar\partial_t \psi(x,t) = -\frac{\hbar^2}{2m}\partial_x^2 \psi(x,t)\,, \tag{4.1}$$

and taking an Airy function as an initial condition $\psi(x,0) = \mathrm{Ai}(Bx/\hbar^{2/3})$, they found the following solution:

$$\psi(x,t) = \mathrm{Ai}\left(\frac{B}{\hbar^{2/3}}\left(x - \frac{B^3t^2}{4m^2}\right)\right) e^{\frac{iB^3t}{2m\hbar}\left(x - \frac{B^3t^2}{6m^2}\right)}, \tag{4.2}$$

where Ai(x,t) is the Airy function, solution of the equation $\partial_x^2 y - xy = 0$. It appears clearly that such a "Airy packet" propagates without spreading and accelerates to the right with the term $B^3t^2/2m^2$. This can be clearly observed in a space time density plot with curved trajectories of the different peaks, see Fig. 4.1(a). The acceleration is particularly shocking because of Ehrenfest theorem that connects observables from a quantum wavepackets to classical dynamics, and the latter is notoriously adamant since Galileo that in absence of an applied force, a system does not change its velocity. The absence of diffusion is less unexpected but this is the sort of quality for a Schrödinger wavepacket that Schrödinger was after before he resigned and turned to a potential to hold the packet together. Berry and Balázs' solution achieve this "particle"-like feat without the need of a potential. However, these two surprising properties emerge because of the non-physical character of the solution. Indeed, the function in Eq. 4.2 is non-square integrable. Ehrenfest theorem in particular does not apply.

For almost three decades, the Airy beam remained a mathematical curiosity and did not receive much attention. That is only in 2007 that the field was born again, when Siviloglou *et al.* [69] proposed a truncated version of the Airy beam by introducing an aperture function, *i.e* by multiplying the Airy function by a exponential term: $\mathrm{Ai}(x)e^{ax}$, with $a \ll 1$ typically. This resulted in the observation of a finite-lifetime (and finite-energy) optical Airy beam, as shown in Fig. 4.1(b). The peaks of the wave packet ("sub-packets") do indeed accelerate while also retaining their shape during propagation, but the truncated tail eventually destroys the structure, that thus exhists for a finite lifetime. Ehrenfest theorem becomes relevant again but is not violated: the total average does not accelerate, only sub-packets do appear to do so, inside a mother packet that moves according to Newtonian dynamics.

Still, these are fascinating objects, that, within the purely non-interacting, single-field Schrödinger equation, call us to reconsider our understanding of fields and particles. We can mention one of the first non-trivial applications of the physical Airy beams, namely, the realisation of optically mediated particle clearing using Airy sub-packet acceleration by Baumgartl *et al.* (2008) [70]. The accelerating property of the Airy beam was used experimentally to optically drag particles into the main intensity maximum, acting like a "particle snowblower". Also, Zhang *et al.* (2011)[71] have demonstrated the realisation of plasmonic Airy beams with dynamically controlled trajectories, opening the door to dynamic manipulations of nanoparticles on metal surfaces.

4.2.2 Other beams families

The concept of non-spreading and accelerating beam is not restricted to the Airy function nor to the Schrödinger Equation. Airy beams are also solutions of the paraxial wave equation, which is equivalent to the Schrödinger Equation. Zhang *et al.* (2012) [72] have demonstrated theoretically and experimentally the realisation of nonparaxial Mathieu and Weber accelerating beams, which are solutions of the Helmholtz Equation. The Airy beams is nothing more than a special case of Weber beams, themselves being a special case of Mathieu accelerated beams in the paraxial limit. Bessel beams are also known to be non-diffractive, non-spreading and also self-healing, *i.e.* they reform their shape after passing through an obstacle (*e.g.* a potential). A method has been proposed theoretically by I. D. Chremmos *et al.* (2012) [73] to generate Bessel-like optical beams with arbitrary trajectories in free space, that can be either non-accelerating or accelerating. The realisation of such Bessel beams have been demonstrated experimentally shortly after by Zhao *et al.* (2013) [74].

Accelerating beams can be implemented in various optical systems, such as photonic crystal slabs, honeycomb lattices, or various metamaterials [75]. There is an entire field of research about accelerated beams that has been developed in the past years

4.3 Self Interfering Polariton Wave Packets

In this Section, we present the formalism we used to describe non-interacting polariton wave packets. Various properties of the polaritons about their localisation, propagation or diffusion are presented, leading us to the concept of Self-Interfering Packet. We also explore momentum-space representations of the SIP and we discuss its possible observation in realistic conditions.

4.3.1 Localising a polaritonic field

The dynamics of the wavefunction $|\psi\rangle$ is ruled by the polariton propagator Π such that $|\psi(t)\rangle = \Pi(t-t_0)\,|\psi(t_0)\rangle$. In free space, it is diagonal in k space [76]:

$$\langle k'|\,\Pi(t)\,|k\rangle = \exp\left[-i\begin{pmatrix}\frac{\hbar k^2}{2m_C}+\Delta & \Omega_R \\ \Omega_R & \frac{\hbar k^2}{2m_X}\end{pmatrix}t\right]\delta(k-k') \tag{4.3}$$

where $m_{C,X}$ is the photon/exciton mass, Δ their detuning and Ω_R their Rabi coupling. Polaritons are maybe best formally defined as the states with a well defined momentum and, consequently, also energy. Note that in the absence of decay terms, the system is here perfectly conservative. The eigenstates of the propagator:

$$\Pi(t)\,\|k\rangle\rangle_\pm = \exp(-iE_\pm t)\,\|k\rangle\rangle_\pm\,, \tag{4.4}$$

define both the polariton dispersion:

$$E_\pm = \hbar k^2 m_+ + 2\Delta \mp k_\Omega^2 \,, \tag{4.5}$$

where the notation $\|\rangle\rangle_\pm$ stands for upper ("+") and lower ("−") polaritons. They also define the canonical polariton basis:

$$\|k\rangle\rangle_\pm \propto \begin{pmatrix} E_\pm(k) \\ 1 \end{pmatrix} |k\rangle \,, \tag{4.6}$$

where $m_\pm = (m_C \pm m_X)/(m_C m_X)$ are the reduced relative masses and $|k\rangle$ the plane wave of well defined momentum k. Another important quantity is the dressed polariton momentum:

$$k_\Omega^2 = \sqrt{\hbar^2 k^4 m_-^2 - 4\hbar k^2 \Delta m_- + 4(\Delta^2 + 4\Omega_R^2)} \,. \tag{4.7}$$

A general polariton state can thus be expressed as a linear combination:

$$\|\psi\rangle\rangle_\pm = \int_{-\infty}^{\infty} \phi_\pm(k) \, \|k\rangle\rangle_\pm \, dk \,, \tag{4.8}$$

with $\phi_\pm(k)$ the scalar-field (upper/lower) polariton wavefunction.

All the results in what follows come from the impossibility to evolve such a general polariton state in time with the complex rotation of free propagation as in Eq. (4.4), due to its two-component character. Except for a well-defined polariton state in k-space, i.e., a completely delocalized polariton in real space, the photon and exciton components of a polariton cannot be jointly defined according to a given wavepacket $\phi(k)$, e.g., a Gaussian packet, since one component gets modulated by the $E_\pm$ factor needed to maintain the particle on its branch. Gaussian packets for both the photon and the exciton result in populating both polariton branches. The general case obviously admixes the two types of polaritons:

$$|\psi\rangle = \sum_{\sigma=\pm} \int \phi_\sigma(k) \, \|k\rangle\rangle_\pm \, dk \,. \tag{4.9}$$

These results that impose strong constrains on a polariton wavepacket must be contrasted with the conventional picture one has of the polariton as a particle, which is that of states $\|k\rangle\rangle_\pm$ and is, in good approximation, recovered for large enough packets.

The composite structure of a polariton forbids its localisation in real-space, in the sense that both its photon and exciton components be simultaneously localized. If we choose $\phi(k)$ such that either $\psi_C(x, t = 0)$ or $\psi_X(x, t = 0)$ is $\delta(x)$, the other component is smeared out in a pointed wavefunction surrounding the singularity of the localized field, as shown in Fig. 4.2(a-b). Such constrains result in a rich phenomenology when involving a large enough set of momenta which, to the best of my knowledge, remained up to now safely hidden behind the simplicity of the equations.

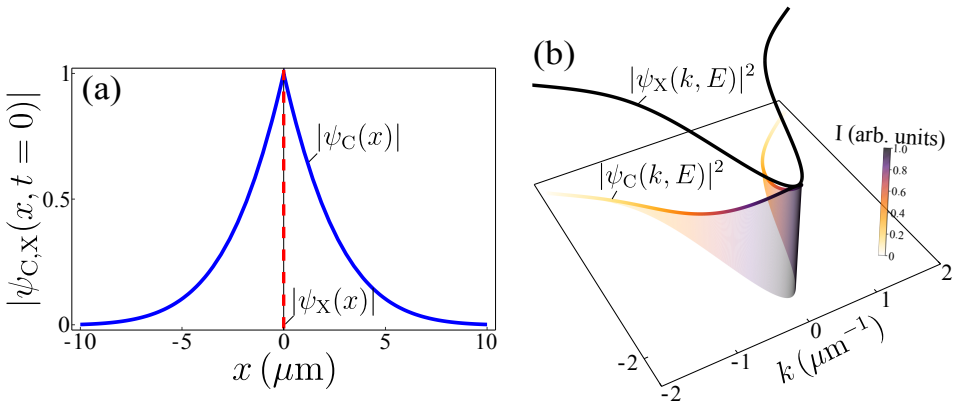

Figure 4.2: (a) Localising a polariton in space is possible for one of its component only (here in dashed red); the other field smears out to keep the particle on its branch. (b) Counterpart of (a) in energy-momentum space

4.3.2 Particles effective mass in a cavity

The concept of effective mass is a fundamental notion in solid state physics, that was initially introduced in band theory to describe the electrons motion, providing a useful semiclassical picture [77]. A notable property of the effective mass is that it can take negative values, which will be of a particular interest in the case of the polaritonic system.

Let us introduce it by considering the case of an electron in a crystal in the presence of an electric field F. The crystal's band can be locally approximated using a parabolic dispersion:

$$E(k) = E_0 + \frac{\hbar^2 k^2}{2m^*}, \tag{4.10}$$

where E_0 is a constant giving the band energy at the edge of the Brillouin zone and m^* is the effective mass, which is a constant here.

The electron's velocity can be connected to the energy gradient as follows:

$$v(k) = \frac{1}{\hbar}\partial_k E(k). \tag{4.11}$$

One can note that in the case of flat bands, this velocity goes to zero, as if we were dealing with extremely heavy classical objects. We can now obtain the Newton-like equation of motion :

$$\frac{dv(t)}{dt} = \frac{d}{dt}\frac{1}{\hbar}\partial_k E(k) = \frac{1}{\hbar}\frac{d^2E(k)}{dk^2}\frac{dk}{dt} = \frac{1}{\hbar^2}\frac{d^2E(k)}{dk^2}(-e)F, \tag{4.12}$$

where we have used the time derivative of the quasi-momentum of the electron in the crystal $d(\hbar k)/dt = -eF$, with e the elementary charge of the electron. This leads us to the well know expression for the effective mass:

$$m^* = \hbar^2(\partial_k^2 E)^{-1}. \tag{4.13}$$

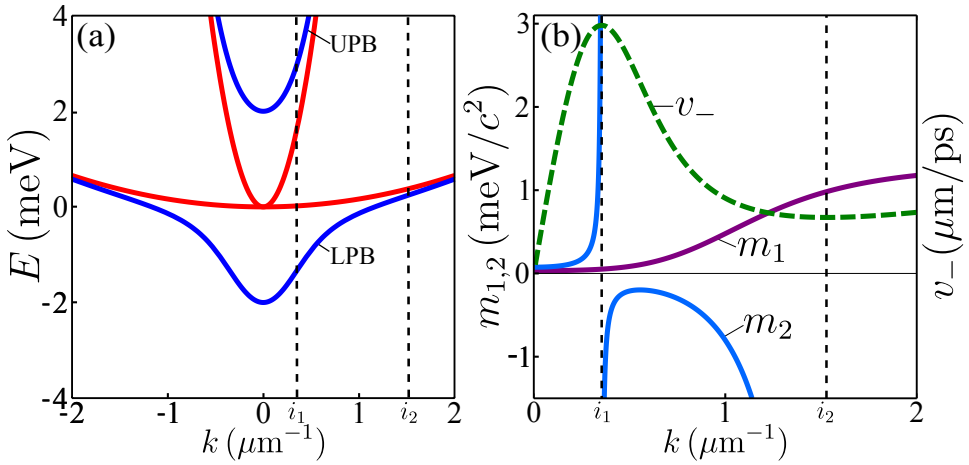

Figure 4.3: (a) Polariton dispersions. In red: the parabolic dispersion of the cavity photon, and the bare exciton. In blue: the polariton branches $E_\pm$. The vertical dashed lines at i_1 and i_2 mark the inflection points of the LPB. Parameters : $\Omega_R = 2$ meV, $m_C = 0.025$ meV ps^2 μm^{-2}, $m_X = 2$ meV ps^2 μm^{-2}. b) Effective masses for the LPB as a function of k: inertial mass m_1 (purple), diffusive mass m_2 (blue, negative when $i_1 < k < i_2$) and group velocity v_- (green).

One more time, we find from the previous expression that a flat band would induce an infinite effective mass that would cancel any motion of the electron. Another surprising result arises in the case of a dispersion with a negative curvature like the holes in semiconductors. Indeed, by reversing the dispersion's curvature, one obtains negative values for the effective mass m^*, which implies negative velocities when a positive force is applied on the system. An approximated expansion of the effective mass can also be generalized in the perturbation theory using the $k.p$ method [77]. The previous definition in Eq. 4.13 has been extensively used in the literature concerning polaritons to approximate their effective mass. However, most of it leaves aside the main feature that characterises polaritons, that they enjoy a non-parabolic dispersion relation, leading to different mass concepts for the propagation and the diffusion of the wave packet.

In 2005, Larson *et al.* [78] showed how these two concepts of mass emerge in the context of cavity QED, in which nonlinearity plays a key role. In the case of particles represented by a wave packet (possibly Gaussian), two mass parameters m_1 and m_2 are necessary to describe respectively propagation and diffusion. From the wave packet group velocity $v_g = \partial_k E(k)$, we define the *inertial mass* m_1 that determines the wave packet velocity from de Broglie's relation $p = \hbar k$ and the classical momentum $p = m v_g$ as:

$$m_1(E,k) = \hbar^2 k (\partial_k E)^{-1}. \tag{4.14}$$

The second mass parameter m_2, that we call the *diffusive mass*, is associated with the spreading of the wave packet. It depends on the branch's curvature, and reads:

$$m_2(E,k) = \hbar^2 (\partial_k^2 E)^{-1}. \tag{4.15}$$

For instance a Gaussian wave packet begotten from a non-parabolic dispersion but large enough in space to probe only parabolic portions of the dispersion in reciprocal space is essentially that expected from Schrödinger dynamics [79], it would diffuse according to the well known textbook expression:

$$\sigma_x(t) = \sqrt{\sigma_x^2(0) + \left(\frac{\hbar t}{2m_2\sigma_x(0)}\right)^2}, \tag{4.16}$$

where σ_x gives the Gaussian's standard deviation in real space, and where the mass parameter is the one depending on the branch's curvature m_2. It is important to note that in the last expression, the mass m_2 enters squared and thus its sign does not play a role in the wave packet diffusion. We will see in the following that the situation turns out to be more tricky when an important spread on the branch is considered.

The two masses m_1, m_2 and the packet velocity v_- are plotted in Fig. 4.3(b) for the LPB. Unlike parabolic dispersions, where they are equal, polariton dispersions yield different inertial and diffusive masses. We will see in details in the following how the k-dependent inertial mass m_1 imposes a maximum speed for the lower polaritons.

4.3.3 Dynamics of Polariton Wave Packets

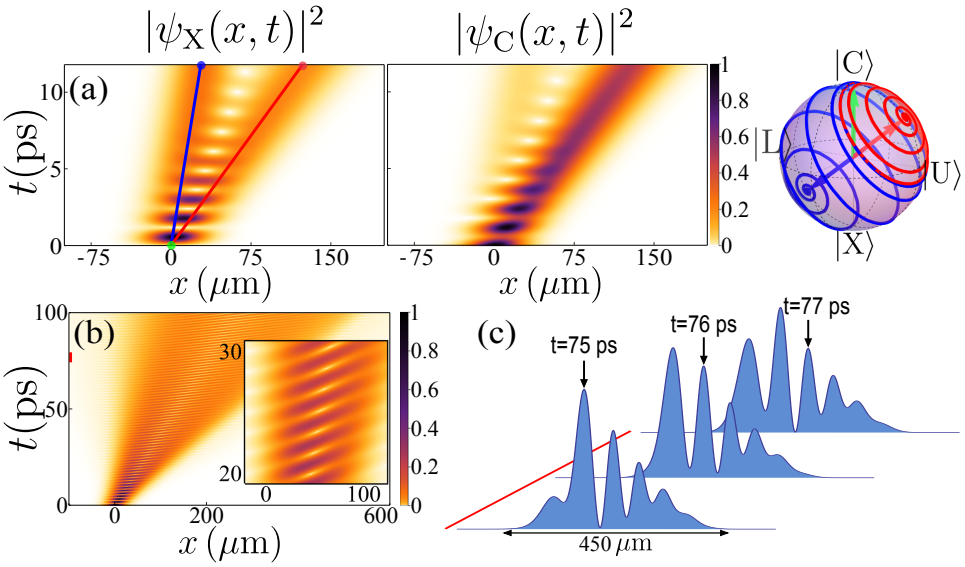

Figure 4.4: (a) Spacetime evolution of $|\psi_C(x,t)|^2$ and $|\psi_X(x,t)|^2$ with as an initial condition a photon of momentum $k_0 = 0.5\,/\mu$m. The Bloch Sphere shows the quantum state trajectories along the line of the density plot in (a). (b) Configuration with $\Delta = -\Omega_R$, preventing splitting of the beam and resulting in ultrafast, Rabi–powered, propagating sub-packets, as shown for three snapshots of time in (c).

In the previous Section, we have seen how the different effective masses should be treated for polariton dispersions. For the propagation of polaritons wave packets, one has to consider the inertial mass m_1. The group velocity $v_\pm = \partial_k E_\pm(k)$ can then be directly derived from the dispersion relation. This means a different group velocity at $k \neq 0$ for the upper and lower polaritons, the upper being usually faster due to its smaller effective mass. Thus, exciting the system with a non-eigenstate, *i.e.* producing Rabi oscillations between ψ_C and ψ_X, and with an imparted momentum $k_0 \neq 0$, will lead to the splitting in space of the upper and lower polariton components of the bare states. This is illustrated in Fig. 4.4(a) where the system is excited with a Gaussian packet in the photonic component at $k_0 = 0.5\ \mu m^{-1}$. At early times, we see Rabi oscillations between the two fields, but then, as time passes, in both components, the beam tends to split in two parts without Rabi-oscillating any more. The nature of the two resulting beams can be identified by looking at their respective quantum state. To do so, we have computed and displayed the quantum state following two paths along each beam, as represented in blue and red on Fig. 4.4(a). Both paths start at the same point (green dot). On the Bloch Sphere, the initial state is represented by a green arrow pointing at the $|C\rangle$ state. Then the states of the two beams converge to orthogonal points on the meridian of the sphere. They correspond to an upper and lower polariton state. They are not reaching exactly the cardinal points $|U\rangle$ and $|L\rangle$, the sphere's orientation being calculated at resonance. Here we observe an important properties of polaritons : Rabi oscillations can be viewed as a space-time interference between two polariton fields (upper and lower), which depends directly on their spatial overlap.

This allows one to obtain more complex Rabi oscillation patterns in space and time. For instance, considering an energy detuning between the bare states leads to intricate patterns. We show in Fig. 4.4(b-c) the effect of a detuning $\Delta = -\Omega_R$. This bends the Rabi oscillations in space and time and results in the propagation of ultrafast subpackets, moving inside a mother packet, as shown in (b) and for three time snapshots in (e). The subpackets, continuously formed in the tail of the mother packet, propagate inside it one order of magnitude faster, powered by Rabi oscillations, before dying in the head. Each sub-peak acquires properties of an identifiable object, traceable in time. A video of the full wave packet dynamics (of Fig. 4.4(b-c)) is available on-line in the supplementary section of ref. [80].

Let us now focus on the lower polariton's properties. We have already seen (Fig. 4.3) that its velocity v_- features a local maximum. It reads:

$$v_- = \frac{k}{2m_+} - \frac{\frac{\Delta}{k} - \frac{k}{2m_-}}{\sqrt{1 - \frac{4m_-\Delta}{k^2} + \frac{4m_-^2(4\Omega_R^2+\Delta^2)}{k^4}}}, \tag{4.17}$$

which is shown in Fig. 4.5 (blue line). The local maximum is obtained at the first inflection point of the dispersion, $k = i_1$. Increasing the momentum makes the particle heavier and actually reduces its speed. A local minimum is attained at the second inflection point, $k = i_2$, where the polaritons also propagate without diffusion but now with a lower speed. At larger k, Eq. (4.17) becomes linear and

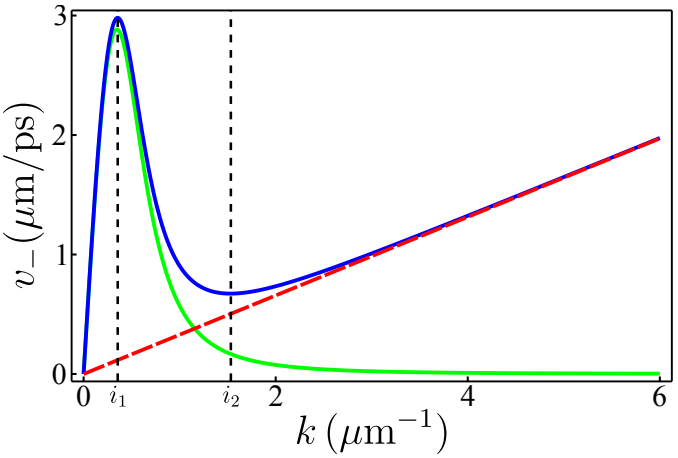

Figure 4.5: Speed of the lower polariton as a function of its imparted momentum, for a non-detuned system. The blue curve shows the group velocity v_- with $\Delta = 0$. There is a maximum and larger momenta result in slower particles. Local maxima are given by the inflection points i_1 and i_2. At large enough k, the polariton becomes exciton-like and suffers no such restriction. The red-dashed line is the group velocity of the bare excitons. In green is plotted the group velocity v_- for $\Delta = 0$ and $m_X \to \infty$. If the exciton mass is infinite, polaritons have an absolute maximum velocity.

tends to the speed of the bare exciton, as indeed for $k \gg 0$, $v_-(k) \to k/m_X$, cf. Fig. 4.5 in dashed red for a non-detuned system. If there is no second inflection point (for an infinitely heavy exciton mass), there is an absolute maximum speed for the polaritons since the bare exciton group velocity vanishes (green curve).

The LPB is also particularly interesting because the diffusive mass m_2 diverges at its two inflection points and becomes negative between them. According to the diffusion law for a Gaussian wave packet (see Eq. 4.16), if the mass parameters m_2 tends to infinity, then the diffusion is cancelled and the size of the packet remains $\sigma_x(0)$. This phenomenology can be seen in Fig. 4.6 (a-b), where by exciting the LPB, we propagate a Gaussian wave packet with an initial size of $\sigma_x = 20\,\mu\mathrm{m}$. As we propagate an eigenstate of the system, there is no longer Rabi oscillations between the photonic and excitonic fields. On the panel (a), we see that at resonant excitation ($k_0 = 0$) the Gaussian wave packet diffuses in a usual way. But exciting the branch on its first inflexion point ($k_0 = i_1\ \mu\mathrm{m}^{-1}$) leads to a perfect cancellation of the diffusion (b), the size of the packet σ_x remaining the same at any time and thus presenting a solitonic-like behaviours.

Exciting the LPB at its first inflection point has already been used to generate bright solitons and soliton trains, notably by the groups of D. Skryabin and M. S. Skolnick, see the main references from Egorov *et al.* (2009) [14], Sich *et al.* (2012) [15] and Sich *et al.* (2014) [16]. In all of these experiments, polariton-polariton interactions are present due to the high pumping applied. The mechanism of solitons generation is based on the interplay between the negative effective mass and the repulsive interactions. We remind that in this Chapter we do not include interactions between the particles, the nonlinearity of the polariton branches arises

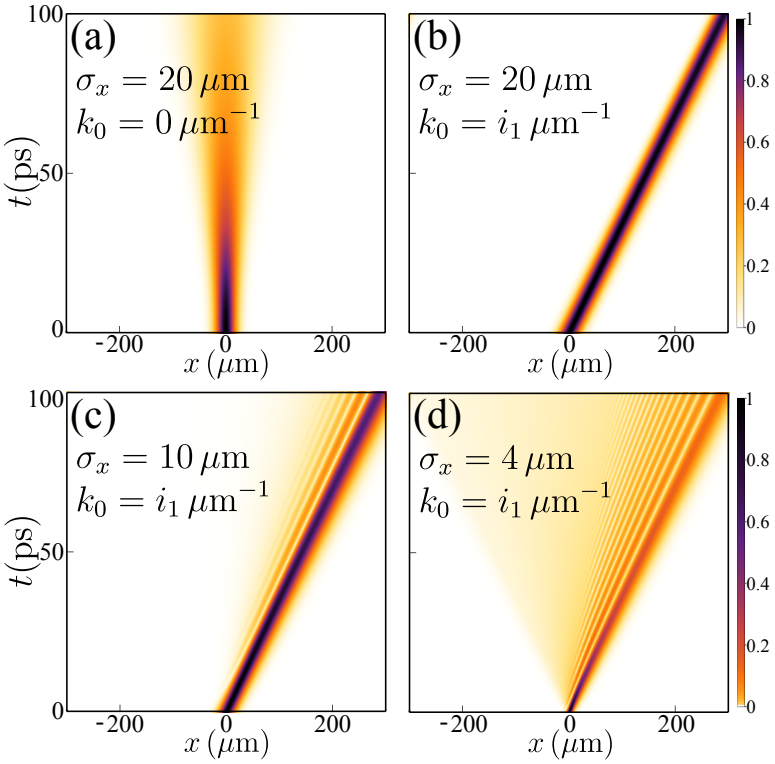

Figure 4.6: Propagation of lower polariton packets for various momenta and sizes. (a) Regular diffusion of the wave packet, the LPB is excited resonantly with a small spread ($\sigma_k = 1/20\ \mu\mathrm{m}^{-1}$). (b) Exciting the LPB at first inflection point i_1 induces an infinite diffusive mass of the wave packet and cancels its diffusion. (c-d) The size of the packet is decreased to reach the regime of self-interferences ($\sigma_k = 1/10\ \mu\mathrm{m}^{-1}$ and $\sigma_k = 1/4\ \mu\mathrm{m}^{-1}$), that occurs when the spread on the branch straggles over the divergence

only from the Rabi coupling between the photonic and the excitonic fields. In these studies, the role of the high effective mass, that could possibly helps the soliton generation, was not fully estimated.

So far, the interesting phenomenology we have discussed illustrates isolated features of polariton propagation. A new physical picture emerges when combining several aspects within the same wave function, leading to the concept of SIP. This new kind of wave packet appears when one increases the staggering on the dispersion on the momentum-space, that is, reducing the packet's size in the real-space. The sizes of a Gaussian wave packet in both real and momentum space are simply linked by their inverse:

$$\sigma_x(0) = 1/\sigma_k(0)\,. \tag{4.18}$$

New features appear when the spread in k is large enough to probe polaritonic deviation from the parabolic dispersion. In the previous case, the sign of m_2 did not impact the diffusion, since it entered squared in Eq. 4.16, which remains true for $i_1 < k < i_2$. It plays here an explicit role. If the wave function's spread straddles

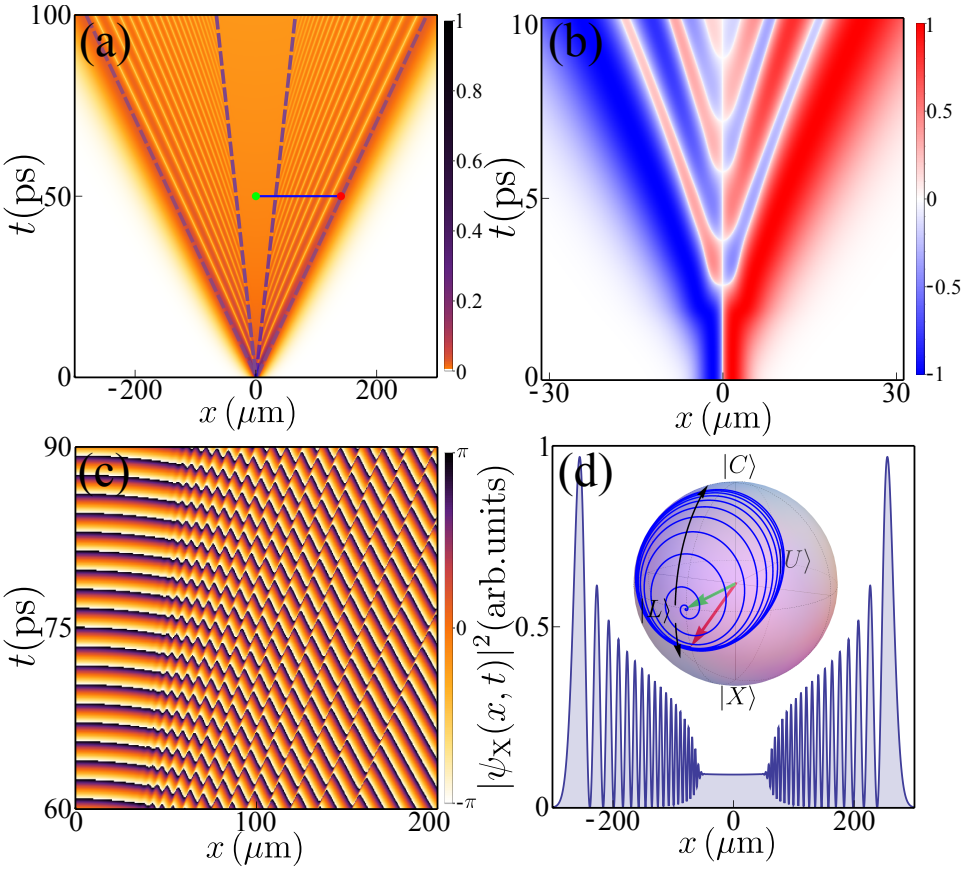

Figure 4.7: a) Propagation of a Self Interfering Packet, produced by exciting the LPB with a narrow Gaussian packet $\sigma_x = 2$ µm. The blue dashed lines show the cones that limit the diffusion, obtained from the inflection points (see. Eq. 4.19). (b) Corresponding probability current j, calculated at early times. (c) Phase profile computed from a selected region in space-time. (d) SIP intensity at $t = 50$ ps with a Bloch Sphere displaying the quantum state computed from a selected path (from green to red in (a)).

over the divergence, self-interferences appear between the harmonics of the packet subject to the positive mass and others to the negative mass. In Fig. 4.6(c-d) one can see how the wave function is reshaped when the initial size of the packet $\sigma_x(0)$ is decreased in space down to 10 µm and 4 µm, and thus extended over the first inflection point of the LPB in the $k-$space. The part of the packet that goes above the divergence is rejected back and interferes with the rest, resulting in ripples. The whole wave packet still propagates forward since the group velocity remains positive. We point out that in the different density plots shown here, the color gradient is not necessarily kept linear. Indeed, we have to deal with sharp functions as initial conditions, that cause a fast diffusion, the interesting physics occurring during the diffusion process. The full picture of the SIP can be obtained by reducing even more the size of the initial wave packet. Exciting this time resonantly ($k_0 = 0$) with a packet whose size is reduced to $\sigma_x(0) = 2$ µm provides enough spread in both

positive and negative ks on the LPB to see the total area covered by the interferences. The wave function evolution is plotted in Fig. 4.7(a). While for a parabolic dispersion, squeezing the packet in space merely causes a faster diffusion, in the polariton case however, there is a critical diffusion beyond which the packet stops expanding and folds back onto itself. This happens when the wave function encounters the inflection point of the LPB, that acts like a "mass wall" against which the packet bounces back. In the case of relatively small excitons mass, the second inflection point i_2 of the branch becomes accessible and thus, spreading over this point induces another reflection of the wave function, shielding from the self-interferences the core of the mother packet. The two diffusion cones of the wave function due to the inflection points of the LPB are materialized by blue dashed lines on the space time chart Fig. 4.7(a). They correspond to a propagation with the wave vector related to the inflection points, and their expression is thus simply given by:

$$w_{1,2}(t) = \frac{t}{k(i_{1,2})}\,, \tag{4.19}$$

where the values of the inflection points $k(i_{1,2})$ are obtained by solving $\partial_k E_- = 0$, which is complex polynomial equation with no closed-form solutions, but the solutions can be easily obtained numerically.

This result is the first reported case of self-interferences occurring for a single wave packet and without applying any external forces or potentials. From a conceptual point of view, it shows the coexistence of masses of opposite signs within the same packet. The mother packet $|\psi\rangle$ fragments itself into two trains of daughter shape-preserving subpackets which travel in opposite directions. In average, the momentum carried by the mother packet is null $\langle\psi|p|\psi\rangle = 0$ but self-shaping the wave function redistributes it to its subpackets as a series of non-zero momenta. All of these different sub-peaks can be identified by following their quantum state on the Bloch sphere, as we did in Chapter 2. As shown in Fig. 4.7(d), they lie onto the meridian between $|\mathrm{L}\rangle$ and $|\mathrm{X}\rangle$. The quantum state is computed from a path starting from the center of the packet to the edge (see Fig. 4.7(a) from green to red at $t = 50$ ps). One can thus see the SIP as a train of polariton packets "emitted" by the area shielded from the self-interference at the rate of Rabi oscillations, and that maintain their individuality as they propagate inside the mother packet. We will come back on this point in the next Section, by deriving at analytical solutions.

It is also interesting to have a look at the SIP's phase profile $\phi(x,t)$ of the total wave function $\psi(x,t) = |\psi(x,t)|e^{i\phi(x,t)}$, plotted in Fig. 4.7(c). The successive peaks exhibit a maximum phase shift of π. Baring the fact that they do not involve self-interactions to account for their cohesion and other properties making them particles lookalike, these propagating subpackets behave in many respects as soliton-like objects. This makes our analogy with Airy beams now conspicuous.

More insights into the nature of the SIP can be obtained by looking at the probability current :

$$j = \frac{i\hbar}{2m_1}\left(\psi^*\partial_x\psi - \psi\partial_x\psi^*\right). \tag{4.20}$$

It is shown in Fig. 4.7(b) for the SIP at early times. The red and the blue colors represent the probability flux moving rightward and leftward, respectively. One can see clearly how the wave function alternates rightward and leftward net flows. In the case of a standard diffusion of a Gaussian wave packet, this plot would have been fully red on the right and fully blue on the left.

4.3.4 Space-Time Crystal

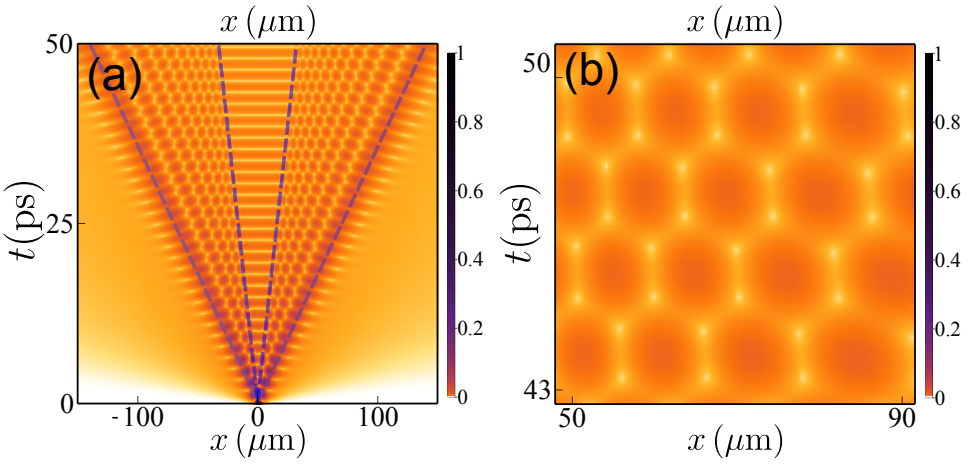

Figure 4.8: (a) Spacetime honeycomb lattice when combining the SIP with Rabi oscillations by starting with a photon as an initial condition. The blue dashed lines correspond to the diffusion cone into which the lower polariton field diffuses. (b) Zoom of the hexagonal lattice.

We have seen before how one can generate a SIP by taking advantage of the nonlinear dispersion relation of the LPB. However in most of the current experiments, the LPB is not excited directly through an eigenstate of the system but with a bare state, for instance the photonic field by shinning a laser onto the microcavity. This leads to all of the Rabi phenomenology we have described in the previous Chapters. Let us now combine the different patterns emerging from the SIP mechanism and from the Rabi dynamics. We consider, as we did before, the generation a SIP with a narrow Gaussian wave packet ($\sigma_x = 2$ μm) to excite the photonic field ψ_C, instead of exciting directly the LPB. The result is shown in Fig. 4.8. The combination of the SIP and Rabi features gives an amazing pattern in space and time, with domains. We have reported with blue dashed lines the limits of the diffusion cones induced by the self-interferences of the lower field. In Fig. 4.8(a) we see that in the central region, protected from the self-interferences by the second mass wall, normal Rabi oscillations appear, showing interferences between the upper and the lower fields. However, in the outer regions, the packet undergoes a very fast diffusion without exhibiting any interferences or Rabi oscillations. This part corresponds solely to the upper field, the lower field being reflected before by the first mass wall and thus cannot propagate in these regions of space. The upper field does not suffer from such a restriction and diffuses everywhere equally. The

most interesting phenomenology takes place in the SIP area, sitting between the two mass walls, the interplay of Rabi oscillations and self-interferences produces an hexagonal lattice. A zoom in this region is plotted on Fig. 4.8(b). Such a structure is known to arise from the interference of three beams [81], and indeed in our case the hexagonal pattern comes from the interference of two effective lower fields (actually one lower field, but self interfering) and one upper field. This striking structure is, again, sculpted self-consistently out of a unique photon field with a simple Gaussian shaped by the dynamics of coupled non-interacting fields. Here, instead of the emergence of propagating particles, a spacetime crystal is formed with the manifest ordering of the previously freely propagating train of polaritons.

Let us discuss in more details how the different fields are interfering and in which areas. The photonic field ψ_C is not an eigenstate and exciting the cavity creates Rabi oscillations, that can be seen as the result of a beating between the two eigenstates: the lower ψ_+ and the upper ψ_- polaritons. This provides two fields. As mentioned, Rabi oscillations only take place if there is a spatial overlap between these two polariton fields. This is what happen in the central area. When the SIP regime is reached by exciting a large part of the dispersion, straddling over an inflection point of the branch, the field interferes with itself, providing two additional effective fields in the same spatial area. The diffusion cone thus contains $\psi_-(0<k<i_1)$ and $\psi_-(i_1<k<i_2)$ (or symmetrically on the negative k). If the second inflection point is reached, it also contains $\psi_-(k>i_2)$. However the field ψ_+ does not suffer from any restriction in its diffusion, and thus covers most of the space time domain. In Fig. 4.9(a) we have delimited with green arrows the three fields present within the diffusion cone on the right side, and in blue for their negative k counterpart on the left side. So by exciting one single field ψ_C, polaritonic systems allow us to create in some regions of space a superposition of three effective fields that interferes to order a time crystal structure.

The same hexagonal structure can be as well constructed from three independent fields. By resonant excitation at $k_0 = 0$ we have created a lower and an upper field (exhibiting Rabi oscillations due to their spatial overlap), on which is sent another lower polariton beam imparted with a momentum $k > i_1$, that gives rise to an hexagonal lattice in the common interference area. The result is plotted in Fig. 4.9(b). All this phenomenology follows self-consistently from a single photon beam in the SIP case. In the next Section, we will see how the SIP and the interferences can be regarded in different momentum-space representations.

4.3.5 SIP analytical solution

The theoretical description of a SIP is, in principle, simple. It consists in a set of two coupled-Schrödinger Equations in the linear regime, and without added potentials terms. The Schrödinger Equation is possibly the most studied one in physics, but this does not guarantee that it has been fully explored and that all the solutions are known. We have mentioned before the example of the Airy beam, discovered only in 1979.

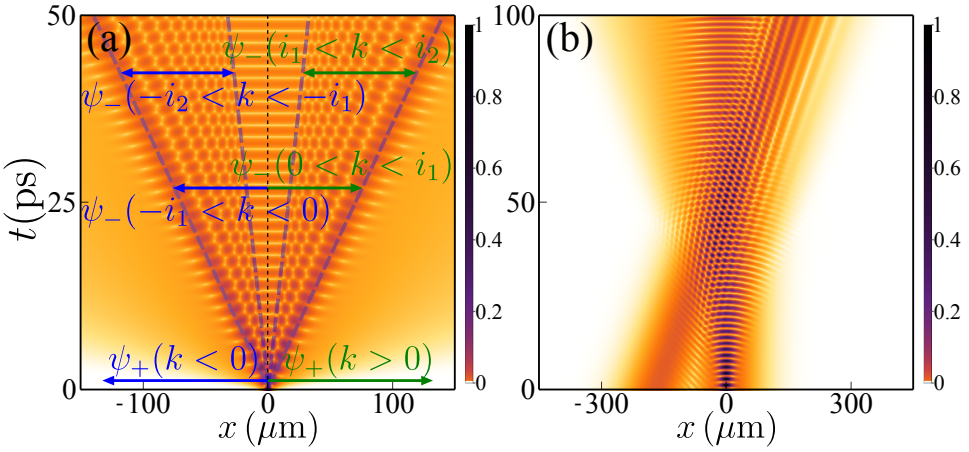

Figure 4.9: (a) Propagation of a SIP with Rabi oscillations, exhibiting a spacetime hexagonal lattice. Specific areas are identified to explain the effect as the interference of three beams. The different arrows indicate which components of the different fields (ψ_+ and ψ_-) diffuse within these areas. The lattice is formed by two LP fields and one UP field. Rabi oscillations or simple diffusions are obtained in areas with only two and one field, respectively. (b) An hexagonal lattice in space and time can be also produced by making interfering three independent beams: exciting resonantly a lower polariton and an upper polariton (providing Rabi oscillations) produces the same pattern when overlaping with another lower polariton field imparted with a momentum (here with $k_0 > i_1$).

We will attempt here to look for an analytical expression of the SIP. Let us start with the complete expression of the polariton propagator :

$$\langle k'|\Pi|k\rangle = \begin{pmatrix} e^{\frac{-ik^2 m_+ t}{4}}\left(\cos(\frac{k_\Omega^2 t}{4}) + i\frac{k^2}{k_\Omega^2}m_-\sin(\frac{k_\Omega^2 t}{4})\right) & -\frac{i4\Omega_R}{k_\Omega^2}\exp(\frac{-ik^2 m_+ t}{4})\sin(\frac{k_\omega^2 t}{4}) \\ -\frac{i4\Omega_R}{k_\Omega^2}\exp(\frac{-ik^2 m_+ t}{4})\sin(\frac{k_\omega^2 t}{4}) & e^{\frac{-ik^2 m_+ t}{4}}\left(\cos(\frac{k_\Omega^2 t}{4}) - i\frac{k^2}{k_\Omega^2}m_-\sin(\frac{k_\Omega^2 t}{4})\right) \end{pmatrix}\delta(k-k'), \tag{4.21}$$

where we remind the important dressed momentum variable k_Ω :

$$k_\Omega \equiv \sqrt[4]{k^4 m_-^2 + 16 m_+^2 \Omega_R^2}, \tag{4.22}$$

that depends explicitly on k. We also have introduced the reduced masses $m_\pm = (m_C \pm m_X)/(m_C m_X)$ and set $\hbar = 1$ in order to lighten the expressions.

Following the previous discussion on the localisation of polaritons, we will start with the case of a lower polariton prepared so that the photonic component is perfectly localized at $t = 0$. Since we focus only on a simple SIP picture, we can restrict the LPB to only have a single inflection point by flattening the exciton dispersion. To do so, we have to set $m_X \to \infty$. The SIP profile we are thus expecting is a wave packet entirely affected by the self-interferences, since no second "mass wall" can shield the core of the packet any more. From the previous Equations, we

find the fields expression in the k-space:

$$\psi_C(k,t) = \exp\left(-i\frac{k^2-k_\Omega^2}{4m_C}t\right)\frac{k_\Omega^2-k^2}{4\Omega_R m_C}, \tag{4.23a}$$

$$\psi_X(k,t) = \exp\left(-i\frac{k^2-k_\Omega^2}{4m_C}t\right). \tag{4.23b}$$

The case of a perfectly localized exciton as the initial condition (i.e., in the photon vacuum rather than the field needed to provide a lower polariton), i.e., $\psi_-(x,t=0)=(\delta(x),0)^T$, is given directly by the columns of Eq. 4.21:

$$\psi_C(k,t) = \exp\left(-\frac{ik^2t}{4m_C}\right)\left[\cos\left(\frac{k_\Omega^2 t}{4m_C}\right)-i\left(\frac{k}{k_\Omega}\right)^2\sin\left(\frac{k_\Omega^2 t}{4m_C}\right)\right], \tag{4.24a}$$

$$\psi_X(k,t) = \exp\left(-\frac{ik^2t}{4m_C}\right)(-i\Omega_R t)\,\mathrm{sinc}\left(\frac{k_\Omega^2 t}{4m_C}\right). \tag{4.24b}$$

In the same way, we are expecting an hexagonal lattice covering entirely the interferences zone, with a fast diffusion of an upper polariton outside. The corresponding field intensities for Eqs. 4.23a and 4.24a are easily obtained in the real space by Numerical Fourier Transform and plotted in Fig. 4.10. Finding a closed-form solu-

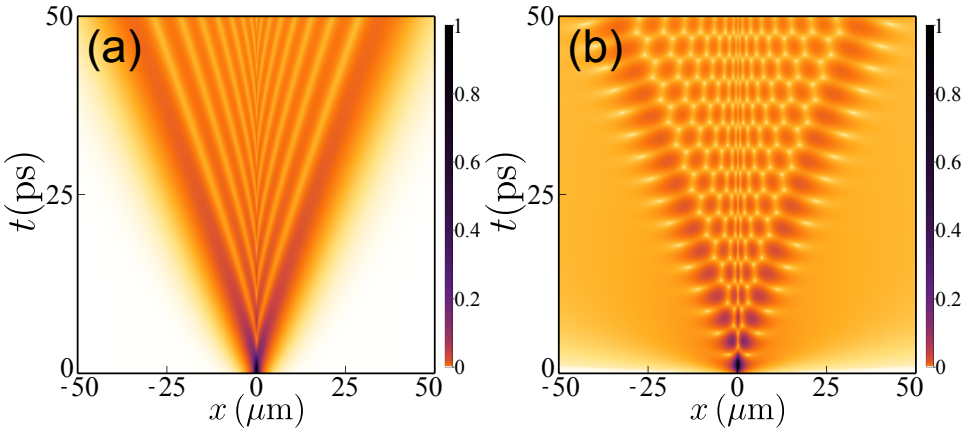

Figure 4.10: Field intensities of a lower field $|\psi_-|^2$ (a) and a photonic field $|\psi_C|^2$ (b) whose photonic components are perfectly localised at $t=0$. The exciton mass has been set to $m_X \to \infty$ in order to flatten the LPB at high ks, shifting the second inflection point to ∞. The core of the packets are thus totally affected by the self-interferences process.

tion of the previous wave functions in real space reveals to be a hard task, mainly because of the term $\exp(k_\Omega^2-k^2)$. Its representation in real space captures the (lower) polaritonic self-interferences effect. However, I could not obtain a closed form for this Fourier Transform. Nonetheless, the term $k_\Omega^2-k^2$ can be well approximated by a Voigt distribution, since it combines both exponential and fat-tail types of decay. Since the fat-tail could be expected to play a dominant role qualitatively,

we assume simply a Lorentzian distribution $f(k) = 4\Omega_R m_C/\left(1+\frac{k^2}{4\Omega_R m_C}\right)$. Let us apply this approximation to Eq. 4.23a, it reads :

$$\psi_X(k,t) \simeq \frac{-\exp\left(\frac{-it\Omega_R}{1+k^2/(4m_C\Omega_R)}\right)}{1+k^2/(4m_C\Omega_R)}. \tag{4.25}$$

which Fourier Transform can be obtained by a series expansion of the exponential, providing the real-space dynamics of the SIP:

$$\psi_X(x,t) \simeq \sum_{n=0}^{\infty} \frac{-4\sqrt{\pi}(m_C\Omega_R)^{\frac{3+2n}{4}}(it\Omega_R)^n|x|^{\frac{1}{2}+n}K_\alpha(2\sqrt{\Omega_R m_C}|x|)}{n!^2}, \tag{4.26}$$

where $K_\alpha(z)$ are the modified Bessel functions (solutions of th equation $z^2y'' + zy' - (z^2+n^2)y = 0$) and with $\alpha = n+1/2$. The propagation of the wave packet calculated with the Numerical Fourier Transform (a) and the one obtained with the analytical formula in Eq. 4.26(b) are compared in Fig. 4.11. The qualitative agreement looks good, only the size of the propagation cone differs slightly, due to the difference between the Lorentzian distribution and the real one. This approximation is good enough to describe the nature of the SIP. The convergence of the series in Eq. 4.26 is obtained for a number of terms in the sum that increases linearly with time t. The SIP is a phenomenon of many interferences, each new peak arises from a next order in the interferences as it requires more terms to ensure the convergence of the series. At the center of the wave packet ($x = 0$), the previous expression can be reduced to a simple form :

$$\psi_X(x=0,t) \simeq -2\pi\sqrt{\Omega_R m_C}\, e^{\frac{it\Omega_R}{2}} J_0\left(\frac{t\Omega_R}{2}\right), \tag{4.27}$$

where $J_n(z)$ is the Bessel function of the first kind. We expect a better agreement at $x = 0$, since the principal approximation we made mainly affects the extent for the envelope of the momentum. We actually find a perfect agreement between Eq. 4.27 and the exact numerical result, as shown in Fig. 4.11(c). The Eq. 4.27 confirms that the successive peaks appear with the Rabi frequency Ω_R. The photon mass m_C (we remind that we assumed here an infinite exciton mass) acts only on the intensity.

In the same way, one can obtain the corresponding series for the photonic field :

$$\psi_C(x,t) \simeq \sum_{n=0}^{\infty} \frac{4\sqrt{\pi}(m_C\Omega_R)^{\frac{2n+1}{4}}(it\Omega_R)^n|x|^{n-\frac{1}{2}}K_\beta(2\sqrt{\Omega_R m_C}|x|)}{n!\Gamma(n)}, \tag{4.28}$$

with $\beta = n-1/2$, showing the sort of complexity that describes both structures and how they are tightly related. The corresponding Series of Eqs. 4.24a and 4.24a can also be obtained, involving Hypergeometric functions, that are too cumbersome and do not bring more informations to be written here.

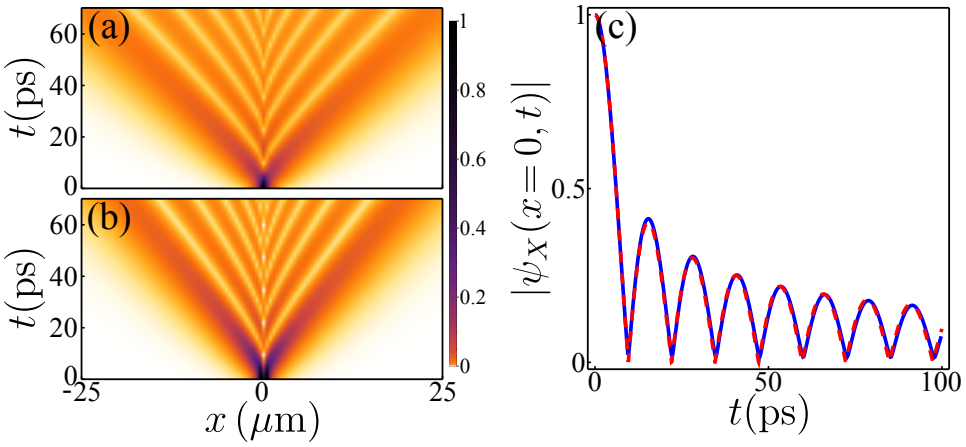

Figure 4.11: (a,b) $|\psi_X(x,t)|^2$ calculated from the exact result Eq. (4.23a) and the approximated one, Eq. (4.26). (c) Normalized intensity at the center of the wavepacket ($x = 0$): exact result through the Fourier Transform of Eq. (4.23a) (blue line) and the analytical expression Eq. (4.27) (red dashed line). The approximation appears to be exact at $x = 0$.

4.4 Momentum-Space representation

In this section, I will discuss the utility of having a momentum-space representation of the wave function. It appears that a mathematical formalism was already extensively developed in the context of signal processing, but has found so far just a few applications for wave functions in quantum mechanics. The use of the Wigner Transform will be also discussed, and some ambiguous and widespread interpretation of the negativity of the WT will be clarified.

4.4.1 Wavelet Transform Analysis

Having a momentum-space representation of the wave function can be an interesting way to observe interferences within a wave packet. This idea was first introduced in the context of signal processing by Dennis Gabor (1900–1979), a Hungarian-British physicist and engineer, most famous for his work on holography for which he was awarded the Nobel Prize in 1971. One of the main reasons for these developments is that the Fourier Transform does not provide the local information of signals. Thus the FT is not convenient to analyse a signal in the time-frequency domain. In order to describe waveforms with a minimal spread in the time-frequency domain, and keeping a good localisation for both time and frequency, Gabor introduced first the concept of windowed Fourier transform (or Gabor Transform), which is a particular kind of Short-Time Fourier Transform (STFT) using a Gaussian distribution as windows function. The concept of "ondelette" or "wavelet" was introduced by the french engineer Jean Morlet (1982) as a family of functions constructed by using translation and dilation of a single function. A wavelet is defined as an oscillating square-integrable function. The

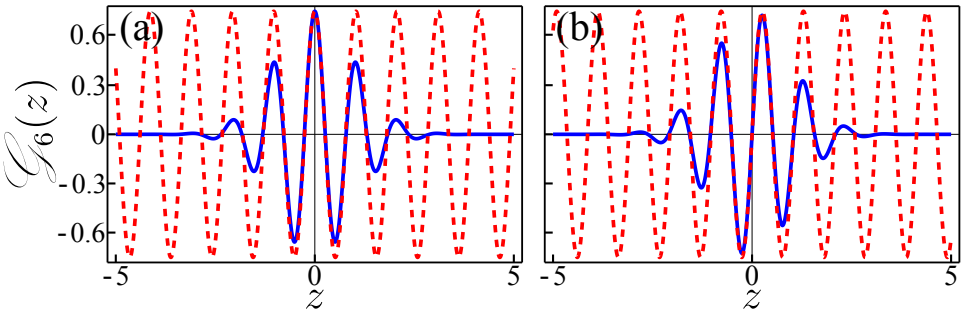

Figure 4.12: Real (a) and imaginary (b) part of the Gabor Wavelet ($\omega = 6$).

main idea was to scan the Fourier Transform of the signal with a window function $\mathcal{G}_a(t-b)$ to extract the information locally, the parameter a measuring the width of the windows and the parameter b translating the function over the whole time domain.

One can thus consider the Wavelet Transform (WT), expressed in this general form by [82]:

$$\mathbb{W}_{a,b}(\psi) = \frac{1}{\sqrt{|a|}} \int_{-\infty}^{+\infty} \psi(x) \mathcal{G}^* \left(\frac{x-b}{a} \right) \mathrm{d}x, \tag{4.29}$$

where a reads for the scales and b a translation parameter which determines the time location of the wavelet.

Different wavelets, discrete and continuous with real and complex values have been developed in the last decades in order to approximate a large variety of signals. I made the choice to use the Gabor wavelet family :

$$\mathcal{G}(z) = \sqrt[4]{\pi} \exp(i\omega x) \exp(-x^2/2), \tag{4.30}$$

which allows us to decompose the wave function into Gaussian packets, which are the basic packets as far as propagation and diffusion are concerned. This extension of the Fourier transform is common in signal processing but has found so far little echo to study wavepacket dynamics [83]. It can be useful to distribute the wave function energy in time, in space and in among wave numbers simultaneously, particularly if interferences phenomena are involved.

The pseudo-frequency of the real part of the Gabor Wavelet can be obtained with:

$$a = \pi^{-1/4} \cos\left(\frac{1}{1} (\omega + \sqrt{2+\omega^2}) \right), \tag{4.31}$$

whereas the frequency of its imaginary part is obtained using a sine instead of the cosine in the previous expression.

The relation between the scales of the WT and the specific frequency is given by:

$$F_a = \frac{F_c}{a\Delta_R}, \tag{4.32}$$

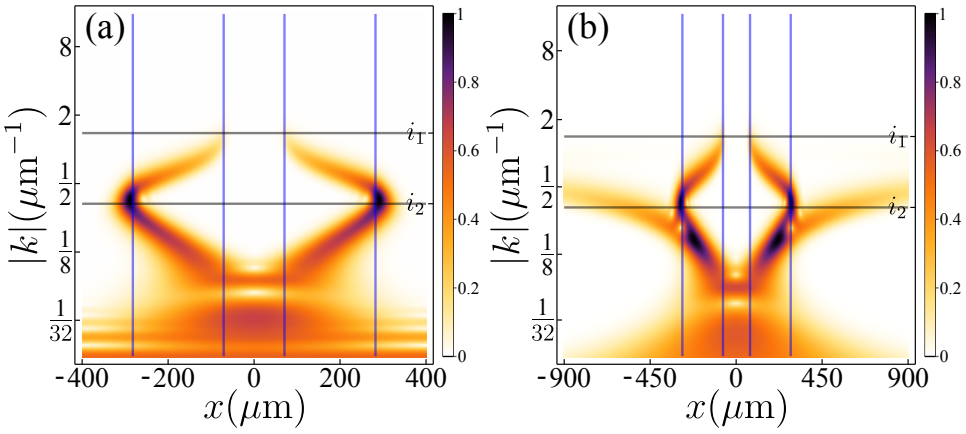

Figure 4.13: a) Wavelet decomposition of the SIP (see Fig. 4.7(a)) and of the Time Crystal (see Fig. 4.8(a)) at t = 100 ps. The dark horizontal lines show the position of the two inflection points of the LPB, and the blue vertical ones the limits of the diffusion cones of the SIP.

where F_c is the center frequency of the wavelet (the argument of the function in Eq. 4.31), a is the scale and Δ_R is the sample rate (which is here the spacial resolution of the grid for the integration Δ_x).

We have applied the Wavelet Transform to two cases of interests: the SIP we have previously calculated and plotted in Fig. 4.7(a) and its Rabi oscillating counterpart (or Time Crystal) plotted in Fig. 4.8. We show in Fig. 4.13 both transforms performed at t = 100 ps. As we deal here with density plots in space and momentum, we have reported on vertical blue lines the limits of the diffusion cones at this time, and with horizontal dark lines the value of the inflection points of the LPB. Note that the absolute value of the momentum $|k|$ is displayed in $\log_4$ scale. These plots, called "scalograms" in signal processing, show how the energy density $|\mathbb{W}_{k,x}|^2$ of the wave function is distributed in the $(x-k)$ plane at t = 100 ps. The wavelet decomposition lets appear in both cases a background of small k-components and an interesting distribution for the rest of the field in the high k values. We see how, within the diffusion cones, the packet contains two different k-components, which creates the interferences in the wave packet, as they are located in the same spatial area. The field starts to diffuse exactly when it meets the inflection point i_1. In (b), one can see the same behaviours due to the SIP, and additionally, the field distribution of the upper polariton component of the packet that "escapes" out of the diffusion cones without being affected by any reflection. Indeed, in this case, there is no real solutions for $\partial_k^2 E_+ = 0$ that give an inflection to reverse the mass m_2 of the upper polariton. Thus the upper polariton component of the packet will always diffuse normally.

4.4.2 Wigner Transform Analysis

The Wigner-Ville quasiprobability distribution or Wigner Distribution Function (WDF) was introduced by Eugene Wigner and Jean-André Ville, obtained from

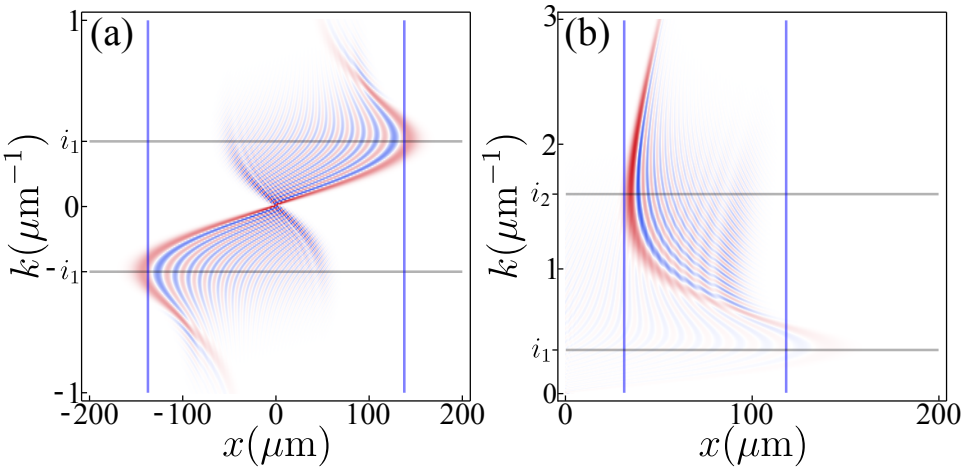

Figure 4.14: (a) WDF of a SIP (from Fig. 4.7 at t = 50 ps) exciting at $k_0 = 0$. (b) WDF of a SIP exciting at $k_0 = i_2$. The dark horizontal lines show the position of the inflection points of the LPB and the blue vertical ones, the position of the diffusion cone at this time. Red color indicate positive values of the WDF whereas blue one indicates negative values.

a wave function ψ and defined by:

$$\mathbb{P}(x,p) = \frac{1}{\pi\hbar}\int_{-\infty}^{+\infty} \psi^*(x+y)\,\psi(x+y)e^{2ipy/\hbar}\,\mathrm{d}y\,, \tag{4.33}$$

where x and p are the independent variables representing the quantum-mechanical position and momentum. The goal was to find an alternative to the Schrödinger wave function by using a density probability in phase space. The WDF has many remarkable properties, such as the space and momentum marginal integrals:

$$\int_{-\infty}^{+\infty} \mathbb{P}(x,p)\mathrm{d}p = |\psi(x)|^2\,, \tag{4.34a}$$

$$\int_{-\infty}^{+\infty} \mathbb{P}(x,p)\mathrm{d}x = |\psi(p)|^2\,, \tag{4.34b}$$

representing the position and momentum energy densities. In addition, the total energy can be obtain by integrating over the entire (x,p) space :

$$\int_{-\infty}^{+\infty} \mathbb{P}(x,p)\mathrm{d}x\mathrm{d}y = \int_{-\infty}^{+\infty} |\psi(p)|^2\mathrm{d}p = \int_{-\infty}^{+\infty} |\psi(x)|^2\mathrm{d}x\,. \tag{4.35}$$

Physically, the WDF can be interpreted as the time–frequency energy distribution. In quantum mechanics, negative values of the Wigner function are commonly viewed as the sign of a non-classical behaviours, due to quantum interferences. However, it has been shown by D. Dragoman (2000) [84] that negative values of the WDF can occur as well in classical optics, without any quantum origins. Two light fields interfering leads to an oscillatory interference term of the WDF, and thus negative values. The statement is even stronger: each field that is non-Gaussian

will induce negativity of the WDF. Indeed, one can decompose a field distribution as a sum of Gaussian fields, using for example the Gabor decomposition. Thus, the negative values of its WDF will be due to interferences among the Gaussian fields.

We have applied the WDF to the case of the SIP, as we did before with the Wavelet Transform. In Fig. 4.14(a) is plotted the WDF of the SIP generated at resonant excitation, the counterpart of Fig. 4.13(a). The pattern is similar to the one obtained with the WT, we see how the energy distribution is reflected in space when passing the inflection point $\pm i_1$. Another consequence of the self-interferences is the alternation of positive and negative values of the WDF. In (b) the same but this time exciting the second inflection point at $k_0 = i_2$. We see how the reflection occurs in the opposite way, the diffusive mass m_2 changing from negative to positive again when crossing the second inflection point i_2.

4.5 SIP generation in realistic systems

In this last Section we discuss on the realisation of SIP in a realistic system. All of the previous study has been purely theoretical, and the mechanism at the origin of the SIP generation is now well understood. We show here how real physical parameters like the choice of the masses of the particles and intrinsic effects of the cavity system with radiative decay can affect the formation and propagation of a SIP.

4.5.1 SIP in dissipative systems

So far, in all this Chapter, we have only considered conservative systems, neglecting all the decay sources that are normally present in the polariton systems. Polaritons live with a finite lifetime and we have already shown in Chapter 2 how this affects the dynamics. Therefore, one can wonder how realistic conditions could affect the SIP generation? Here we perform the same calculations but this time adding decay terms into the Hamiltonian Eq. 4.3. For simplicity, we only consider the photon lifetime, by adding a term $-i\hbar/\gamma_C$ in the first matrix element. The value of the photon lifetime is set to $\gamma_C = 5$ ps, in agreement with the experimental observations reported earlier [44].

In Fig. 4.15(a), we show the propagation of a lower polariton wave packet in a SIP configuration, the same we used in Fig. 4.7(a) but this time including the photon lifetime. Self-interferences are still visible around ten times the lifetime and then vanish. This is due to the fact that photon-like polaritons (small k components) are more damped than the exciton-like ones (high k components) and with one part of the overlapping wavefunction gone, the self-interference disappears. One can see (b) how the current probability tends to be uniform on both sides of space. It can also be observed through the wavelet decomposition (d), here at $t = 100$ ps, that only the high k-components remain ($|k| > i_1$), where the polaritons are strongly excitonic and thus insensitive to the photon radiative decay. Another way to see this

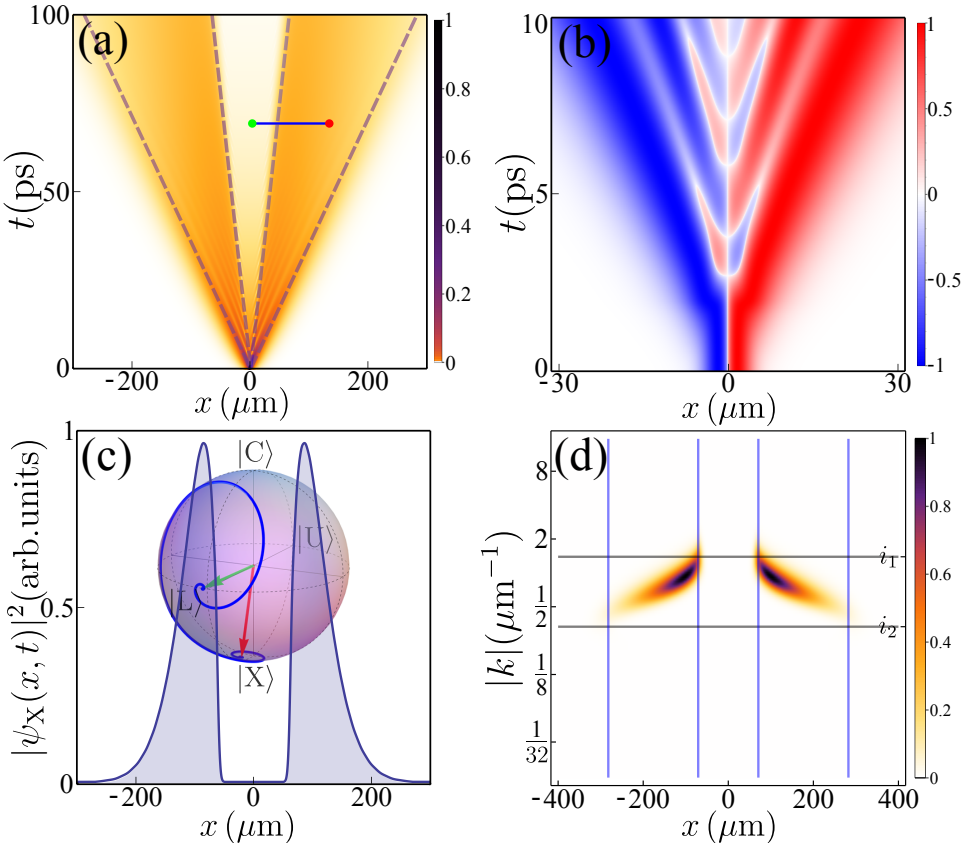

Figure 4.15: (a) Propagation of a lower polariton packet with non-zero photon lifetime $\gamma_C = 5$ ps. (b) Current probability j at early times. (c) Intensity profile at $t = 100$ ps with the evolution of the quantum state on the Bloch sphere corresponding to the path (from green to red) plotted in (a). (d) Wavelet decomposition of (a) at $t = 100$ ps. (e-f) Propagation and wavelet decomposition in the same conditions but exciting with a momentum at $k_0 = i_2$. One can see how the SIP disappears when the overlap between k components is lost by radiative decay of the photonic part. The parameters are the one used in Fig. 3 (e-l) of the main text.

effect is to look at the evolution of the quantum state in this region (cf. the Bloch Sphere in panel (c)), that converges quickly to the $|X\rangle$ state.

Unlike the non-dissipative case, within the diffusion cone, the packet is only composed of a singe k component whereas at least two different k components are needed to obtain the self-interferences (see Fig. 4.13(a)). As a result, the wave function takes a two-peaked shape with a strong depletion of particles at the center (c). In contrast, a SIP formed at the second in inflection point, is much more robust to decay. The interferences persist at all times as shown in Fig. 4.16, since both components around i_2 remain present, as displayed on the scalogramm in panel (b).

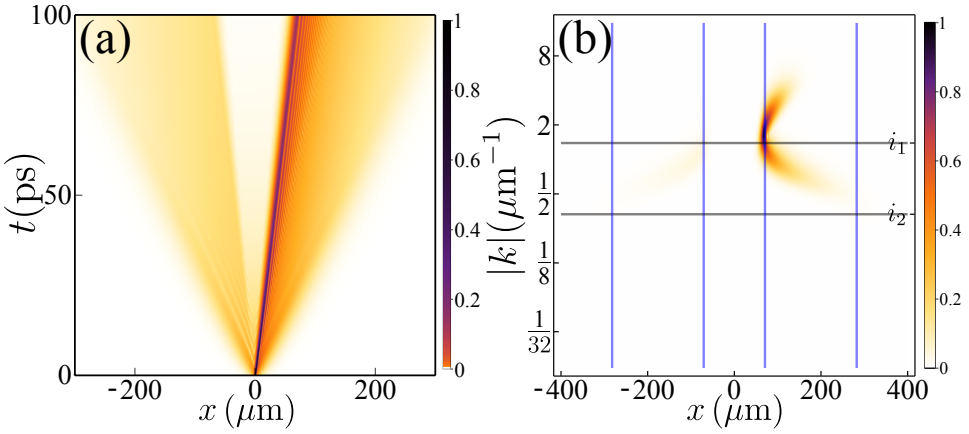

Figure 4.16: (a-b) Propagation and wavelet decomposition in the same conditions but exciting with a momentum at $k_0 = i_2$. One can see how the SIP disappears when the overlap between k components is lost by radiative decay of the photonic part.

4.5.2 On the choice of the mass parameters

The two main ingredients needed to generate a SIP are i) the access to an inflection point of the LPB and more importantly ii) to make the wave function spread over this point in k-space. To obtain the largest spread in the Fourier space, one needs to reduce as much as possible the size of the laser spot. This is experimentally limited by the laser's wavelength (in a good approximation). The smallest laser beam reported in the literature for such polariton experiments was about $\sigma = 2$ µm [85, 86], which corresponds to the values that we have considered before.

On the other hand, the steepness of the polariton dispersion depends on the effective masses of the particles m_C and m_X. The smaller they are, the more the dispersion will be confined in a small range of k, setting the inflection points closer to $k = 0$.

In this study, we have made the choice of small particles mass and with a small ratio : $m_X/m_C = 80$. In real samples, the exciton mass m_X is typically two orders of magnitude larger than the photon mass m_C, that has for consequence to flatten completely the LPB at high ks, which forbids the access to the second inflection point of the system. However, for generality, I provide theoretically the most general picture of the effect, two coupled fields giving rise to two inflection points. The role of the second point is however merely to iterate the effect of the first one, resulting in a central area shielded from the interferences during propagation. Such cases with $m_X \to \infty$ have actually been treated in Section. 4.3.5. With today's polariton parameters, such a double-reflection SIP might indeed not be readily reachable. But there is no fundamental restriction that prevents its actual realization using other materials or possibly other platforms, such as modulated photonic lattices [87], crystals [88] or coupled waveguides [89], with several inflection points potentially reachable. Photonic crystal slabs are indeed known to provide a better field confinment and thus could lead to stronger polaritonic effects.

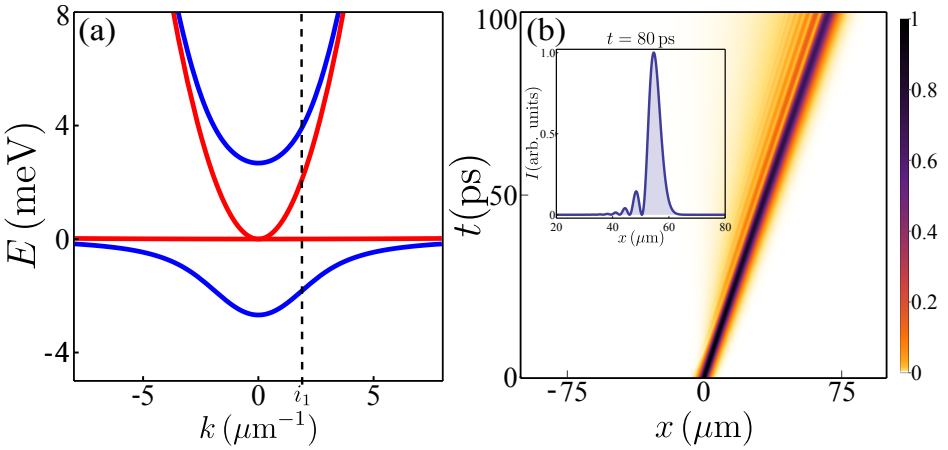

Figure 4.17: (a) Propagation of a polariton packet with parameters typical of today's samples, exciting the lower branch at the inflexion point with a Gaussian spot of spatial extent $\sigma_x = 2$ µm. The parameters of the dispersion are the ones of a sample used in a previous work, see ref [44]. The SIP remains clearly visible, with soliton-like propagation of its main peak.

In Fig. 4.17 we show how would a SIP be produced with real parameters, and through the simplest approach, that is sending a pulse light onto the sample. Here the parameters taken are typical of today's sample (see ref. [44]) and exciting with a spot size of $\sigma_x = 2$ µm. This does not provide the full picture of the SIP, but interferences are still visible, the cancellation of the diffusion is as well.

4.5.3 SIP generation with a Potential

In the case of unavailable system parameters or equipment able to reach the SIP regime, we provide here an alternative method to spread the wave function that involves external factors, namely, by colliding it onto a potential. It is well known that under some conditions (potential strength), a wave packet that bounces into an harmonic potential will squeeze, increasing *de facto* its spread in k. This squeezing of the wave function induced by the harmonic potential could bring this additional spread in k needed to reach the SIP regime in the cases where physical parameters would limit it. In Fig. 4.18 we show the propagation of a polariton wavepacket in the presence of harmonic potentials $V(x)$ for the photonic and excitonic fields. It reads:

$$V(x) = \frac{1}{2} m_{\mathrm{C,X}} \omega_{\mathrm{C,X}}^2 x^2 , \tag{4.36}$$

where the frequency is set to $\omega_{\mathrm{C,X}} = \hbar/(m_{\mathrm{C,X}}\sigma_x^2)$. While the free propagation of a broad packet $\sigma_x = 20$ µm does not exhibit interferences (a), the staggering on the branch being too small, the same packet propagated inside the potentials squeezes as it bounces back one wall and then develops self-interferences (b), the squeezing reducing the packet size in space, thereby increasing its spread on the branch on either side of the in infection point. Essentially the same result is obtained with

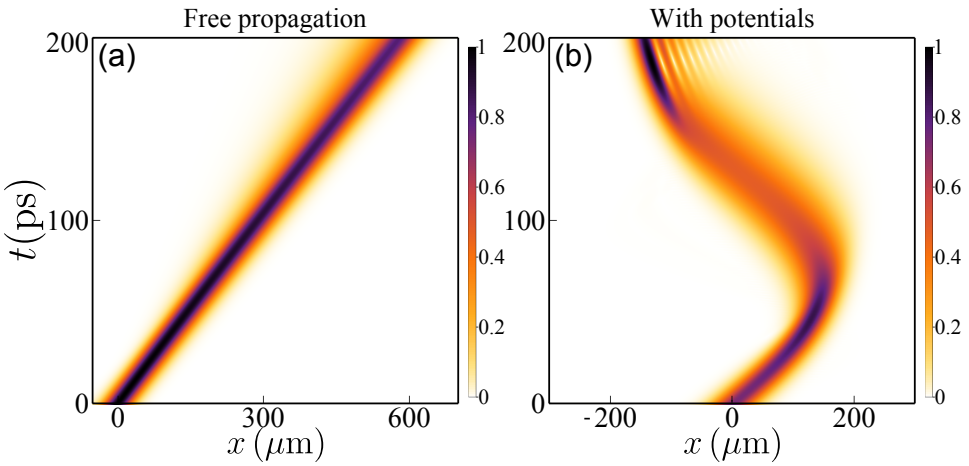

Figure 4.18: A polariton wavepacket with width $\sigma_x = 20$ µm imparted with a momentum $k_0 = i_1$ and (a) propagating freely or (b) within an harmonic potential.

only the photonic potential. Switching it off would allow to free the SIP into free propagation. A video of the full wave packet dynamics (of Fig. 4.18(b)) with the corresponding Wavelet Transform is available on-line in the supplementary section of ref. [80].

4.5.4 SIP in Two Dimensions

Up to now, we have considered 1D cases, which are indeed possible in heterostructures by confining the two other dimensions. We can mention the work of Wertz *et al.* (2010) [85] with polaritons in quantum wires. Polariton propagation is however more popular in 2D geometry [90] and we briefly discuss what happens in this case. Since the system is linear and uncoupled in transverse coordinates, the dynamics follows trivially from the previous results and symmetry. With a full radial symmetry, all the phenomenology is conserved in 2D, with rotational invariance. In Fig. 4.19 (a), the propagation of a SIP at 100 ps is shown, after propagating a narrow Gaussian wave packet at $t = 0$, and at the origin of the plane. This case is the 2D counterpart of the one of Fig. 4.7. The propagation and thus the shape of the wave packet are similarly determined by the dispersion and the way it is excited. There is also, depending on the proximity of the second inflection point, a central area shielded from the interferences, which now turns to a disk in the x-y plane. Its diameter is also determined by a zero of $\partial_k^2 E_- = 0$. Similarly to the 1D case, one can trigger the SIP dynamics without needing an ultra sharp packet, simply by imparting a momentum (close to the inflection point of the LPB). In Fig. 4.19 (b) one can see the propagation of a smaller wave packet when exciting the dispersion at the first inflection point $k_x = k_y = i_1$. The shape of the packet and the amount of interferences can thus be controlled by tuning the momentum and the initial shape of the packet. In Fig. 4.19 (c) we show a case where self interferences are produced

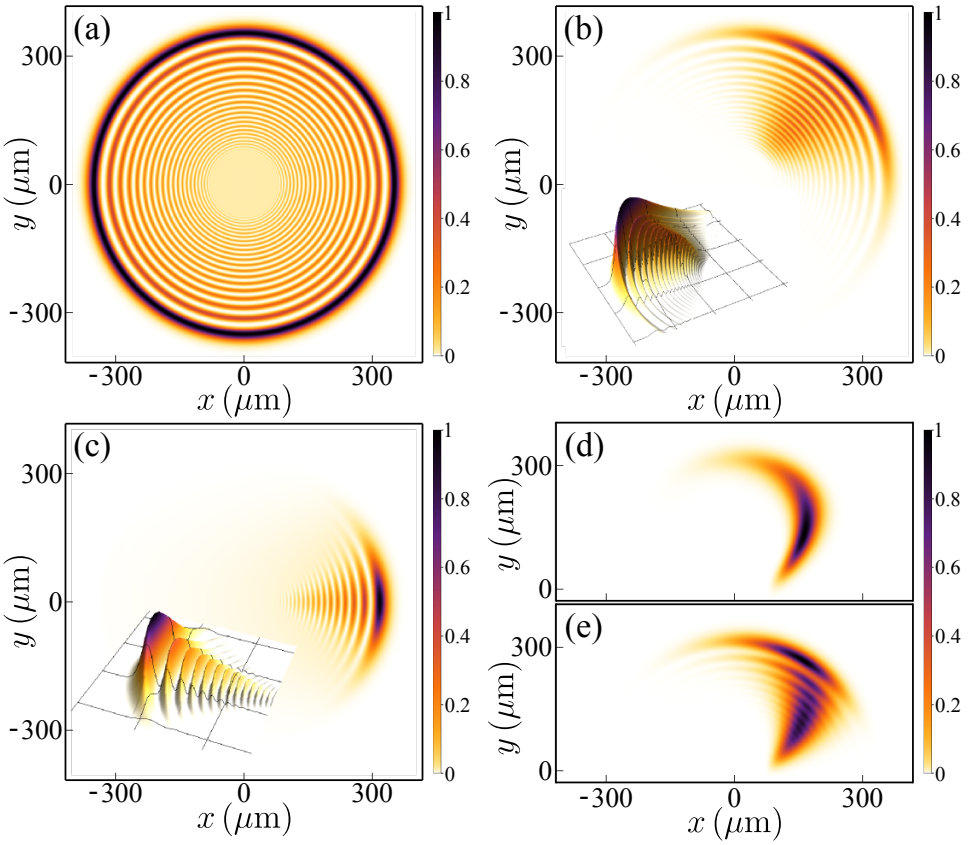

Figure 4.19: SIPs in 2D. (a) With full radial symmetry when self-interfering in all directions. A central disk is shielded from interference like in the 1D case and features a plateau of lower polaritons. The initial packet is sharp in both x and y directions, $\sigma_x = \sigma_y = 2$ µm. (b) When imparted with momentum, the packet self-interferes in the direction of its propagation and diffuses radially, $k_x = k_y = i_1$ and $\sigma_x = \sigma_y = 4$ µm. (c-e) The amount self-interferences can be controlled by adjusting the momentum and the size of the initial packet in the different directions. (c) $k_y = 0$, $k_x = i_1$, $\sigma_x = 4$ µm and $\sigma_y = 10$ µm. (d-e)$k_x = k_y = i_1$ with $\sigma_x = 4$ µm, $\sigma_y = 20$ µm for (c) and $\sigma_y = 10$ µm for (e).

along the x-axis and by limiting the diffusion of the packet in y, by setting $\sigma_x > \sigma_y$. Other configurations leading to packets with new shapes can also be obtained, see Fig. 4.19 (d-e). In a recent work by O. Voronych *et al.* (2015) [91], the generation of 2D X-waves was proposed by exciting the LPB past its inflection point, where the effective mass is negative. Unlike bright solitons and similarly to SIPs, this kind of waves does not require nonlinearity to maintain their shape. The authors have however mentioned that in their case, nonlinearity allows the spontaneous X-waves formation from an initial Gaussian wave packet. We have not studied in details the SIP in presence of nonlinearity, but we have seen that a SIP is quite robust for reasonable polariton-polariton interactions. A further work could consist in studying the SIP mechanism thought a full nonlinear model, including as well pumping and the relevant decay/dephasing terms.

4.6 Conclusions

In this Chapter, I have introduced the concept of Self-Interfering Wave Packet developed in the polariton systems framework. The non-linear polariton dispersion allows us to produce new wave packets composed of harmonics of different effective mass, leading to non-trivial interference patterns.

In Section 4.2, we have summarized the general framework of non-trivial wave packets, to which the SIP adds a new member. We have mentioned potential applications for such packets and how, from a more fundamental point of view, they challenge our understanding of the notion of particle in classical and quantum mechanics.

We have seen how coupled fields result in unconventional wave propagation and exhibit surprising properties, such as an impossible real-space localisation of both the photonic and excitonic components of a polariton field, as seen in Section 4.3.1. This is in stark contrast with the reciprocal space, where k-space simultaneous localisation is possible. This shows how polaritons are more properly wave-like objects. Their non-parabolic dispersion relation also leads to the emergence of different concepts of effective mass. Propagating a wave packet whose k-components straddle over the mass divergence induces self-interferences (Fig 4.6 and 4.7). More complicated patterns can be obtained if one no longer excites the eigenstate of the system, merging Rabi oscillations to the SIP features. This can lead to ordered honeycomb lattices in space and time (Fig. 4.8). Some analytical expression for these solutions can be obtained by approximating the polariton dressed momentum distribution $k_\Omega^2 - k^2$ by another distribution (a Lorentzian for instance), easier to Fourier-Transform. We found complex series expansions (Eq. 4.26) that show how the interferences emerge in time, and how the peaks are produced at the Rabi frenquency Ω_R. The Wavelet Transform was an important tool to understand the SIP mechanism, providing a clear view of the repartition of the field energy density in a momentum-space representation. We saw how the different k-components of the packet, containing both positive and negative effective mass, were present within the diffusion cones.

Finally in Section 4.5, we have discussed the feasibility of the SIP generation in experimental conditions, taking the radiative decay of the photon into account. We discussed as well what realistic mass parameters are available to experimentalist to observe this dynamics in the laboratory. The main experimental limits are the availability of samples with small particles masses (eventually also allowing to access the second inflection point) and the use of very highly focused laser spots. With today's polariton technologies, the full picture of the SIP might not yet be reachable, but the effect should still be visible under certain conditions (Fig. 4.17). If not, we provide another possible way to amplify the spread on the LPB by colliding the wave packet against a potential, squeezing the packet and increasing *de facto* the spread on the branch, which can help to reach the SIP regime.

SIP are very promising objects and could lead to interesting applications, for example by exciting polaritons with quantum light [38], quantum SIP could propa-

gate in properly wired polariton circuits to perform Linear Optical Quantum Computing, thanks to the linearity of the effect. SIP can indeed carry qubit states, unlike solitons with which they otherwise share similar propagation qualities.

Chapter 5

Rabi oscillating Vortices

I don't believe in psychology.
I believe in good moves.
Bobby Fischer.

Contents

In this Chapter are presented some of the last results that have been obtained during the course of this thesis. They address the topical question of polariton vortices. As in the opening chapters, they present joint experimental and theoretical efforts. We have demonstrated the generation of Rabi oscillating vortices by pulsed-excitation. The results have been reproduced theoretically through the

usual polariton Hamiltonian with adequate initial conditions. Vortices oscillating in space on top of their Rabi oscillations in time can be obtained by imparting a momentum to the wave packet. The orbital angular momentum is studied for the different cases.

5.1 Introduction

This 5th Chapter is devoted to the study of vortices in polariton condensates, and more specifically to their oscillations powered by Rabi oscillations. This work was impulsed by Lorenzo Dominici, my experimentalist colleague and close co-worker from Lecce, who discovered intriguing dynamics while studying the dynamics of vortices in polaritons, a problem that he regularly combines and revisits in countless configurations. Following the footsteps of the previous experiments on the coherent control of the polariton Rabi oscillations and the polariton polarization shaping, he has with his co-workers in Lecce observed the generation of Rabi-powered vortex oscillations in real space. This was initially achieved by using two series of pulses, the first one creating a stable vortex in the polariton condensate, and the second one disturbing the density's homogeneity and inducing the vortex oscillations. These results can be reproduced by using our standard coupled-Schrödinger Equations for the polaritons, fed with the adequate initial state. The different decay sources present in the system can be added in the Hamiltonian in order to model the oscillations damping. The system can also be solved formally and analytical solutions can be derived. To get more insights into this dynamics, we study the evolution of the Orbital Angular Momentum (OAM) and see its connection with the Rabi coupling. Similar but more complex vortex oscillations are theoretically found by imparting a momentum to the vortex beam, with the appearance of a second polariton vortex, which was also demonstrated experimentally. These results suggest that polariton vortices could be used to carry high quanta of OAM, similarly to electron beams [92].

The Chapter is organised as followed. In Section 5.2, we first give a short overview of the physical systems in which vortices can be encountered, particularly at the quantum level. In Section 5.2.1 are derived the vortex solutions for a single Schrödinger Equation. An analytical solution is found for a Laguerre-Gauss function of arbitrary topological order l as initial condition. A solution is also derived for beams with imparted momentum, which will be the basis solution to describe the propagating vortex experiment. In Section 5.3 is derived the solution for the full polariton system, *i.e.* vortex solutions for the coupled-Schrödinger Equations by considering pulsed excitation. We show that the system can be formally solved for a general linear Hamiltonian. Updated versions of the Hamiltonian that include the polaritons decay rates are also derived. Section 5.4 is devoted to the study of the OAM of the Rabi-oscillating vortices. After reminding the general definitions in the present context, we consider the OAM of a quantum superposition of states, as it is the case for the polariton fields. A specific Rabi-Orbit Coupling

can be obtained. Experimental results of the two pulses experiment are presented in Section 5.5, showing a good agreement with the theory. The coherent control of the vortex trajectories can also be obtained, with a single or a pair of vortices. The resulting shifted vortex is modelled analytically. The last experiment, whose results are in Section 5.6, shows that the vortex oscillations can also be obtained by propagating a single Laguerre-Gauss beam. The two polariton sub-fields (UP and LP) are thus spatially separated due to their mass imbalance, which induces the vortex precession. We see theoretically that high OAM values can be obtained in the first stage of the propagation, before the polaritons get completely split in space. The simultaneous presence of the two polariton vortices has been observed experimentally. The main conclusions are presented in Section 5.7

The results presented in this Chapter were among the lasts I have obtained in the course of my Ph. D, thus they are not necessarily in their definitive and "complete" form, as they are still within development as I write these lines.

5.2 Vortices in Quantum Fluids

Vortices are commonly encountered in classical systems where a fluid dynamics involves rotation. They can appear at various scales of space and time, for instance when the reader is stirring their coffee whilst reading this text, by removing the plug of a bath or during hurricanes. In all these cases, the local rotation of the fluid is given by the vorticity $\vec{\omega} = \vec{\nabla} \times \vec{v}$. If $\vec{\omega} = 0$, the fluid is called *irrotational*, *i.e.* it does not rotate like a rigid body. Vortices are in general not stable configurations.

At the quantum level, vortices—also called "topological charges"—or quantized circulation in superfluids, have been initially predicted by Onsager in 1949 in his work on superfluid Helium. But these predictions were only widely accepted after Feynman's contributions in 1955. Further theoretical developments have also been made by Gross and Pitaevskii (1961). They are more generally encountered in systems that can be described by a complex wave function and whose phase plays a key role. The velocity field $\vec{v}$ around the vortex is characterized by a quantum of circulation:

$$\oint \vec{v}.\mathrm{d}\vec{l} = \frac{2\pi\hbar}{m}. \tag{5.1}$$

Quantum vortices can be encountered in a wide range of superconductors [93] where the vortex dynamics is mainly governed by the thermal and quantum fluctuations. Such vortices can be as well manipulated by applying external forces, such as electric currents. Superconductors vortices were extensively studied as they can carry Abrikosov vortices (fluxons) and exhibit some complex ordering like Abrikosov lattices, spin glasses etc.

Bose–Einstein Condensates (BEC) are also a good platform to generate quantum vortices since they are also superfluid systems. The vortex generation in a BEC has been first demonstrated by Cornell's group in 1999 [94] following his previous works on BEC for which he was awarded the Nobel prize in 2001. It was

later demonstrated that vortices can even appear spontaneously during phase transitions in which the BEC formation occurs [95]. Vortex lattices were also observed in rotating BEC by the group of W. Ketterle [96], exhibiting a high vortex lifetime ($\approx$ 1min). Vortex precession was observed in atomic BECs. We can mention another work of the Cornell's group, related to our polariton vortices behaviours, namely, that of B. P. Anderson *et al.* (2000)[97], where the authors considered a BEC made of a superposition of two internal states of ^{87}Rb. The vortex motion is in this case attributed to a Magnus effect applied on the vortex into the quantum fluid.

More recently, it has been demonstrated that similarly to optical fields [98, 99], electron beams could propagate with a phase singularity [100], giving a new degree of freedom to the electrons. Shortly later, electron vortex beams with high quanta of angular momentum (up to 100$\hbar$) were realised [92]. Electron beams can find potential applications in electron microscopy of magnetic and biological specimens.

The polariton community was of course not left behind in the investigation of vortex experiments. K. G Lagoudakis *et al.*(2008) [101] have reported the formation of pinned single quantized vortices in the Bose-condensed phase of a polariton fluid, giving new clues to understand the superfluid nature of the polariton condensates. Quantum half-vortices were later observed in polariton condensates [102] by the same group, following their prediction by Yu. Rubo [103]. We can also mention the work of D. Sanvitto *et al.*(2010) [10] where metastable persistent polariton superflows were observed. They have shown how to sustain quantized angular momentums that can be transfered to the steady-state condensate, insuring a long-lived vorticity. The last advances on the field were brought by L. Dominici *et. al*(2015) [104], where stable half-vortex spiralling and vortex twin-charge splitting was observed. In their system, the vortex dynamics is ruled by the interplay between the nonlinearity and the disorder landscape.

Many applications based on OAM beams are already considered. For example, quantum correlations between the OAM variables can be used in quantum information processing and notably in protocols for quantum key distribution [105]. Quantum OAM based multiplexing was developed and used to increase the efficiency of millimetre-wave wireless communications [106]. The data exchanged between OAM beams and using OAM multiplexing was reported to reaches Terabit rates values in free-space transmission [107]. A proposal of polariton gyroscope has even been made [108], it exploits the macroscopic response of the system to small perturbations to create sensitive devices.

5.2.1 Vortex Solution for single Schrödinger Equation

In this section, we derive the solution of the two-dimensional Schrödinger Equation (2DSE) for a free particle by considering a vortex as initial condition. The 2DSE

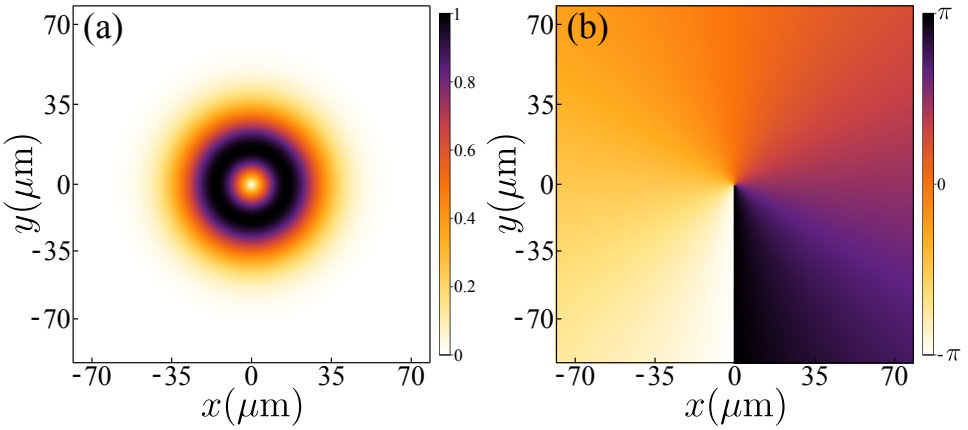

Figure 5.1: Laguerre-Gauss beam, imprinting the vortex phase. (a) $|\psi_0|^2$ from Eq. 5.4. (b) Corresponding phase profile. It presents a phase singularity in the minimum of intensity, and a 2π phase jump along. Here the winding number is $l = 1$ and the spot size $\sigma_R = 15$ µm.

reads:

$$i\hbar\partial_t \psi(x,y,t) = -\frac{\hbar^2}{2m}\nabla^2\psi(x,y,t)\,. \tag{5.2}$$

It can be formally integrated by moving to the momentum space representation :

$$\tilde{\psi}(k_x,k_y,t) = e^{-\frac{i\hbar(k_x^2+k_y^2)t}{2m}}\tilde{\psi}_0(k_x,k_y)\,, \tag{5.3}$$

with $\tilde{\psi}_0(k_x,k_y)$ the initial condition in the k-space. As initial condition, we consider a Laguerre-Gauss beam, imprinting the phase of the vortex, which reads in Cartesian coordinates :

$$\tilde{\psi}_0(x,y) = \sqrt{x^2+y^2}^{|l|}\, e^{\frac{-x^2-y^2}{2\sigma_R^2}}\, e^{il\tan^{-1}(y/x)}\,, \tag{5.4}$$

where l is the winding number of the vortex and σ_R gives the spot size. The corresponding expression can be as well obtained in the momentum space representation by Fourier Transform:

$$\tilde{\psi}_0(k_x,k_y) = i^{2l}\sigma_R^{2+2l}(k_x-ik_y)^l e^{\frac{1}{2}(k_x^2+k_y^2)\sigma_R^2}\,. \tag{5.5}$$

The previous expression can now be plugged into Eq. 5.3 and the Inverse Fourier Transform be used to obtain the general solution (normalised) in real space:

$$\psi(x,y,t) = \frac{i^l\sigma_R^{1+l}(x-iy)^l}{\sqrt{l!\pi}(\sigma_R^2+\frac{i\hbar t}{m})^{l+1}} e^{-\frac{(x^2+y^2)}{2\sigma_R^2+\frac{2i\hbar t}{m}}}\,. \tag{5.6}$$

In the following we will mainly consider cases where $l = 1$. The previous equation can thus be reduced to:

$$\psi(x,y,t) = \frac{\sigma_R^2(y+ix)}{\sqrt{\pi}(\sigma_R^2+\frac{i\hbar t}{m})^2} e^{-\frac{(x^2+y^2)}{2\sigma_R^2+\frac{2i\hbar t}{m}}}\,. \tag{5.7}$$

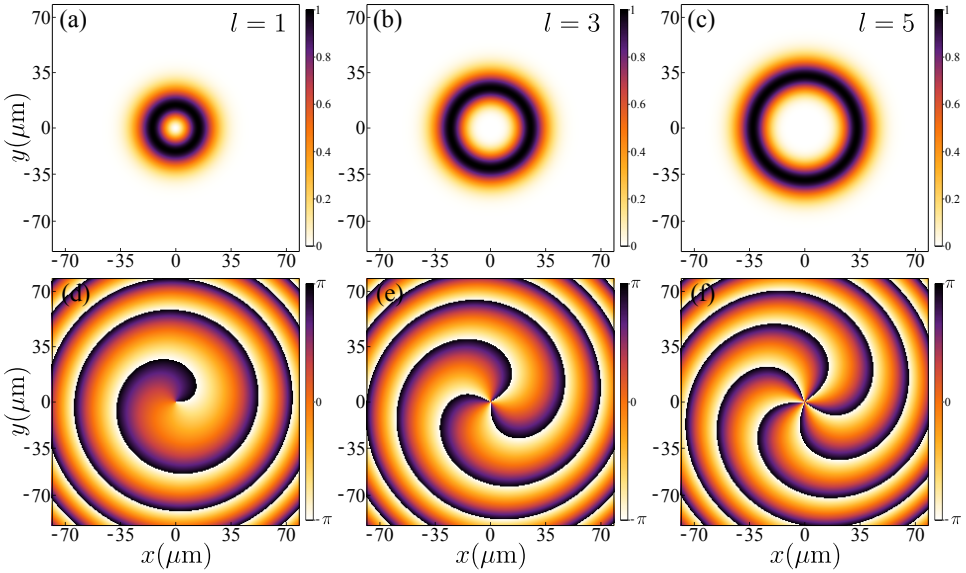

Figure 5.2: Laguerre-Gauss beams of different orders, and at t = 150 ps. (a-c) $|\psi_0|^2$ for three different winding numbers. (d-f) Corresponding phase profile. Parameter : σ_R = 10 µm.

This wave function is plotted in intensity and phase in Fig. 5.1. The vortex beam presents a 0-intensity minimum in its center (a) while the exterior behaves like a Gaussian. To the vortex core is associated a phase singularity (b) along which a 2π phase shift occurs.

This solution shows a similar behaviour than a traditional Gaussian, diffusing with time. The phase begotten by the vortex also swirls in time around it. This can be seen in Fig. 5.2, where we have plotted the wave function intensity and phase of Eq. 5.6 for different winding numbers and at t = 150 ps.

The system can also be solved for a propagating vortex, *i.e.* a vortex with an imparted momentum as initial condition, Eq. 5.4 being simply multiplied by a term $e^{i(k_{0x}x+k_{0y}y)}$. The solution is found in the same way as before and gives :

$$\psi(x,y,t) = \frac{\sigma_R^2\left((y+ix) - \frac{(k_{0y}+ik_{0x})\hbar t}{m}\right)}{\sqrt{\pi}\left(\sigma_R^2 + \frac{i\hbar t}{m}\right)^2} e^{-\frac{(x^2+y^2)-2i(k_{0x}x+k_{0y}y)\sigma_R^2) + \frac{i(k_{0x}^2+k_{0y}^2)\hbar\sigma_R^2 t}{m}}{2\sigma_R^2 + \frac{2i\hbar t}{m}}} . \quad (5.8)$$

Theses vortex solutions will constitute the basis of the polaritonic vortices in the following.

5.3 Vortices in Polariton Fluids

In this Section we develop and solve the equations describing polariton vortices. We show how to deal with the pulse excitation and the way to introduce the polariton decay rates, by updating the polariton Hamiltonian.

A vortex evolving in a polariton fluid can be described by two coupled 2D Schrödinger Equations (c-2DSE), which read:

$$i\hbar\partial_t \boldsymbol{\psi} = \mathbf{H}\boldsymbol{\psi} + \mathbf{F}\,. \tag{5.9}$$

This can be more clearly expressed in matrix form:

$$i\hbar\partial_t \begin{pmatrix} \psi_{\mathrm{C}} \\ \psi_{\mathrm{X}} \end{pmatrix} = \begin{pmatrix} \frac{-\hbar^2}{2m_{\mathrm{C}}}\partial^2_{x,y} - i\frac{\hbar}{\gamma_{\mathrm{C}}} & \frac{\hbar\Omega_{\mathrm{R}}}{2} \\ \frac{\hbar\Omega_{\mathrm{R}}}{2} & \frac{-\hbar^2}{2m_{\mathrm{X}}}\partial^2_{x,y} - i\frac{\hbar}{\gamma_{\mathrm{X}}} \end{pmatrix} \begin{pmatrix} \psi_{\mathrm{C}} \\ \psi_{\mathrm{X}} \end{pmatrix} + \begin{pmatrix} F_1 + F_2 \\ 0 \end{pmatrix}, \tag{5.10}$$

where Ω_{R} is the Rabi frequency and $\gamma_{\mathrm{C,X}}$ is the lifetime of the photon/exciton. Here, the initial condition is the vacuum and the system is excited via one or two pulses F_1 and F_2, that could be a Gaussian pulse or a Laguerre-Gauss pulse that carries the vortex phase.

Like in the experimental case, we first consider a Laguerre-Gauss pulse F_1, creating the polariton vortex. It reads:

$$F_1(x,y,t) = \sqrt{x^2+y^2}^{|l|}\, e^{\frac{-x^2-y^2}{2\sigma_R^2}}\, e^{il\tan^{-1}\left(\frac{y}{x}\right)} e^{-\frac{(t-t_{01})^2}{2\sigma_t^2}}\, e^{-i\omega_L t}\,, \tag{5.11}$$

where l is the winding number of the vortex and σ_{R} gives the spot size. The pulse is sent at a time $t = t_{01}$ at the frequency ω_{L}. A second pulse, Gaussian this time, is sent at $t = t_{02}$:

$$F_2(x,y,t) = e^{\frac{-x^2-y^2}{2\sigma_R^2}}\, e^{-\frac{(t-t_{02})^2}{2\sigma_t^2}}\, e^{-i\omega_L t} e^{i\theta}\,, \tag{5.12}$$

where we have introduced θ to be the relative phase between F_1 and F_2. This second pulse has a central role as it disturbs the Rabi oscillation regime and shift the minimum of intensity of the wave function, inducing vortex oscillations.

Equation 5.9 can be formally integrated in the Fourier space as we did in the previous Section (see Eq. 5.3), it thus reads:

$$\tilde{\boldsymbol{\psi}}(t) = e^{-i\tilde{\mathbf{H}}t}\left(\tilde{\psi}(0) - \int_0^t ie^{i\tilde{\mathbf{H}}t'}.\tilde{\mathbf{F}}(t')\mathrm{d}t'\right), \tag{5.13}$$

where the Hamiltonian $\tilde{\mathbf{H}}$ and the pulse vector $\tilde{\mathbf{F}}$ are as well easily obtained in the Fourier space. It is important to note that the temporal part of the two pulses F_1 and F_2 has the same mathematical form:

$$F(x,y,t) = F_s(x,y)F_t(t)\,, \tag{5.14}$$

with $F_t(t) = e^{-\frac{(t-t_0)^2}{2\sigma_t^2}}\, e^{-i\omega_{\mathrm{L}}t}$ the temporal part and F_s the spatial part of the pulse. This is true assuming that the two pulses have the same temporal spread and are sent at the same energy. Thus, the integral in Eq. 5.13 needs to be calculated only one time. This integral, that captures the transient feature of the pulses can also be integrated exactly, but it leads to a long and heavy expression composed of the error function $\mathrm{erf}(t')$ (see Eq. 2.17 of Chapter 2) that are too cumbersome be written here.

5.3.1 Adding the Polariton lifetime

We have already said how vortex oscillations can be obtained by sending a second Gaussian pulse on the unperturbed vortex, which leads to circular oscillations of the vortex into the beam. Experimentally, the same oscillations are observed but they are rapidly damped after a few picoseconds, the vortex becoming immobile again. As the vortex oscillations are powered by the Rabi oscillations between the photonic and excitonic field, we suspect that the lifetime imbalance between the upper and lower polaritons plays as well a key role in this mechanism.

We can thus introduce the upper polariton lifetime into our equations, since it has the strongest influence on the Rabi oscillations, as we saw in the previous Chapters. The lifetime of the Upper Polariton can be added into the Hamiltonian once written in the Upper/Lower Polariton basis as follows:

$$\tilde{\mathbf{H}}_d = \begin{pmatrix} E_{\mathrm{L}} & 0 \\ 0 & E_{\mathrm{U}} - i\frac{\hbar}{\gamma_{\mathrm{U}}} \end{pmatrix}, \tag{5.15}$$

where $E_{\mathrm{L,U}}$ are the dispersion relations of the Lower and Upper polaritons, respectively. The full expressions are already given in Eq. 2.3 of Chapter 2. Then, one can come back to the Hamiltonian in the Exciton/Photon basis, by applying P, the eigenvectors matrix of $\tilde{\mathbf{H}}$ as follow :

$$\tilde{\mathbf{H}}_m = \mathrm{P}\tilde{\mathbf{H}}_d\mathrm{P}^{-1}. \tag{5.16}$$

The modified Hamiltonian $\tilde{\mathbf{H}}_m$ is thus expressed as :

$$\tilde{\mathbf{H}}_m = \begin{pmatrix} \frac{k_x^2+k_y^2}{2m_{\mathrm{C}}} - \frac{i}{2\gamma_{\mathrm{U}}} + \frac{i}{2\gamma_{\mathrm{U}}}\frac{(k_x^2+k_y^2)m_-}{\sqrt{(k_x^2+k_y^2)^2m_-^2+16\Omega_{\mathrm{R}}^2}} & \frac{\Omega_{\mathrm{R}}}{2} - \frac{2i}{\gamma_{\mathrm{U}}}\frac{\Omega_{\mathrm{R}}}{\sqrt{(k_x^2+k_y^2)^2m_-^2+16\Omega_{\mathrm{R}}^2}} \\ \frac{\Omega_{\mathrm{R}}}{2} - \frac{2i}{\gamma_{\mathrm{U}}}\frac{\Omega_{\mathrm{R}}}{\sqrt{(k_x^2+k_y^2)^2m_-^2+16\Omega_{\mathrm{R}}^2}} & \frac{k_x^2+k_y^2}{2m_{\mathrm{X}}} - \frac{i}{2\gamma_{\mathrm{U}}} - \frac{i}{2\gamma_{\mathrm{U}}}\frac{(k_x^2+k_y^2)m_-}{\sqrt{(k_x^2+k_y^2)^2m_-^2+16\Omega_{\mathrm{R}}^2}} \end{pmatrix}, \tag{5.17}$$

where we have set $\hbar = 1$ and assumed an infinite lifetime for the excitons and photons in order to highlight the effect on the upper polariton dephasing on the system. The reduced mass $m_- = (m_{\mathrm{C}} - m_{\mathrm{X}})/(m_{\mathrm{C}}m_{\mathrm{X}})$ was also introduced to shorten the size of the expression. One can note that the parabolic dispersions of the bare states are now affected with imaginary terms. For large values of momentum, these terms tend to zero. More interesting, the off-diagonal terms that provide the Rabi coupling are also affected in the same way.

For a better accuracy and complete agreement with the experimental results, the modified Hamiltonian $\tilde{\mathbf{H}}_m$ can also include the lifetime of the photon γ_{C}, of the upper polariton γ_{U} and of the lower polariton γ_{L}. However, we keep neglecting the lifetime of the exciton γ_{X} since its value is about two orders of magnitude larger

than the photon one. Following the same transformation, we obtain:

$$\tilde{\mathbf{H}}_m = \begin{pmatrix} \frac{k_x^2+k_y^2}{2m_C} - i\left(\frac{2\tau_C+\tau_L+\tau_U}{2}\right) - \frac{i}{2}\frac{\tau_L+\tau_U}{\sqrt{1+\left(\frac{2\Omega_R}{2i\tau_C+m_-(k_x^2+k_y^2)}\right)^2}} & \frac{\Omega_R}{2} + \frac{i}{2}\frac{\tau_L-\tau_U}{\sqrt{1+\left(\frac{2i\tau_C+(k_x^2+k_y^2)m_-}{2\Omega_R}\right)^2}} \\ \frac{\Omega_R}{2} + \frac{i}{2}\frac{\tau_L-\tau_U}{\sqrt{1+\left(\frac{2i\tau_C+(k_x^2+k_y^2)m_-}{2\Omega_R}\right)^2}} & \frac{k_x^2+k_y^2}{2m_X} - i\left(\frac{2\tau_C+\tau_L+\tau_U}{2}\right) + \frac{i}{2}\frac{\tau_L+\tau_U}{\sqrt{1+\left(\frac{2\Omega_R}{2i\tau_C+m_-(k_x^2+k_y^2)}\right)^2}} \end{pmatrix}. \tag{5.18}$$

Note that in the previous expression, the different lifetimes are introduced through their respective decay rates: $\tau_j = 1/\gamma_j$.

5.3.2 Vortex dynamics

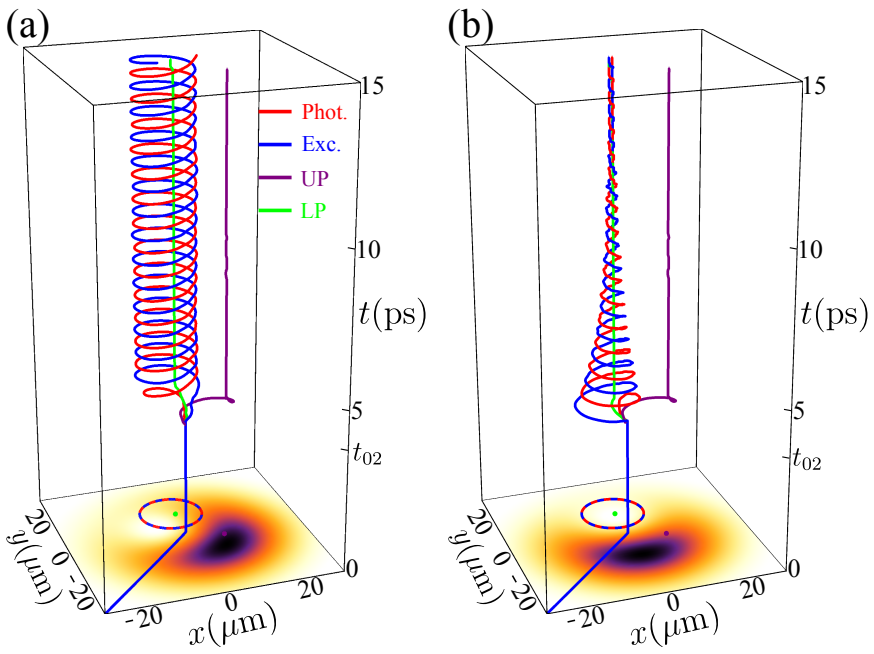

Figure 5.3: Vortex oscillations generated by perturbing the system, that was initially prepared in a vortex state, with a Gaussian pulse sent at $t = t_{02} \approx 4$ ps. The vortex trajectory in the photonic (excitonic) field is plotted in red (blue) and also in the upper (lower) field in purple (green). The wave function intensity $|\psi_C|$ is plotted in the $x-y$ plane for a $t > t_{02}$, where are as well projected the vortex trajectories. (a) Conservative case, without including decay. After the second pulse, the vortices in both fields describe circles with a non constant angular velocity. (b) Adding the upper polariton decay, it results in a damping of the oscillations at the rate of the UP decay.

One can see in Fig. 5.3(a) the basic vortex dynamics obtained from Eq. 5.13. A first Laguerre-Gauss pulse is sent at early time to generate the vortex, and a second Gaussian pulse is sent at $t_{02} \approx 4$ ps. After the first pulse, the vortex is perfectly

centred in the middle of the beam and motionless. After the second pulse, the minimum of intensity no longer remains in the center of the beam, as shown on the density plot, which induces vortex oscillations. The dynamical position of the vortex is shown with a 3D curve for both photonic (in red) and excitonic fields (in blue). The vortices trajectory in space and time looks helical but it is actually not, the angular velocity varying periodically in time. The two vortices, in the photon and in the exciton, rotates around each other at the Rabi frequency a bit like a Newton's cradle, one vortex slowing down while the other accelerates.

In the case of Fig. 5.3(a) the upper polariton lifetime was included by using the modified Hamiltonian $\tilde{\mathbf{H}}_m$ of Eq. 5.17. The vortex precession now follows a spiral whose radius damping corresponds to the UP lifetime, here 4 ps. The vortex in both photonic and excitonic field converges towards the same fixed point.

To understand these vortex motions, it is interesting to look at the vortex behaviours through the eigenstates of the system, namely by looking at the polaritonic fields ψ_+ and ψ_- which are obtained by combining the bare states. The vortex trajectories in the polaritonic fields are plotted with green (lower) and purple (upper) lines in Fig. 5.3. Before the Gaussian pulse, the vortex is located in the center of the beam for all the fields. After the second pulse, we see that unlike in the photon and exciton fields, in which the vortex oscillates, it is simply shifted to the periphery of the beam in the polaritonic fields, without exhibiting any oscillations. In the damped case, we see now clearly that as the upper field is dying, the vortex in the photon/exciton field converges toward the position of the lower one. We know now that the oscillations occur because the vortex of the polaritonic fields are shifted at different position into the beam, the vortex in the photon/exciton components oscillating between them. Yet the vortex oscillations are located close to the vortex position in the LP, possibly due to the mass imbalance between the two fields.

This suggests that the same kind of oscillations could be obtained by simply propagating the Laguerre-Gauss beam. We have seen in Chapter 4 that because of the effective mass imbalance between the polaritonic fields, one can obtain their spatial separation by imparting a momentum to the light beam, both of the subfields (ψ_+ and ψ_-) propagating thus with a different velocity. We will discuss it in details in Section 5.6.

5.4 Orbital Angular Momentum of Polariton Vortices

In this Section, the main definitions of the Orbital Angular Momentum (OAM) and the different applications to the polariton vortex cases are given. We see how the OAM is conserved in a polariton system, and what is the OAM of a superposition of vortex states. The Rabi-Orbit coupling is also investigated.

5.4.1 Definitions and Vortex OAM

In quantum mechanics the OAM is an observable that can be measured from the field's spatial distribution of a light beam. To this observable is associated a Hermitian operator defined as the cross product between the position and the momentum operators:

$$\hat{L} = \hat{r} \times \hat{p}\,, \tag{5.19}$$

with the momentum operator $\hat{p} = -i\hbar\vec{\nabla}$. The OAM operator can thus be written for any component j as:

$$\hat{L}_i = -i\hbar\varepsilon_{ijk}x_j\partial_{x_k}\,, \tag{5.20}$$

in the Einstein notation and using the Levi-Civita symbol ε_{ijk}. The commutation relations for the OAM operator can be as well summarised as:

$$[\hat{L}_i, \hat{L}_j] = \varepsilon_{ijk}i\hbar\hat{L}_k\,. \tag{5.21}$$

We shall make clear that the OAM definition we use here corresponds to the *external* OAM, which is origin-dependent, unlike the *internal* OAM generally associated to the helical wave front of the beam.

In the present case, we are considering wave functions which are 2D functions of x and y. Thus the angular momentum operator will only contain one non-zero component on z :

$$\hat{L}_z = -i\hbar(x\partial_y - y\partial_x)\,. \tag{5.22}$$

The expectation value of $\hat{L}_z$, that we will simply call $\hat{L}$ in the following, over a state ψ is thus expressed by:

$$\langle\hat{L}\rangle_\psi = -i\hbar\,\langle\psi|\hat{L}|\psi\rangle = -i\hbar\int_{-\infty}^{+\infty}\int_{-\infty}^{+\infty}\psi^*(x\partial_y\psi - y\partial_x\psi)\mathrm{d}x\mathrm{d}y\,. \tag{5.23}$$

As is well known, the angular momentum is quantized. The z-component of the angular momentum only assumes one of the discrete set of values $m\hbar$, with $m = \pm 0, \pm 1, ..., \pm l$, where l is the vortex topological charge. In the case of a Gaussian wave packet, the value of $\langle\hat{L}\rangle_\psi$ is simply zero. For a vortex state, like the general one of Eq. 5.6 we have $\langle\hat{L}\rangle_\psi = l\hbar$, since the packet was normalised.

One can also define the OAM per particle by dividing it by the total intensity of the field:

$$\hat{l}_\psi = \frac{\langle\hat{L}\rangle_\psi}{N_\psi}\,, \tag{5.24}$$

where $N_\psi = \int_{-\infty}^{\infty}|\psi|^2\mathrm{d}r$. The angular momentum per particle of a general vortex state (Eq. 5.6) is $\hat{l}_\psi = l\hbar$. As mentioned by Pitaevskii and Stringari [19], in the case of a vortex displaced from the center, $|\hat{l}_\psi|$ takes a lower value, the axial symmetry of the problem being lost.

5.4.2 OAM of a States Superposition

We have seen in the previous Sections that the expectation value of $\hat{L}$ for a simple vortex state was given by an integer number of $\hbar$, depending on the vortex's order. We want now to compute the angular momentum of a linear combination of two wave functions ψ_1 and ψ_2, in order to apply it later to a superposition of two vortices. To do so we have to calculate the expectation value of $\hat{L}$ for a linear combination:

$$\psi_s = \alpha_1 \psi_1 + \alpha_2 \psi_2 \,, \tag{5.25}$$

where the $\alpha_{1,2}$ are complex numbers and $\psi_{1,2}$ are possibly vortex solutions (Eq. 5.8), with their respective masses m_1 and m_2. The expectation value of the OAM for ψ_s thus reads:

$$\begin{aligned}
\langle \hat{L} \rangle_{\psi_s} &= -i\hbar \int_{\mathbb{R}^2} \psi_s^* (x\partial_y \psi_s - y\partial_x \psi_s) \mathrm{d}r \\
&= -i\hbar \int_{\mathbb{R}^2} (\alpha_1^* \psi_1^* + \alpha_2^* \psi_2^*)(x(\alpha_1 \partial_y \psi_1 + \alpha_2 \partial_y \psi_2) - y(\alpha_1 \partial_x \psi_1 + \alpha_2 \partial_x \psi_2)) \mathrm{d}r \\
&= -i\hbar \int_{\mathbb{R}^2} \Big(|\alpha_1|^2 \psi_1^* (x\partial_y \psi_1 - y\partial_x \psi_1) + |\alpha_2|^2 \psi_2^* (x\partial_y \psi_2 - y\partial_x \psi_2) \\
&\qquad + \alpha_1^* \alpha_2 \psi_1^* (x\partial_y \psi_2 - y\partial_x \psi_2) + \alpha_1 \alpha_2^* \psi_2^* (x\partial_y \psi_1 - y\partial_x \psi_1) \Big) \mathrm{d}r \,.
\end{aligned} \tag{5.26}$$

If $\psi_{1,2}$ are vortex solutions, we see that the two first terms of the last integral are the expression of the angular momentum for a single vortex and thus have the value $-|\alpha_{1,2}|^2\hbar$.

The other cross terms of the integral depend on the spatial overlap between the two fields ψ_1 and ψ_2. For instance if these two fields are spatially separated, the value of $\langle \hat{L} \rangle_{\psi_s}$ will be simply the sum of the contribution of the OAM from each field, being thus $-(|\alpha_1|^2 + |\alpha_2|^2)\hbar$.

5.4.3 OAM Conservation

For a polariton system, the total intensity of the fields is conserved through a change of basis:

$$N_{\psi_\mathrm{C}} + N_{\psi_\mathrm{X}} = N_{\psi_\mathrm{U}} + N_{\psi_\mathrm{L}} \,. \tag{5.27}$$

In the same way, such a relation can be found for the conservation of the angular momentum. The sum of the angular momentum of the different fields is conserved as well through the change of basis:

$$\langle \hat{L} \rangle_{\psi_\mathrm{C}} + \langle \hat{L} \rangle_{\psi_\mathrm{X}} = \langle \hat{L} \rangle_{\psi_+} + \langle \hat{L} \rangle_{\psi_-} \,. \tag{5.28}$$

This can be easily demonstrated by writing the photonic and excitonic fields as a sum of polaritonic fields, that are $\psi_\mathrm{X} = (\psi_+ + \psi_-)/\sqrt{2}$ and $\psi_\mathrm{C} = (\psi_+ - \psi_-)/\sqrt{2}$, and by using the result of Eq. 5.26. One also notes that Eq. 5.28 is not valid for the sum of the angular momentum per particle. It is known that in the absence of a torque,

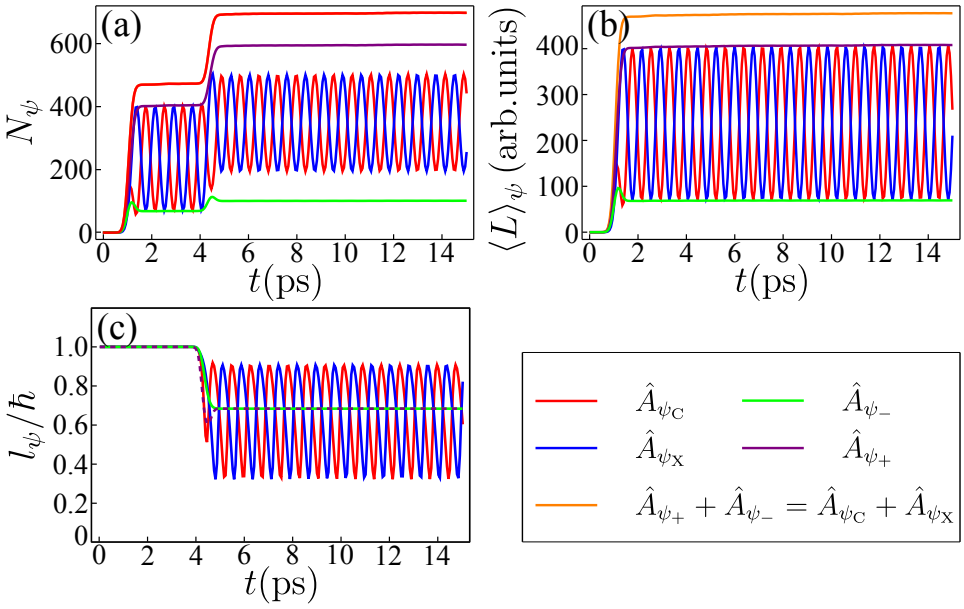

Figure 5.4: Various OAM computed from the two-pulses experiment simulation data, corresponding to the case of Fig. 5.3(a). (a) Fields intensities. (b) Angular Momentum for the different fields. (c) Angular momentum per particle, normalised in units of $\hbar$. See the legend on the right bottom corner for the color code of the operators $\hat{A}(\langle L \rangle, N \text{ or } l)$ applied to the corresponding field. The conserved quantity are plotted in orange.

the angular momentum is constant. However, for the polaritons, the OAM is conserved through the sum of the OAM of each sub-fields (photon/exciton), which allows the OAM of the individual fields to vary. In any case $d(\langle \hat{L} \rangle_{\psi_C} + \langle \hat{L} \rangle_{\psi_X})/dt$ has to be constant. In order to illustrate these conservation rules, we have computed the different OAM for the conservative case of the oscillating vortex created with two pulses (see Fig. 5.3(a)). One can see in Fig. 5.4(a) the time evolution of the fields intensities N_ψ. The bare fields ψ_C and ψ_X exhibit Rabi oscillations while the polaritonic fields ψ_+ and ψ_- do not. The different intensities of course increase after the second pulse arrival, the system being filled with more particles. The conserved quantities of Eq. 5.27 are plotted in orange. The OAM (see Eq. 5.23) is plotted in (b) for the different fields. One can see that the OAM of the bare fields oscillates exactly between the OAM's steady value of the polaritonic fields. This result is intriguing because the OAM of the different fields does not seem to be affected by the second pulse, that initiates the vortex oscillations process. The conserved quantities of Eq. 5.28 are also plotted in orange. We can get more insight by looking at the OAM per particle, as plotted in (c). When the vortices in the different fields are exactly in the center of the beam, that is before the second pulse, the angular momentum per particle is exactly quantized to one unit of $\hbar$. After the second pulse, the vortices in the polaritons do not oscillate but are displaced to a fixed position on the periphery of the beam (see purple and green lines in Fig. 5.3), and as we said before, the corresponding value of l is less than 1.

As the polaritonic vortices are symmetrically displaced into the beam, l_{ψ_+} and l_{ψ_-} share the same value. In the photonic and excitonic fields, the vortices oscillate from the center to the periphery in circle, so that variation range of the oscillations of the OAM per particle is constant.

5.4.4 Rabi Orbit Coupling

In a polariton fluid, as we have seen before, the vortex motion is intrinsically powered by the Rabi oscillations. We attempt here to find the physical and mathematical reason of this *Rabi-Orbit Coupling* at the origin of the vortex oscillations. To do so, we look for the variation of the OAM in order to see how the angular momentum operator is related to the Rabi coupling.

We first start by computing the time derivative of the expectation value of $\hat{L}$:

$$\begin{aligned}\partial_t \langle\psi|\hat{L}|\psi\rangle =&(\partial_t \langle\psi|)\hat{L}|\psi\rangle + \langle\psi|\hat{L}(\partial_t|\psi\rangle)\\ =&\frac{i}{\hbar 2m}\langle\psi|\hat{p}^2\hat{L}|\psi\rangle - \frac{i}{\hbar 2m}\langle\psi|\hat{L}\hat{p}^2|\psi\rangle\\ =&\frac{i}{\hbar 2m}\langle\psi|[\hat{p}^2,\hat{L}]|\psi\rangle\,.\end{aligned} \tag{5.29}$$

It is known that the value of the commutator in the previous equation is $[\hat{L}_z,\hat{p}^2]=0$, which is expected for a single isolated field ψ, and arises from the conservation of the *OAM*.

This result should be however different in the case of a coupled system like the polaritons. So let us now substitute the time derivative $\partial_t|\psi\rangle$ in Eq. 5.29 by its solution form the coupled Schrödinger Equation. For the photonic field, it reads:

$$\partial_t \psi_C = -\frac{i}{\hbar 2m_C}\hat{p}^2\psi_C - \frac{i\Omega_R}{2}\psi_X\,. \tag{5.30}$$

We can now introduced the previous solution into the Eq. 5.29 :

$$\begin{aligned}\partial_t\langle\hat{L}\rangle_{\psi_C} =& \int_{\mathbb{R}^2}\frac{i}{\hbar 2m_C}\langle\psi_C|[\hat{p}^2,\hat{L}]|\psi_C\rangle + \frac{i\Omega_R}{2}\left(\langle\psi_X|\hat{L}|\psi_C\rangle - \langle\psi_C|\hat{L}|\psi_X\rangle\right)\mathrm{d}r\\ =&\int_{\mathbb{R}^2} -\Omega_R\mathrm{Im}(\langle\psi_C|\hat{L}|\psi_X\rangle)\mathrm{d}r\,.\end{aligned} \tag{5.31}$$

We see from the previous equation how the Rabi coupling couples as well with the angular momentum of each field, which depends explicitly on the spatial overlap between the two wave functions. This coupling will be ineffective if the two wave functions are spatially separated, cancelling the OAM variations.

The term $\langle\psi_C|\hat{L}|\psi_X\rangle$ can be as well differentiated in time :

$$\begin{aligned}&\partial_t\langle\psi_C|\hat{L}|\psi_X\rangle =\\ &\int_{\mathbb{R}^2}\frac{i}{2\hbar m_C}\langle\psi_C|\hat{p}^2\hat{L}|\psi_X\rangle - \frac{i}{2\hbar m_X}\langle\psi_C|\hat{L}\hat{p}^2|\psi_X\rangle + \frac{\Omega_R}{2\hbar}\left(\langle\hat{L}\rangle_{\psi_C} - \langle\hat{L}\rangle_{\psi_X}\right)\mathrm{d}r\,.\end{aligned} \tag{5.32}$$

We see again through the last term of Eq. 5.32 the coupling between Rabi and the OAM of the different fields. Nonetheless, new crossed terms are obtained and can also be differentiated, going deeper in the order of operators correlation:

$$\partial_t \langle \psi_C | \hat{p}^2 \hat{L} | \psi_X \rangle = \int_{\mathbb{R}^2} \frac{i}{2\hbar m_C} \langle \psi_C | \hat{p}^4 \hat{L} | \psi_X \rangle - \frac{i}{2\hbar m_X} \langle \psi_C | \hat{p}^2 \hat{L} \hat{p}^2 | \psi_X \rangle + \frac{\Omega_R}{2\hbar} \left(\langle p^2 \hat{L} \rangle_{\psi_C} - \langle p^2 \hat{L} \rangle_{\psi_X} \right) \mathrm{d}r, \tag{5.33}$$

and

$$\partial_t \langle \psi_C | \hat{L} \hat{p}^2 | \psi_X \rangle = \int_{\mathbb{R}^2} \frac{i}{2\hbar m_C} \langle \psi_C | \hat{p}^2 \hat{L} \hat{p}^2 | \psi_X \rangle - \frac{i}{2\hbar m_X} \langle \psi_C | \hat{p}^4 \hat{L} | \psi_X \rangle + \frac{\Omega_R}{2\hbar} \left(\langle \hat{L} p^2 \rangle_{\psi_C} - \langle \hat{L} p^2 \rangle_{\psi_X} \right) \mathrm{d}r. \tag{5.34}$$

Differentiating the new cross terms in Eqs. 5.33 and 5.34 would not close this system of Equations. A truncation at an arbitrary order is thus necessary to close it, which would require further studies.

For our purpose, it is however enough to demonstrate that the Rabi-Orbit Coupling is at the origin of the vortex motion. This claim can also be supported from the numerical simulations we have done. In Section 5.3, we have seen how the UP lifetime damps as well the vortex oscillations, indeed, by removing one the polaritonic field (ψ_- in this case), one cancels as well the Rabi oscillations. We will see in Section 5.3, that the Rabi oscillations can also be suppressed by obtaining a spatial separation of the polariton fields, providing a momentum to the beam, for instance. Without overlap between the polaritons, no Rabi oscillations occur, and neither do vortex oscillations.

5.5 Two-Pulse Experiments

In this Section are presented some experimental results obtained by my colleagues of Lecce. This two-pulse experiment, which corresponds to the cases we have already described in Section 5.3, was the first initially performed. It demonstrates the generation of vortex oscillations by disturbing it with a Gaussian pulse.

The impact of the decay sources is discussed, based on the numerical simulations we have realised. We also discuss the different hypothesis on the nature of the vortex oscillations from a theoretical point of view and propose an analytical solution for the shifted vortex.

5.5.1 Experimental Results

The experimental setup used for this experiment is very similar to the one of the previous experiments that we have discussed in this manuscript, and it is based on the same microcavity sample. So we will not enter into further details here, one can refer instead to Section 2.4.1 of Chapter 2.

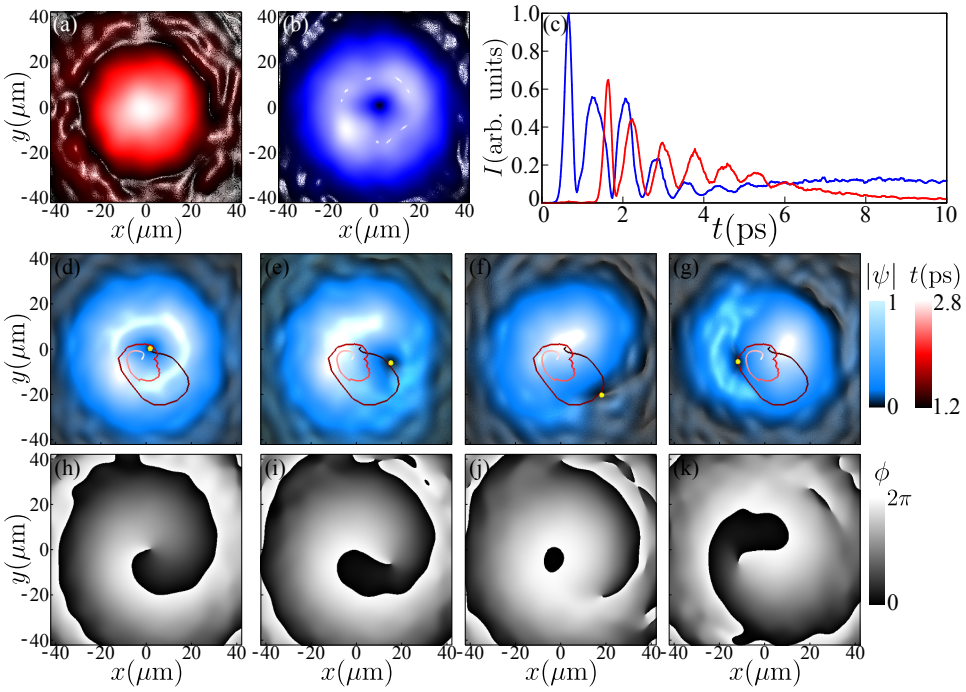

Figure 5.5: Polariton vortex oscillations. (a,b) Space charts of $|\psi|^2$ after the first Gaussian pulse (a) and after the second Laguerre-Gauss pulse (b). (c) Local density oscillations in the ring annulus and centre after the two pulses. The vortex oscillation over a time span of two Rabi periods (t = 1.2 – 2.8 ps) is displayed for four space charts taken at t = 1.2, 1.5, 1.58, 1.72 ps, in intensity (d-g) and phase (h-k). The phase singularity is marked with a yellow dot which follows the red trajectories in this time range.

The experimental configuration is otherwise the following: a first Laguerre-Gauss pulse (see Eq. 5.11) with a 30 µm FWHM is sent to the cavity at t = 1.20 ps, with a spread in energy large enough to probe both polariton branches, triggering the Rabi oscillations. This beam imprints the phase singularity that creates the vortex. Shortly after, at t = 1.50 ps, a second Gaussian pulse arrives (see Eq. 5.12) breaking the initial symmetry of the density by displacing the vortex on the periphery of the beam. The pulses space profiles are shown in Fig. 5.5(a,b).

The direction of the initial displacement is set by the relative phase θ between the two pulses. The second Gaussian pulse indeed presents a central top intensity with an homogeneous phase. They will be coherently added the ones of the polaritonic vortex field, shifting the vortex core to a new intensity minimum along the vortex line. A more interesting consequence is the generation of a rotating motion of the vortex core, which can be seen in Fig. 5.5. The oscillation of the vortex core over two Rabi period is clearly observed (d,g, yellow dot), and follows the corresponding red path. The vortex describes a spiral with a period roughly equal to the Rabi perdiod $\tau_R \approx 0.8$ ps and with a radius damping corresponding to the UP lifetime $\tau_{UP} \approx 0.2$ ps. The theoretical results that we have obtained (see Fig. 5.3) are thus in good agreement with the experimental observations.

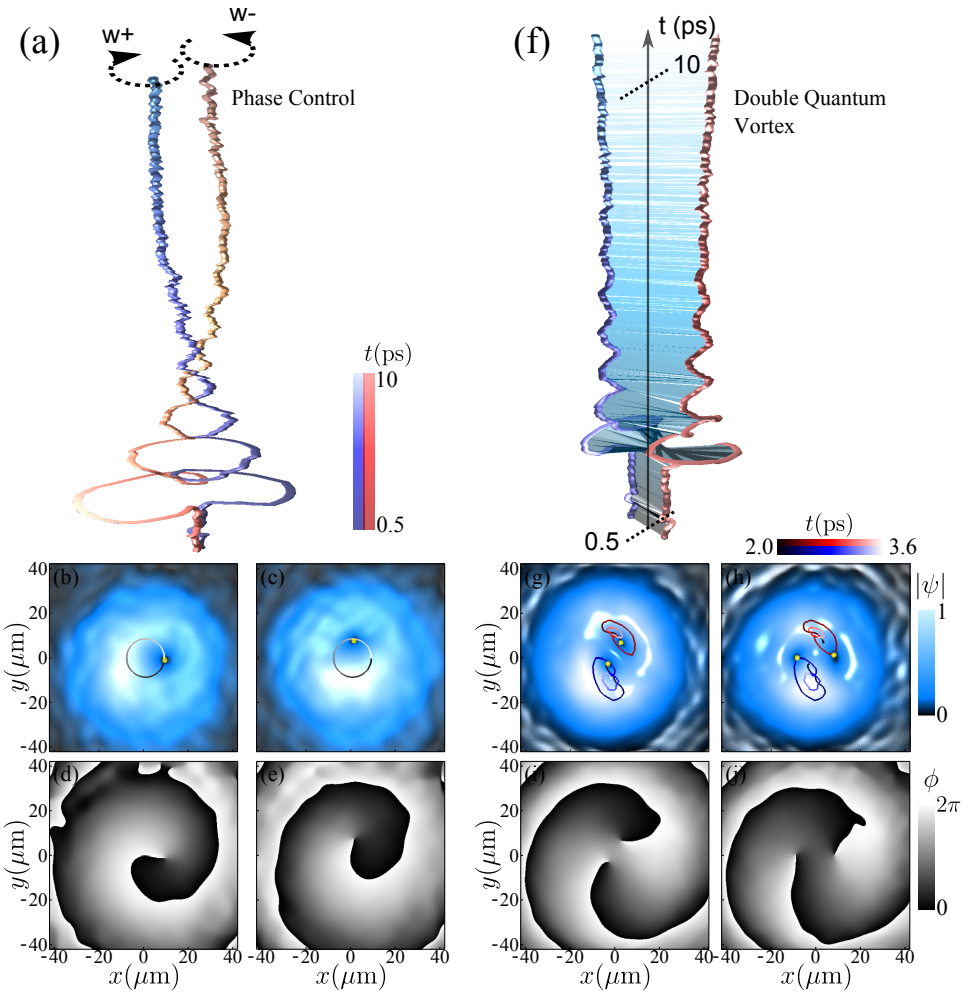

Figure 5.6: (a-e) Vortex oscillations phase control. Vortex trajectories are shown for $l = \pm 1$ winding initial vortex states. It results in opposite spiralling. The space charts show the amplitude and the phase wave function at $t = 2.6$ ps, for different phase delay between the pulse, of $\pi/2$ here. (f-j) Spiralling of a double quantum vortex. The vortex lines are plotted from 0.5 to 10 ps. The space charts are taken at $t = 2$ and 2.56 ps, where the vortex trajectories are reported in solid lines (blue and red).

This experiment was also performed with opposite winding number $l = +1$ and $l = -1$, see Fig. 5.6 (a-e). Starting with an opposite winding number results in the spiraling of the vortex in the other direction, suggesting that the phase does not only respond to the initial displacement of the vortex. A coherent control of the vortex trajectory could thus be obtained by tuning the phase delay between the two pulses ϕ.

The photonic pulse can also be shaped to carry two topological charges by the use of different q-plates. The two vortices are symmetrically split (over ≈ 10 μm) into the beam after the second pulse arrival. Such a dynamics is reported in Fig. 5.6

(f-j). Each vortex oscillates in spiral, whose radius decay with the upper polariton lifetime, reaching a new equilibrium position.

5.5.2 Analytical Model

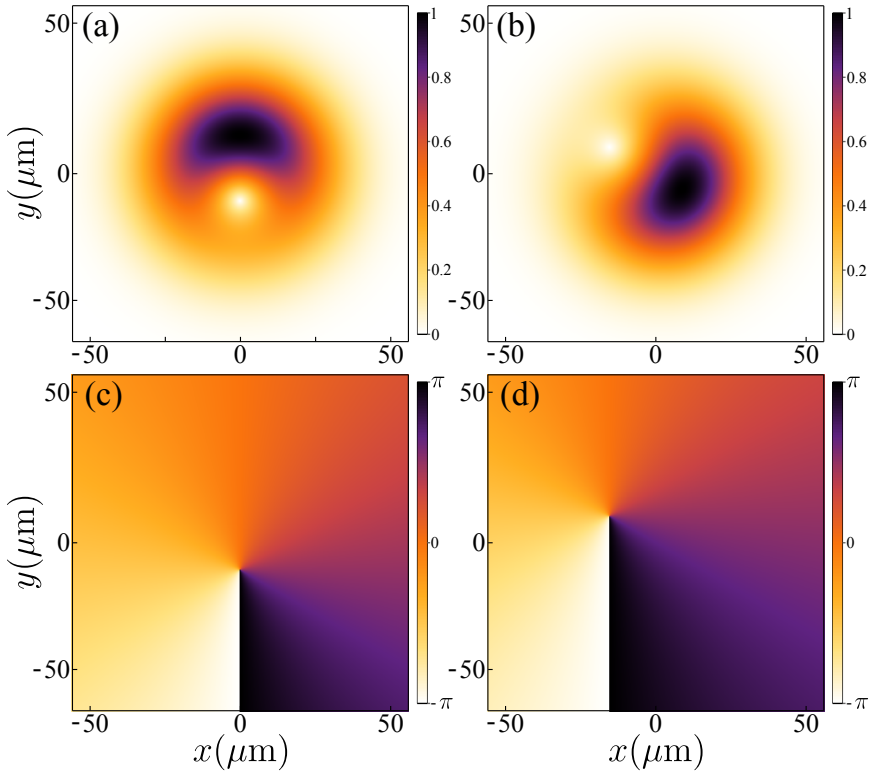

Figure 5.7: Intensity (upper row) and phase (lower row) for the analytical vortex solution ψ^{Gv}, see Eq. 5.35. Parameters : $\alpha = 100$ and $\theta = 0$ (a-c). $alpha = 50$ and $\theta = 2\pi/3$ for (b-d).

Following an intuitive approach, we can now try to find an analytical expression for the shifted vortex. Let us consider the two pulses experiment viewed from the polaritonic fields, *i.e.* a polariton described by a single field that does not Rabi oscillate. The vortex initially located in the center of a Laguerre-Gauss beam is shifted to a new position on the periphery of the beam after the sent of a Gaussian pulse, breaking in the same time the homogeneity of the density. We can construct a such a vortex solution by simply considering a superposition of a vortex solution of the 2DSE (see Eq. 5.7) with a Gaussian solution of the 2DSE (That can be obtained easily with the same procedure as Eq. 5.7). The final solution reads :

$$\begin{aligned}\psi^{Gv} &= \psi^{v} + \frac{e^{i\theta}}{\alpha}\psi^{G} \\ &= \frac{i\sigma_R^2(y+ix)}{\sqrt{\pi}(\sigma_R^2+\frac{i\hbar t}{m})^2} e^{-\frac{(x^2+y^2)}{2\sigma_R^2+\frac{2i\hbar t}{m}}} + \frac{e^{i\theta}}{\alpha}\frac{\sigma_R^2}{\sigma_R^2+\frac{i\hbar t}{m}} e^{-\frac{(x^2+y^2)}{2\sigma_R^2+\frac{2i\hbar t}{m}}}.\end{aligned} \tag{5.35}$$

where ψ^v is the vortex solution from Eq. 5.7 and ψ^G is the solution for the Gaussian wave packet, with m the mass of the desired polariton and θ the optical phase between the two pulses. The two wave functions are weighted with the coefficient α, which controls the ratio of the pulses intensities. We assume that the two beams have the same spatial extension σ_R.

Thus, the OAM per particle for such a solution reads:

$$\hat{l}_{\psi^{Gv}} = \frac{\langle \hat{L} \rangle_{\psi^{Gv}}}{N_{\psi^{Gv}}} = \hbar \frac{\alpha^2}{\alpha^2 + \pi\sigma_R^2}, \tag{5.36}$$

where $N_{\psi^{Gv}}$ is the density of the total beam $\int_{-\infty}^{+\infty} \psi^{Gv} \mathrm{d}r$. The distance of the vortex from the center into the new beam is controlled by the value of the coefficient α. The bigger it is, the closest is the vortex from the center of the beam. From Eq. 5.36 we see that the value of $\hat{l}_{\psi^{Gv}}$ tends to $\hbar$ when α tends to infinity, *i.e.* when then beam is purely Laguerre-Gauss. The optical phase θ set the angle of the phase singularity, but it does not affect the value of the OAM per particle.

Two examples of the wave function in Eq. 5.35 are plotted in Fig. 5.7. In (a-c), the parameter α is set to 100 and the optical phase θ to zero, displacing slightly the vortex from the center of the beam. In (b-d), with $\alpha = 50$ and $\theta = 2\pi/3$ the vortex is moved more in the periphery of the beam and with a particular angle.

5.6 Propagating vortices

In this Section we consider cases of a propagating Rabi oscillating vortex. We have seen in Chapter 4 how the polaritons separate spatially while they propagate, due to their mass imbalance. As the photon/exciton fields are actually a superpostion of polariton fields, such a case would lead as well to the splitting of the vortices in polaritonic fields. Furthermore we have seen in Section 5.3 that a separation of the polaritonic vortices combined with the Rabi oscillations induce vortex oscillations. Such a case was first investigated theoretically and we detail here the different solutions we have developed for it. From these predictions, the corresponding experiment was performed in Lecce and a very interesting dynamics was observed.

5.6.1 Moving Rabi Vortices Model

To generate vortex oscillations, we considered previously the excitation of the system via two pulses, the second one being a Gaussian that alters the beam's density. The vortices in the polaritons were thus shifted symmetrically out of the center of the beam, *cf.* Fig. 5.3. This phenomenon combined to the Rabi oscillations was leading to precession of the vortex cores in the bare fields. Such a splitting of the vortex cores in the polaritonic fields can actually be achieved in a simpler way, by imparting a momentum to a single Laguerre-Gauss beam. We have seen in Chapter 4 that because of the peculiar polariton dispersion, the UP and LP have a different effective mass $m_1(k)$ and thus propagate with a different velocity if the

same momentum is imparted to them. It is thus easy to construct the solution for the photonic and excitonic fields, by combining the polaritonic fields :

$$\psi_{\mathrm{C}}^{v} = Eg_1\psi_{+}^{v} - Eg_2\psi_{-}^{v}e^{i\Omega_{\mathrm{R}}t}\,, \tag{5.37a}$$

$$\psi_{\mathrm{X}}^{v} = Eg_1\psi_{-}^{v}e^{i\Omega_{\mathrm{R}}t} + Eg_2\psi_{+}^{v}\,. \tag{5.37b}$$

The fields ψ_{+}^{v} and ψ_{-}^{v} are the vortex solutions of the Schrödinger Equation we have derived before, see Eq. 5.8. We can thus use here a parabolic approximation, since the solution for the fields was derived from the uncoupled single SE. The Rabi oscillations can be re-created by splitting the two branches in energy, that's why the term $e^{i\Omega_{\mathrm{R}}t}$ was added. The fields are properly weighted with the Hopfield coefficient given by $(Eg_1, Eg_2)^{\mathrm{T}}$, that is an eigenvector of the Hamiltonian $\mathbf{H}$. The mass parameter of each field can be simply set with the polariton dispersion as:

$$m_{\pm} = \frac{\hbar^2 k}{\partial_k E_{\pm}}\Big|_{k=k_{0x}}\,. \tag{5.38}$$

We have plotted in Fig. 5.8 the wave functions obtained with Eqs. 5.37. In this

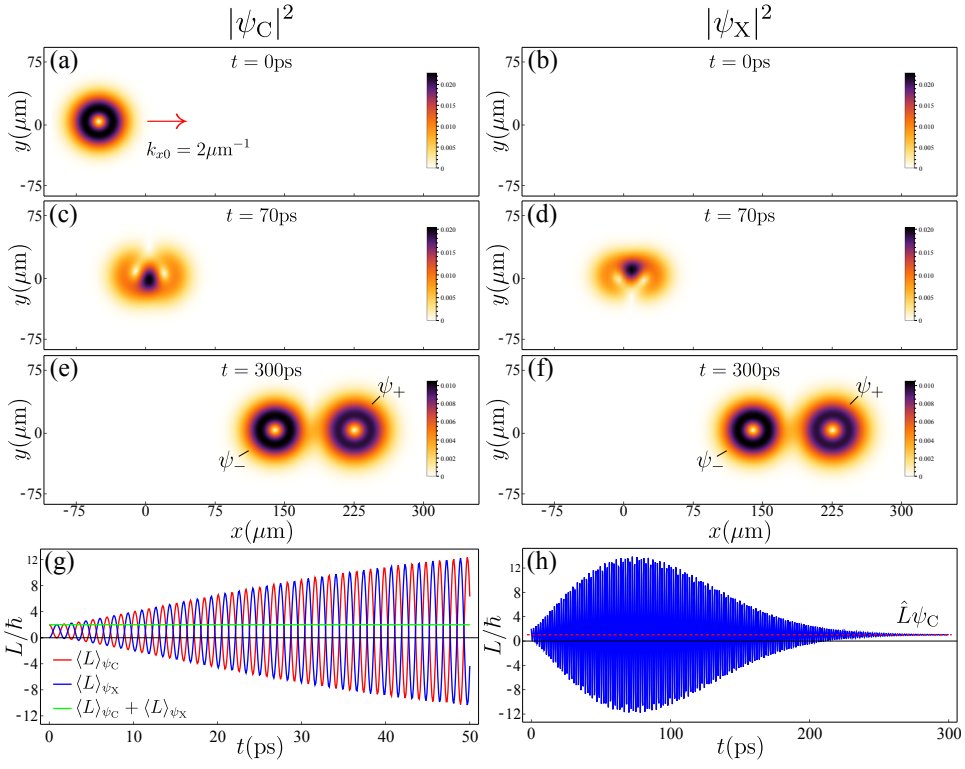

Figure 5.8: Photonic field $|\psi_{\mathrm{C}}|^2$ (a,c,e) and excitonic field intensities $|\psi_{\mathrm{X}}|^2$ (b,d,f) at different times. (g) OAM expectation value of the different fields, photonic in red, and excitonic in blue, as function of time. The conserved sum is plotted in green. (h) OAM for the photonic field only, at computed at larger time. It evolves with the sptatial overlap between the polaritons.

case, the Laguerre-Gauss beam sent in the photon is imparted with a momentum

$k_{x0} = 2\ \mu\text{m}^{-1}$. This results in a moving vortex along the x-axis that Rabi oscillates. The radius of the vortex oscillations slowly increases as the beam propagates. As the UP and LP fields start to split, we see the appearance of an other oscillating vortex core. As shown in Fig. 5.8(c-d) at $t = 70$ ps, the beam contains two contra-rotating vortices. The same dynamics is observed in the exciton, but in this field the vortices are oscillating in opposite directions, with respect to the ones in the photonic field. After a long propagation time, the two polaritons are fully spatially separated, as seen in Fig. 5.8(e-f) at $t = 300$ ps. As there is no more overlap between them at this time, the system does not exhibit Rabi oscillations any more.

We have of course not included the different decay rates and dephasing of the polaritons in order to see the full dynamics. Such a picture would be impossible to obtain with the current microcavity polariton technology. It is however useful to have it to understand the full dynamics. An interesting result arises from looking at the OAM in this case. We have computed the expectation value of the OAM $\langle \hat{L} \rangle_\psi$ and plotted it in Fig. 5.8(g) at early times. Similarly to the two-pulse case, we see an oscillation of the OAM for the photonic and excitonic fields, but more surprisingly, this time the value of $\langle \hat{L} \rangle_\psi$ is increasing with time. The OAM can be increased here by one order of magnitude, with respect to the initial value that depends on the beam's density. The OAM is however still conserved globally through the sum of $\langle \hat{L} \rangle_{\psi_C}$ and $\langle \hat{L} \rangle_{\psi_X}$ (green curve).

This result is surprising but not illogical since the UP and LP are slowing splitting in space, increasing in the same time the radius and the velocity of the vortex oscillations. The value of the OAM is expected to decrease as the UP and LP are separated, limiting the effect of the Rabi oscillations. This is what we see in (h), where the OAM was computed for a larger timescale. At large times, the OAM value converges to a single value, half of $\langle \hat{L} \rangle_{\psi_C} + \langle \hat{L} \rangle_{\psi_X}$. We have seen in Section 5.4.2 that in the absence of overlap between the two wave function (UP and LP here), the expectation value of $\langle \hat{L} \rangle_\psi$ reduces to the sum of the expectation values of the sub-fields, which is steady and does not oscillate. The vortex solution for the photonic/exciton fields in Eq. 5.37 are in very good agreement with the corresponding numerical solutions of the c-2DSE.

5.6.2 Experimental demonstration

Based on the previous theoretical predictions, Rabi oscillating and propagating vortices were achieved experimentally in Lecce. The microcavity sample has been this time excited with a single Laguerre-Gauss shaped beam. The beam has been sent with an oblique incidence in order to reach a central plane wave vector of $k_{x0} = 1.9\ \mu\text{m}^{-1}$, which corresponds roughly to the inflection point of the LPB. The observed vortex dynamics is reported in Fig. 5.9. The space time charts of the left column show snapshots of the wave function intensity in a very short time range, from $t = 1.80$ ps to $t = 1.96$ ps with 0.04 ps steps between the frames. The initial vortex core is suddenly shifted to the beam's periphery. A second vortex core appears shortly after. Both of the contra-rotating vortices are clearly visible on the (c,e,g)

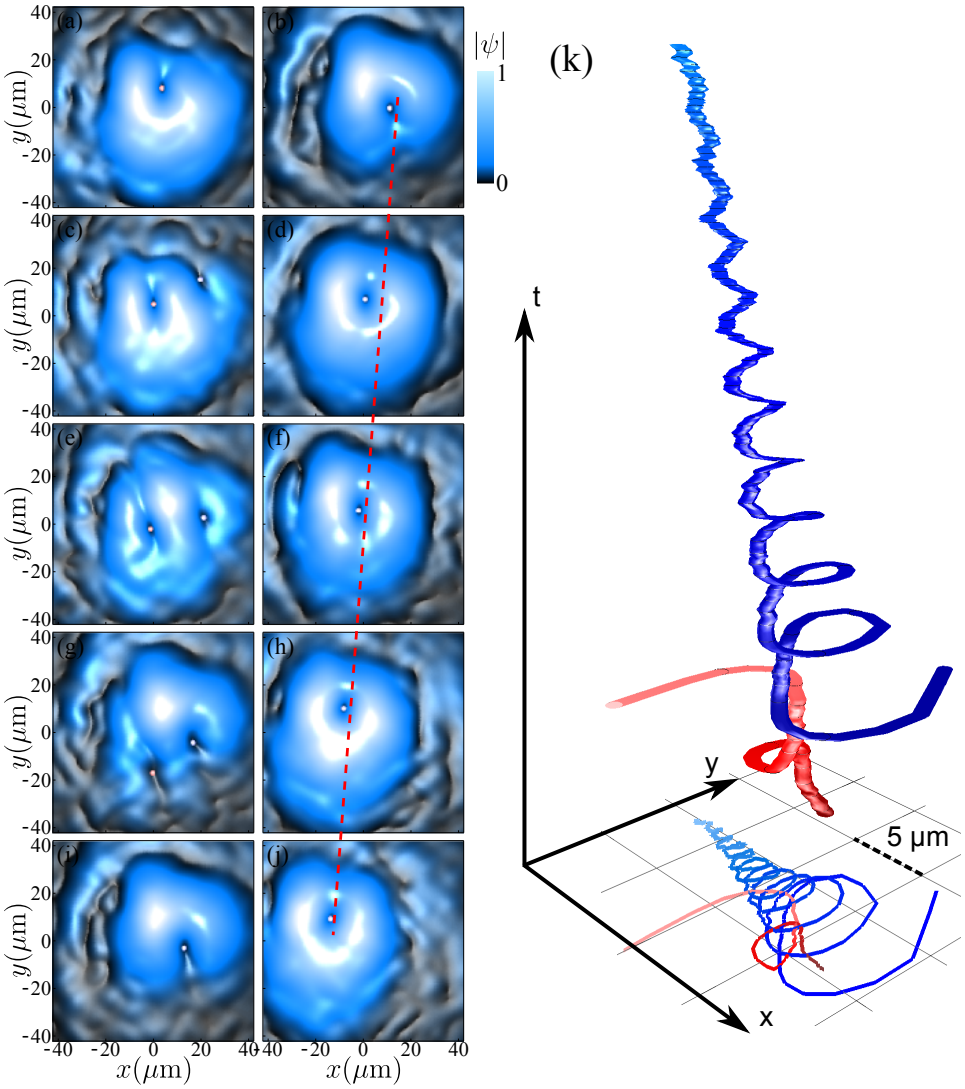

Figure 5.9: Experimental Propagating Rabi vortex. The space time charts show the wave function intensity at different time. The frames on the left column (a,c,e,g,i) are taken from t = 1.80 ps to t = 1.96 ps by steps of 0.04 ps showing the oscillations of the two polaritonic vortices, upper and lower. The frames on the right column (b,d,f,h,j) are taken from t = 2 ps to t = 10 ps by steps of 2 ps showing the overall propagation of the main vortex core, propagating with the measured velocity v = 1.37 µm ps^{-1}. (k) The full vortex trajectories are displayed with 3D strings. The upper (lower) polariton vortex is plotted in red (blue).

panels. At this time, the UP density is still large enough to allow two Rabi cycles, before it dephases completely. This is the first observation of a vortex pair being in two different polariton quantum state. On the second column is represented the wave packet overall dynamics, where the frame are taken from t = 2 ps to t = 10 ps with 2 ps intervals. The whole packet shows a 8.5 µm displacement for 8 ps, which give an average velocity $v \approx 1.05$ µm ps^{-1}. This value is in good agreement with

the expected one, that is determined from the LPB to be $v = 1.08\ \mu\text{m ps}^{-1}$. At early times, the packet might be deformed by the overlapping and faster propagation of the UP, but due to its very short lifetime, the packet is essentially in a LP state after a couple of picoseconds. The remaining vortex motion is thus a combination of linear translation, in the direction of propagation, and a damped Rabi rotation. The trajectory of both vortices can be see in Fig. 5.9(k). The short-living UP vortex (in red) shows two Rabi oscillation barely accomplished, while the long living LP vortex (in blue) shows a similar dynamics than the one obtained in the two-pulse experiment. The projection of these trajectories on the $x-y$ plane are also plotted. The vortex trajectories string were fully reconstructed by measuring the vortices positions with $\delta_t = 0.02$ ps steps.

This first proof shows the complex vortex dynamics that arise from this kind of system. By feeding it with one vortex core in the photonic component, two vortices are actually created in the polaritons fields, sharing the initial OAM provided. The whole oscillation process detected experimentally being simply a consequence of the complex interferences between the two polaritoni fields.

5.7 Conclusions

We have seen in this Chapter the interesting dynamics that arises from the vortices in Polariton fluids. The composite structure of the polaritons allows a vortex core to precess in the beam if their polaritonic vortex components are spatially separated. A perturbation approach can be used, by sending a Gaussian pulse on an initially prepared Laguerre-Gauss beam, that imprints the vortex phase to the polaritons. Another method consists in taking advantage of the effective mass imbalance between the UP and LP, that propagate with a different velocity for a given imparted momentum. In both cases, the vortices of the polaritons are spatially separated, and the vortices in the bare fields oscillate between them.

In Section 5.2, we first have derived the analytical solutions of the Schrödinger Equation for a general vortex state. The solutions can include any winding number or momentum. These vortex solutions share the diffusion properties of a standard Gaussian wave packet, but also get a particular phase profile, with a line singularity that swirls in time; examples are given in Fig. 5.2. These results were extended in Section 5.3 to the more realistic case of a polariton system, described by a set of c-2DSE, excited through two pulses. This system can be exactly solved for any linear Hamiltonian $\mathbf{H}$, see Eq. 5.13. We have thus developed a modified Hamiltonian $\tilde{\mathbf{H}}_m$ that includes all of the relevant decay sources, the UP life time being the most important. From this, we have obtained the full dynamics of a Rabi oscillating polariton vortex, see Fig. 5.3, from which we understood that the vortex motion in the photonic field (that is detected experimentally) depends actually on the fixed position of the vortices in the polaritonic components. The UP lifetime was identified to be the source of the damping of the radius oscillations.

In Section 5.4 we discussed the polariton vortex OAM. We have seen the case

for the OAM of a superposition of states. In the case of superposition of vortex states, the resulting OAM is found to be the sum of the independent OAM contribution (from each sub-vortex) to which is added a contribution depending on the overlap between the two sub-wavefunctions. The OAM for the two-pulses case was computed, corroborating the previous results, see Fig. 5.4. The subtle link between the Rabi coupling and the OAM has been investigated by looking at the torque of the system. It appears that variation of the OAM are directly given by the coupling between the Rabi and the OAM, through *Rabi-Orbit Coupling* terms. Further investigations should go in this direction, since this mechanism appears to be fundamental for the comprehension of the vortex dynamics.

Experimental results of the two pulses experiments are presented in Section 5.5. These results are seen to be in good qualitative agreement with the numerical simulations we have done. A coherent control on the vortex string and experiment involving two vortices have also been performed. We have proposed a simple model to describe the case of a non-oscillating displaced vortex, see Eq. 5.35, whose OAM per particle $\hat{l}$ is found to be less than 1 if the vortex is not centred.

In Section 5.6, we have proposed similar vortex oscillations by imparting a momentum to the Laguerre-Gauss beam. Because of the polariton effective mass imbalance, the UP and LP spatially separate while propagating, leading to a vortex core precession in the photonic (and excitonic) field. In a conservative case, both vortices in the UP and LP can be observed and contra-rotate, see Fig. 5.8, until the complete separation of the polaritons. Without spatial overlap between the wave functions, Rabi oscillations are cancelled, and the vortices oscillations as well. While the polaritons are splitting at early times, the OAM is found to increase by one order of magnitude in the photonic and the excitonic component, the OAM being conserved only through their sum. The OAM then converges towards a steady value when the polaritons do not share overlap any more.

This behaviour has been observed experimentally, where a single Laguerre-pulse was sent that carried a momentum. Both of the polariton vortices were clearly observed, see Fig. 5.9, in the first picoseconds of propagation, the UP one dying then quickly due to its larger lifetime and dephasing. The later dynamics is then governed by the remaining LP component of the beam. These facts confirm some of our hypothesis, such as the actual presence of two vortices (in UP and LP) that can be seen independently for the first time.

These results are very promising since the number of works on the vortices in quantum fluids is huge, and such a vortex dynamics, arising from the superposition of vortex states in polaritons, has not been observed in analogue systems so far, although synthetic gauge fields in cold-atom systems are going in this direction. Apart from the fundamental physical interest, these vortices could find applications in information processing (we have mentioned examples with multiplexing). They could also be used as sensitive polariton gyroscope since they present a macroscopic and easily detectable response to small perturbations.

Chapter 6

Summary and Conclusions

English

In this thesis, I have presented the results of my Research effort during the years 2013-2016 under the supervision of Fabrice P. Laussy as part of the ERC Starting Grant POLAFLOW, which called for a tight collaboration with the experimental group of Daniele Sanvitto in Lecce (Italy). My field of study was the dynamics of microcavity polaritons, superpositions of light and matter in semiconductor heterostructures. These systems can be excited by short pulses of light, that create wavepackets of polaritons, whose subsequent dynamics can be tracked in time thanks to the continuous escape of photons from the cavity (polaritons have a very short lifetime). I have focused on the linear dynamics of these objects where nonlinearities that arise from particle-particle interactions or from a reservoir of excitons can be neglected or absorbed as effective parameters. This poses the problem as the dynamics of two-coupled Bosonic fields, with, in the case of polaritons, largely differing masses that result in a peculiar dispersion relation.

My first input has been to provide a quantitative description of the linear polariton dynamics, in particular their Rabi oscillations. The phenomenon appears simple enough on qualitative grounds but it was not known up to which level of accuracy one could actually account for the observations. The experimentalists in Lecce coud image with a very high precision (hundreds of femtoseconds) the space-time dynamics of the cavity field following short pulse excitations. I have developed a quantum-optical model to describe the order parameters of both the cavity and exciton field, and obtained an essentially perfect agreement between the model and the data. This shows that even though this takes place in a complex solid state system, the Rabi dynamics of polaritons is of an essentially fundamental character, once the problem variables to describe it are understood and accounted for. These are, beside the obvious Rabi coupling between the modes, and their lifetime, also a pure-dephasing term for the upper polaritons and an incoherent pumping rate for the exciton fraction. The former is a well-known attribute of polaritons (the upper branch is much less visible than the lower one) and the later is expected on

phenomenological grounds. My fit to the data allowed to show that these "complications" or "specificities" are enough to account for all that happens in the linear regime. This also allowed to quantify the decay rates for each of these channels, to demonstrate the effect of lifetime-enhancement of the Rabi oscillations thanks to reservoir replenishment and to explain the loss of oscillation contrast by an evaporation of the upper polaritons rather than a loss of strong-coupling. An other clarification made by the theory is that the polariton dynamics under pulse excitation is really that of two-coupled condensates, rather than a quantum superposition of light and matter (what a polariton is in the one-particle limit, that is conceptually largely invoked in the community, although probably still never achieved in the laboratory to date). This brought me to clarify that polaritons are still "cebits" (classical effective two-level systems) rather than "qubits". Finally, the fit revealed that the exciting laser actually couples to both the exciton and photon fields, rather than to the cavity alone, as is universally assumed in the community.

Such a deep understanding and control of the polariton dynamics allows for its coherent control. The theory can achieve any sequence of patterns, amplifying the oscillations, switching Rabi oscillation on and off, transferring the condensates from one branch to the other and even annihilating completely the particles by destructive interferences between the exciting laser and the polarion fields. Strikingly, essentially all these operations have indeed been implemented in the laboratory. This allowed to add another degree of freedom, namely, polarization, to implement the simple but insightful idea that combining Rabi oscillations of two polarized fields leads to oscillations of the polarization. Here, the finite lifetime of the upper polariton could be used as an asset rather than a limitation, to obtain, beside mere oscillations of the polarization, also a drift on the Poincaré sphere. With a judicious choice of parameters, I have shown how this allows to implement a so-called Full Poincaré-beam in time, i.e., light that takes all the states of polarization during the duration of each pulse. Such light brings together two previously unconnected concepts: Full Poincaré beams, that take all the states of polarization in the spatial profile of the beam, and pulse phase-shaping, where a given polarization dynamics can be programmed in the pulse. The latter is usually obtained using complicated setups limited to particular and extreme laboratory conditions. On the opposite, our proposal relies on the universal mechanism of Rabi oscillations that can be implemented in a large variety of platforms to cover a wide span of timescales, from attoseconds with plexcitons to milliseconds with nanomechanical oscillators and conceivably extendable to macroscopic timescales as well. This has numerous technological applications, that can be vividly illustrated by the case of the "lock-picking" excitation of an optical target sensible to one polarization only, which can be found by our pulse since it visits all the possible configurations. I have shown what exact sequence of pulses should be sent on the microcavity to bring it in the configuration that results in its emission swirling from two points (initial and final) on the Poincaré sphere.

The previous works were done in tight collaboration with experimentalists in Lecce, providing both input and feedback. I have also studied purely theoretical

aspects in Madrid, considering the formal and general problem of the propagation of free polariton wavepackets. This is a direct generalization of the problem of how a Gaussian wavepacket propagates under the dynamics of the simple Schrödinger equation, here with essentially the only addition that two coupled fields support the wavefunction. It might be surprising that even the Schrödinger equation itself kept in store nontrivial results such as Airy beams—free wavepackets accelerating without any applied force—till 1979. These results furthermore remained largely unnoticed for another three decades before they triggered a full field of Research on the dynamics of their propagation, with such striking applications as "particle snowblowers". In my own investigation, I have likewise observed several nontrivial features of the polariton dynamics, usually kept hidden behind more complex ingredients such as nonlinearities, pumping, reservoirs, etc. A non-negligible portion of the polariton literature reduce the problem to Gross-Pitaevskii equations, and are therefore in essence more related to cold atoms than to polaritons. My research has pinpointed the most salient feature of the polaritons: their non-parabolic dispersion, with a marked inflection point when the exciton and photon masses differ largely, which is the case experimentally. I have shown in closed-form solutions how a polariton wavepacket is bounded in its diffusion and cannot be jointly localised in space through both its excitonic and photonic component: localizing one field smears the other. In contrast, exact polariton plane-waves are possible. The polariton dispersion yields two concept of masses, one that rule its momentum, the other that rule its diffusion. While they merge into a common concept in the standard Schrödinger case, they compete in all possible combinations for polaritons. Most strikingly, when a wavepacket sits on the inflection point, its diffusing mass diverges and the polariton becomes shape-preserving. When it straddles over both sides of this point, it senses both a positive and negative diffusing mass, resulting in the packet going simultaneously backward and forward. As a result, a peculiar pattern of ripples is formed, leading to a concept of Self-Interfering Packet (SIP), that resembles very much the Airy beams, but being physical (normalized), not accelerating and self-shaping out of initial Gaussian wave packets. The combination of such a packet with Rabi oscillations leads to the formation of a striking honeycomb structure in space-time. I have also discussed briefly (in the introduction) the situation of high densities of excitation, leading to the formation of a "polariton backjet" which, also enjoying a rich and appealing phenomenology, is however, and in stark contradiction to the linear case, far from fully understood.

Finally, back to the linear dynamics and to a collaboration with experimentalists, I have discussed the dynamics of vortices in polaritons. The problem itself has been widely discussed before, but for polaritons as eigenstates, while I have considered the more general problem of vortices in arbitrary states of the coupled fields. In particular, the combination of Rabi oscillations with vortices leads to peculiar dynamics, with oscillations and accelerations of the cores, here again, all this happening in a non-interacting system (only powered by Rabi coupling). This led me to introduce the notion of Rabi-Orbit coupling, to bring together with its venerable counterpart of Spin-Orbit coupling. The vortices in both components

(exciton and photon) make a vortex molecule, whose binding is ruled by the Rabi coupling. The vortex and antivortex that constitute it have the same circulation (same sign in their respective phase space), but they are out of phase in the relative phase space, in contrast to a conventional vortex-antivortex pair. This reveals a more subtle structure of the vortices in such a case. The work is still in progress at the time of writing (the manuscript is in preparation) and the results summarized in this text are thus to be recorded as a snapshot of my understanding, that is called to be quickly updated.

In Conclusions, I have studied varied aspects—both experimental and theoretical—of the microcavity polaritons dynamics. I have focused on their linear dynamics since I have observed that much nontrivial physics remained to be studied even in this simplest of cases, with effects of proposing a new type of quasi-particle emerging out of the dynamics of coupled fields or of a new kind of light that takes all the states of polarization in time. I can safely close this concluding Chapter by stating that even in this framework, I have been far from exhausting the problematic and that many elegant and beautiful results have been left unexplored and lay dormant somewhere between two Bragg mirrors and a couple of Schrödinger equations.

Castellano

En esta tesis, he presentado los resultados de mi investigación durante los años 2013-2016 bajo la supervisión de Fabrice P. Laussy como parte de la ERC Starting Grant POLAFLOW, que ha implicado una colaboración estrecha con el grupo experimental de Daniele Sanvitto en Lecce (Italia). Mi campo de estudio ha sido la dinámica de polaritones en microcavidades, superposiciones de luz y materia en heteroestructuras semiconductoras. Estos sistemas pueden ser excitados por pulsos cortos de luz que crean paquetes de polaritones, cuya subsiguiente dinámica puede ser monitorizada en el tiempo gracias al escape continuo de fotones desde la cavidad (pues los polaritones tienen una vida media muy corta). Me he enfocado en la dinámica lineal de estos objetos, donde las no-linearidades que surgen de las interacciones partícula-partícula o de un reservorio de excitones pueden ser despreciadas o absorbidas como parámetros efectivos. Esto plantea el problema como el de la dinámica de dos campos bosónicos acoplados que, en el caso de los polaritones, difieren enormemente en su masa, lo cual resulta en una relación de dispersión peculiar.

Mi primer aporte ha sido el proporcionar una descripción cuantitativa de la dinámica lineal de los polaritones, en particular de sus oscilaciones de Rabi. Aunque el fenómeno parece muy simple en términos cualitativos, era desconocido hasta que nivel de precisión es capaz de describir las observaciones experimentales. Los experimentales de Lecce han podido plasmar con una gran precisión (cientos de femtosegundos) la dinámica espacio-temporal del campo en la cavidad tras ser excitado con pulsos cortos. He desarrollado un modelo de óptica cuántica para describir los parámetros de orden del campo excitónico y de cavidad, y he obtenido un

acuerdo esencialmente perfecto entre el modelo y los datos. Esto demuestra que incluso teniendo lugar en un sistema complejo de estado sólido, la dinámica de Rabi de los polaritones es de un carácter esencialmente fundamental, una vez que las variables del problema que uno tiene que considerar han sido bien entendidas y tenidas en cuenta. Estas son, aparte del obvio acoplo de Rabi entre los modos y su vida media, un término de pure-dephasing para los polaritones superiores y una tasa de bombeo incoherente para la fracción excitónica. El primero es un atributo bien conocido de los polaritones (la rama superior es mucho menos visible que la inferior), mientras que el segundo es de esperar en términos fenomenológicos. Mi fiteo a los datos permitieron demostrar que estas "complicaciones" son suficientes para describir todo lo que ocurre en el régimen lineal. También permitió cuantificar las tasas de decaimiento para cada uno de estos canales, demostrar el efecto de la mejora de la vida media de las oscilaciones de Rabi gracias a la reposición del reservorio, y explicar la pérdida del contraste en las oscilaciones en base a la evaporación de los polaritones superiores y no a la pérdida del acoplo fuerte. Otra aclaración realizada gracias a esta teoría es que la dinámica de polaritones bajo excitación pulsada es en realidad la de dos condensados acoplados, más que la de una superposición cuántica de luz y materia (lo que un polariton de hecho es al nivel de una sola partícula, tal como es comúnmente referido en la comunidad pese a que probablemente no se haya realizado nunca en el laboratorio hasta la fecha). Esto me llevó a clarificar que los polaritones son todavía "cebits" (sistemas de dos niveles efectivos clásicos), y no "qubits". Finalmente, el fit reveló que el láser usado para excitar se acopla tanto al campo excitónico como al fotónico, y no solo al segundo, como es universalmente asumido en la comunidad.

Este control y entendimiento profundo de la dinámica de los polaritones permite controlarlos coherentemente. La teoría puede conseguir cualquier secuencia de patrones, amplificando las oscilaciones, encendiendo y apagando las oscilaciones de Rabi, transfiriendo los condensados de una rama a la otra e incluso aniquilando completamente las partículas mediante interferencias destructivas entre el láser usado para la excitación y los campos polaritónicos. Sorprendentemente, esencialmente todas estas operaciones han sido implementadas en el laboratorio. Esto permitió añadir otro grado de libertad, la polarización, para implementar la idea, simple pero reveladora, de que combinando oscilaciones de Rabi de dos campos polarizados daría lugar a oscilaciones en la polarización. Aquí, el tiempo de vida finito de los polaritones superiores podría ser un activo más que una limitación, ya que permitiría obtener, aparte de meras oscilaciones en la polarización, un desplazamiento en la esfera de Poincarè. Con una elección cuidadosa de los parámetros, he demostrado cómo esta idea permite implementar un haz completo de Poincarè en tiempo, es decir, luz que adquiere todos los estados de polarización durante la duración de cada pulso. Esta luz junta dos conceptos previamente desconectados: el haz completo de Poincarè, que toma todos los estados de polarización a lo largo de su perfil espacial, y moldeo de fase pulsado, en el que una dinámica de polarización determinada puede ser programada en un pulso. El segundo se obtiene normalmente usando configuraciones complicadas,

limitadas a condiciones de laboratorio particulares y extremas. Por el contrario, nuestra propuesta se basa en el mecanismo universal de las oscilaciones de Rabi, que puede ser implementado en una gran variedad de plataformas para abarcar así un gran abanico de escalas temporales, desde attosegundos para los plexcitones a los milisegundos con osciladores nanomecánicos, siendo incluso concebible su extensión a escalas de tiempo macroscópicas. Todo esto tiene numerosas aplicaciones tecnológicas, que pueden ser vivamente ilustradas por el ejemplo de la excitación "ganzúa" de un blanco óptico sensible a una única polarización, la cual puede ser encontrada por nuestro pulso ya que éste explora todas las polarizaciones posibles. He mostrado cuál debe ser la secuencia exacta de pulsos que debe ser mandada a la microcavidad para llevarla a la configuración que resulta en una emisión que gira entre dos puntos (inicial y final) de la esfera de Poincarè.

Estos trabajos fueron realizados en estrecha colaboración con los experimentales en Lecce, intercambiando resultados y opiniones. He estudiado también aspectos puramente teóricos en Madrid, considerando el problema formal y general de la propagación libre de paquetes de polaritones. Ésta es una generalización del problema de cómo un paquete gaussiano se propaga bajo la dinámica de una ecuación de Schrödinger simple, donde el único elemento extra es que la función de onda se apoya en dos campos acoplados. Podría ser sorprendente que incluso la propia ecuación de Schrödinger mantuviera ocultos algunos resultados no triviales tales como los haces de Airy (paquetes libres que se aceleran sin ninguna fuerza aplicada) hasta 1979. Además, estos resultados permanecieron en gran medida inadvertidos durante otras tres décadas hasta desencadenar el nacimiento de un campo entero de investigación girando en torno a la dinámica de su propagación, con aplicaciones tan sorprendentes como las "máquinas quitanieves de partículas". En mi propia investigación, he observado también algunas características no triviales de la dinámica de polaritones que normalmente se mantienen ocultas tras otros ingredientes más complejos como nolinearidades, bombeo, reservorios, etc. Una parte no despreciable de la literatura de polaritones reduce el problema a ecuaciones de Gross-Pitaevskii, y está por lo tanto más relacionada con átomos fríos que con polaritones. Mi investigación ha ubicado la característica más prominente de los polaritones: su relación de dispersión no parabólica, con un punto de inflexión marcado cuando las masas del excitón y del fotón son muy diferentes, lo cual es el caso experimentalmente. He demostrado con soluciones cerradas como un paquete de polaritones está acotado en su difusión y no puede ser localizado en el espacio a través de su componente excitónica y fotónica conjuntamente: localizando uno de los campos deslocalizamos el otro. Sin embargo, las ondas planas exactas de polaritones son posibles. La dispersión de los polaritones da lugar a dos diferentes conceptos de masa, una que gobierna su momento, y otra que gobierna su difusión. Mientras que ambas se unen en un único concepto en el caso estándar de la ecuación de Schrödinger, compiten en todas sus posibles combinaciones en el caso de los polaritones. Sorprendentemente, cuando un paquete de ondas se encuentra en el punto de inflexión, su masa difusiva diverge y el polaritón pasa a mantener su forma. Cuando se extiende a ambos lados de este punto, siente

una masa difusiva tanto positiva como negativa, resultando en un paquete que se difunde simultáneamente hacia adentro y hacia afuera. Esto produce un patrón regular de ondulaciones, dando lugar al concepto de Paquete Auto Interferente (SIP por sus siglas en inglés), con gran parecido al haz de Airy, con la diferencia de ser físico (normalizado), sin aceleración y formándose solo a partir de un paquete gaussiano. La combinación de uno de estos paquetes con las oscilaciones de Rabi da lugar a la formación de una estructura sorprendente de panal de abeja en el espacio-tiempo. También he discutido brevemente (en la introducción) la situación de altas densidades de excitación, dando lugar a la formación de un "backjet" polaritónico el cual, aun demostrando una fenomenología rica e interesante, aún dista de ser entendido completamente.

Finalmente, volviendo a la dinámica lineal y a la colaboración con experimentales, he discutido la dinámica de vórtices de polaritones. Éste problema ha sido estudiado ampliamente con anterioridad, pero con los polaritones como autoestados, mientras que yo he considerado el problema más general de vórtices en campos acoplados en estados arbitrarios. En particular, la combinación de oscilaciones de Rabi con los vórtices da lugar a una dinámica peculiar, con oscilaciones y aceleraciones de sus centros, y de nuevo considerando sólo una dinámica lineal (solo alimentada por el acoplo de Rabi). Esto me llevó a introducir la idea del acoplo Rabi-Órbita, en contraste con la correspondiente (y venerable) idea del acoplo Espín-Órbita. Los vórtices en ámbos componentes (excitón y fotón) convierten al vórtice en una molécula, cuya ligadura viene dominada por el acoplo de Rabi. El vórtice y antivórtice que la constituyen tienen la misma circulación (el mismo signo en su respectivo espacio de fase), pero están fuera de fase en su espacio de fase relativo, en contraste con el par vórtice-antivórtice convencional. Esto revela una estructura de los vórtices más sutil. Éste trabajo está aún en progreso al momento de escribir (el manuscrito está en preparación), por lo que los resultados presentados en este texto deben ser considerados sólo como una fotografía de mi entendimiento actual, el cual con toda seguridad será revisado pronto.

En conclusión, he estudiado varios aspectos (experimentales y teóricos) de la dinámica de polaritones en microcavidades. Me he enfocado en la dinámica lineal, ya que he observado que incluso en los casos más simples quedaba mucha física no trivial por estudiar. Esto ha dado lugar a resultados como la propuesta de un nuevo tipo de cuasi partícula que emerge de la dinámica de dos campos acoplados, o de un nuevo tipo de luz que toma todos los estados posibles de polarización en el tiempo. Puedo cerrar este capítulo conclusivo con la seguridad de que, incluso en este marco, he estado lejos de agotar toda la problemática presente, y que muchos resultados de extrema belleza y elegancia permanecen inexplorados, yaciendo durmientes en algún rincón entre dos espejos de Bragg y un par de ecuaciones de Schrödinger.

List of publications

Regular Journals

1. L. Dominci, **D. Colas**, S. Donati, J. P. Restrepo Cuartas, M. de Girogi, D. Ballarini, G. Guirales, J. C. Lopez Carreño, A. Bramati, G. Gigli, E. del Valle, F. P. Laussy and D. Sanvitto, *"Ultrafast Control and Rabi Oscillations of Polaritons"*, Phys. Rev. Lett. **113**, 226401 (2014).

2. **D. Colas**, L. Dominci, S. Donati, A. A. Pervishko, T. C. H. liew, I. A. Shelykh, D. Ballarini, M. de Girogi, A. Bramati, G. Gigli, E. del Valle, F. P. Laussy, A. V. Kavokin and D. Sanvitto, *"Polarization shaping of Poincaré beams by polariton oscillations"*, Light Sci. Appl. **4**, e350 (2015).

3. L. Dominci, M. Petrov, M. Matuszewski, D. Ballarini, M. de Girogi,**D. Colas**, E. Cancellieri, B. S. Fernández, A. Bramati, G. Gigli, A. V. Kavokin, F. P. Laussy and D. Sanvitto, *"Real-space collapse of a polariton condensate"*, Nat. Comm. **6**, 8993 (2015).

4. **D. Colas** and F. P. Laussy, *"Self-Interfering Wave Packets"*, Phys. Rev. Lett. **116**, 026401 (2016).

Computer code

6. **D. Colas**, E. del Valle and F. P. Laussy, *Polarized Polariton Fields on the Poincaré Sphere*, Wolfram Demonstrations Project, http://demonstrations.wolfram.com (2015).

Bibliography

[1] Savvidis, P. G. & Lagoudakis, P. G. Teaching polaritons new tricks. *Semiconductors* **18**, 311 (2003).

[2] Kavokin, A., Baumberg, J. J., Malpuech, G. & Laussy, F. P. *Microcavities* (Oxford University Press, 2011), 2 edn.

[3] Hopfield, J. J. Theory of the contribution of excitons to the complex dielectric constant of crystals. *Phys. Rev.* **112**, 1555 (1958).

[4] Christopoulos, S. *et al.* Room-temperature polariton lasing in semiconductor microcavities. *Phys. Rev. Lett.* **98**, 126405 (2007).

[5] Weisbuch, C., Nishioka, M., Ishikawa, A. & Arakawa, Y. Observation of the coupled exciton-photon mode splitting in a semiconductor quantum microcavity. *Phys. Rev. Lett.* **69**, 3314 (1992).

[6] Savvidis, P. G. *et al.* Angle-resonant stimulated polariton amplifier. *Phys. Rev. Lett.* **84**, 1547 (2000).

[7] Kasprzak, J. *et al.* Bose–Einstein condensation of exciton polaritons. *Nature* **443**, 409 (2006).

[8] Vladimirova, M. *et al.* Polariton-polariton interaction constants in microcavities. *Phys. Rev. B* **82**, 075301 (2010).

[9] Larionova, Y., Stolz, W. & Weiss, C. O. Optical bistability and spatial resonator solitons based on exciton-polariton nonlinearity. *Opt. Lett.* **33**, 321 (2008).

[10] Sanvitto, D. *et al.* Persistent currents and quantized vortices in a polariton superfluid. *Nat. Phys.* **6**, 527 (2010).

[11] Amo, A. *et al.* Polariton superfluids reveal quantum hydrodynamic solitons. *Science* **332**, 1167 (2011).

[12] Flayac, H., Solnyshkov, D. D. & Malpuech, G. Oblique half-solitons and their generation in exciton-polariton condensates. *Phys. Rev. B* **83**, 193305 (2011).

[13] Hivet, R. *et al.* Half-solitons in a polariton quantum fluid behave like magnetic monopoles. *Nat. Photon.* **8**, 724 (2012).

[14] Egorov, O. A., Skryabin, D. V., Yulin, A. V. & Lederer, F. Bright cavity polariton solitons. *Phys. Rev. Lett.* **102**, 153904 (2009).

[15] Sich, M. *et al.* Observation of bright polariton solitons in a semiconductor microcavity. *Nat. Photon.* **6**, 50 (2012).

[16] Sich, M. *et al.* Effects of spin-dependent interactions on polarization of bright polariton solitons. *Phys. Rev. Lett.* **112**, 046403 (2014).

[17] Cilibrizzi, P. *et al.* Linear wave dynamics explains observations attributed to dark solitons in a polariton quantum fluid. *Phys. Rev. Lett.* **113**, 103901 (2015).

[18] Amo, A. *et al.* Comment on "linear wave dynamics explains observations attributed to dark solitons in a polariton quantum fluid". *Phys. Rev. Lett.* **115**, 089401 (2015).

[19] Pitaevskii, L. & Stringari, S. *Bose-Einstein Condensation* (Oxford University Press, 2003).

[20] Cilibrizzi, P. *et al.* Reply. *Phys. Rev. Lett.* **115**, 089402 (2015).

[21] Gamayun, O., Bezvershenko, Y. & Cheianov, V. Fate of a gray soliton in a quenched bose-einstein condensate. *Phys. Rev. A* **91**, 031605 (2015).

[22] Franchini, F., Gromov, A., Kulkarni, M. & Trombettoni, A. Universal dynamics of a soliton after an interaction quench. *J. Phys. A.: Math. Gen.* **48**, 28 (2015).

[23] Pal, S. & Bhattacharjee, J. K. Wave packet dynamics for gross–pitaevskii equation in one dimension: Dependence on initial conditions. *Int. J. Mod. Phys. B* **29**, 1550216 (2015).

[24] Pinsker, F. & Flayac, H. Bright solitons in non-equilibrium coherent quantum matter. *Proc. Roy. Soc. A* **472**, 2185 (2016).

[25] Javanainen, J. & Ruostekoski, J. Symbolic calculation in development of algorithms: split-step methods for the gross–pitaevskii equation. *J. Phys. A.: Math. Gen.* **39**, 12 (2006).

[26] Hamner, C., Chang, J. J., Engels, P. & Hoefer, M. A. Generation of dark-bright soliton trains in superfluid-superfluid counterflow. *Phys. Rev. Lett.* **106**, 065302 (2011).

[27] Pinsker, F. & Flayac, H. On-demand dark soliton train manipulation in a spinor polariton condensate. *Phys. Rev. Lett.* **112**, 140405 (2014).

[28] Zhang, Y. *et al.* Interactions of airy beams, nonlinear accelerating beams, and induced solitons in kerr and saturable nonlinear media. *Opt. Express* **22**, 7160 (2014).

[29] Rabi, I. I. Space quantization in a gyrating magnetic field. *Phys. Rev.* **51**, 652 (1937).

[30] Spreeuw, R. J. C., van Druten, N. J., Beijersbergen, M. W., Eliel, E. R. & Woerdman, J. P. Classical realization of a strongly driven two-level system. *Phys. Rev. Lett.* **65**, 2642 (1990).

[31] Faust, T., Rieger, J., Seitner, M. J., Kotthaus, J. P. & Weig, E. M. Coherent control of a classical nanomechanical two-level system. *Nat. Phys.* **9**, 485 (2013).

[32] Zhu, Y. *et al.* Vacuum Rabi splitting as a feature of linear-dispersion theory: Analysis and experimental observations. *Phys. Rev. Lett.* **64**, 2499 (1990).

[33] Khitrova, G., Gibbs, H. M., Kira, M., Koch, S. W. & Scherer, A. Vacuum Rabi splitting in semiconductors. *Nat. Phys.* **2**, 81 (2006).

[34] Wouters, M. & Carusotto, I. Excitations in a nonequilibrium Bose–Einstein condensate of exciton polaritons. *Phys. Rev. Lett.* **99**, 140402 (2007).

[35] Solnyshkov, D. D., Terças, H., Dini, K. & Malpuech, G. Hybrid boltzmann–gross-pitaevskii theory of bose-einstein condensation and superfluidity in open driven-dissipative systems. *Phys. Rev. A* **89**, 033626 (2014).

[36] Demirchyan, S., Chestnov, I., Alodjants, A., Glazov, M. & Kavokin, A. Qubits based on polariton rabi oscillators. *Phys. Rev. Lett.* **112**, 196403 (2014).

[37] Spreeuw, R. J. C. A classical analogy of entanglement. *Found. Phys.* **28**, 361 (1998).

[38] Carreño, J. L., Muñoz, C. S., Sanvitto, D., del Valle, E. & Laussy, F. Exciting polaritons with quantum light. *Phys. Rev. Lett.* **115**, 196402 (2015).

[39] Scully, M. O. & Zubairy, M. S. *Quantum optics* (Cambridge University Press, 2002).

[40] Martín, M., Ballarini, D., Amo, A., Viña, L. & André, R. Dynamics of polaritons resonantly created at the upper polariton branch. *Superlatt. Microstruct.* **41**, 328 (2007).

[41] Lin, S.-C., Chen, J.-R. & Lu, T.-C. Broadening of upper polariton branch in GaAs, GaN, and ZnO semiconductor microcavities. *Appl. Phys. B* **103**, 137 (2011).

[42] Husimi, K. Some formal properties of the density matrix. *Proc. Phys. Math. Soc. Jpn* **22**, 264 (1940).

[43] Dominici, L. *et al.* Real-space collapse of a polariton condensate. *Nat. Comm.* **6**, 8993 (2015).

[44] Dominici, L. *et al.* Ultrafast control and Rabi oscillations of polaritons. *Phys. Rev. Lett.* **113**, 226401 (2014).

[45] Levenberg, K. A method for the solution of certain problems in least squares. *Quart. Appl. Math.* **2**, 164 (1944).

[46] Marquardt, D. An algorithm for least-squares estimation of nonlinear parameters. *SIAM J. Appl. Math.* **11**, 431 (1963).

[47] Brent, R. P. *Algorithms for Minimization without Derivatives* (Dover, 1973).

[48] Savona, V. & Weisbuch, C. Theory of time-resolved light emission from polaritons in a semiconductor microcavity under resonant excitation. *Phys. Rev. B* **54**, 10835 (1996).

[49] Chestnov, I., Demirchyan, S. S., Alodjants, A., Rubo, Y. G. & Kavokin, A. Permanent rabi oscillations in coupled exciton-photon systems with pt -symmetry. *Scientific Report* **6**, 19551 (2016).

[50] Voronova, N. S., Elistratov, A. A. & Lozovik, Y. E. Detuning-controlled internal oscillations in an exciton-polariton condensate. *Phys. Rev. Lett.* **115**, 186402 (2015).

[51] Brixner, T. & Gerber, G. Femtosecond polarization pulse shaping. *Opt. Lett.* **26**, 557 (2001).

[52] Beckley, A. M., Brow, T. G. & Alonso, M. A. Full poincaré beams. *Opt. Express* **10**, 10777 (2010).

[53] Zhuang, Z., Suh, S. W. & Patel, J. S. Polarization controller using nematic liquid crystals. *Opt. Lett.* **24**, 694 (1997).

[54] Brixner, T. *et al.* Quantum control by ultrafast polarization shaping. *Phys. Rev. Lett.* **92**, 208301 (2004).

[55] Aeschlimann, M. *et al.* Adaptive subwavelength control of nano-optical fields. *Nature* **446**, 301 (2007).

[56] Köhler, J., Wollenhaupt, M., Bayer, T., Sarpe, C. & Baumert, T. Zeptosecond precision pulse shaping. *Opt. Express* **19**, 11638 (2011).

[57] Youngworth, K. S. & Brown, T. G. Focusing of high numerical aperture cylindrical-vector beams. *Opt. Express* **7**, 77 (2000).

[58] Chen, H. *et al.* Generation of vector beam with space-variant distribution of both polarization and phase. *Opt. Lett.* **36**, 3179 (2011).

[59] Beckley, A. M., Brow, T. G. & Alonso, M. A. Full poincaré beams ii: partial polarization. *Opt. Express* **20**, 9357 (2012).

[60] Zhan, Q. Cylindrical vector beams: from mathematical concepts to applications. *Advances in Optics and Photonics* **1**, 57 (2009).

[61] del Valle, E. *Microcavity Quantum Electrodynamics* (VDM Verlag, 2010).

[62] Steger, M. *et al.* Long-range ballistic motion and coherent flow of long-lifetime polaritons. *Phys. Rev. B* **88**, 235314 (2013).

[63] Golubev, N. V. & Kuleff, A. I. Control of populations of two-level systems by a single resonant laser pulse. *Phys. Rev. A* **90**, 035401 (2014).

[64] Abasahl, B., Dutta-Gupta, S., Santschi, C. & Martin, O. J. F. Coupling strength can control the polarization twist of a plasmonic antenna. *Nano Lett.* **13**, 4575 (2013).

[65] Schlather, A. E., Large, N., Urban, A. S., Nordlander, P. & Halas, N. J. Near-field mediated plexcitonic coupling and giant Rabi splitting in individual metallic dimers. *Nano Lett.* **13**, 3281 (2013).

[66] Cardano, F. *et al.* Polarization pattern of vector vortex beams generated by q-plates with different topological charges. *App. Optics* **51**, C1 (2012).

[67] She, A. & Capasso, F. Parallel polarization state generation. *Scientific Report* **6**, 26019 (2016).

[68] Berry, M. V. & Balazs, N. L. Nonspreading wave packets. *Am. J. Phys.* **47**, 264 (1979).

[69] Siviloglou, G. A., Broky, J., Dogariu, A. & Christodoulides, D. N. Observation of accelerating Airy beams. *Phys. Rev. Lett.* **99**, 213901 (2007).

[70] Baumgartl, J., Mazilu, M. & Dholakia, K. Optically mediated particle clearing using Airy wavepackets. *Nat. Photon.* **2**, 675 (2008).

[71] Zhang, P. *et al.* Plasmonic airy beams with dynamically controlled trajectories. *Opt. Lett.* **16**, 3191 (2011).

[72] Zhang, P. *et al.* Nonparaxial Mathieu and Weber accelerating beams. *Phys. Rev. Lett.* **109**, 193901 (2012).

[73] Chremmos, I. D., Chen, Z., Christodoulides, D. N. & Efremidis, N. K. Bessel-like optical beams with arbitrary trajectories. *Opt. Lett.* **37**, 5003 (2012).

[74] Zhao, J. *et al.* Observation of self-accelerating bessel-like optical beams along arbitrary trajectories. *Opt. Lett.* **38**, 498 (2013).

[75] Kaminer, I., Nemirovsky, J., Makris, K. G. & Segev, M. Self-accelerating beams in photonic crystals. *Opt. Express* **21**, 8886 (2013).

[76] Carusotto, I. & Ciuti, C. Quantum fluids of light. *Rev. Mod. Phys.* **85**, 299 (2013).

[77] Grosso, G. & Parravicini, G. P. *Solid State Physics* (Academic Press, 2000).

[78] Larson, J., Salo, J. & Stenholm, S. Effective mass in cavity QED. *Phys. Rev. A* **72**, 013814 (2005).

[79] Márk, G. I. Analysis of the spreading Gaussian wavepacket. *Eur. Phys. J. B* **18**, 247 (1997).

[80] Colas, D. & Laussy, F. P. Self-interfering wave packets. *Phys. Rev. Lett.* **116**, 026401 (2016).

[81] Liew, T. C. H., Rubo, Y. G. & Kavokin, A. V. Generation and dynamics of vortex lattices in coherent exciton-polariton fields. *Phys. Rev. Lett.* **101**, 187401 (2008).

[82] Debnath, L. & Shah, F. A. *Wavelet Transforms and Their Applications* (Birkhăuser, 2015), 2 edn.

[83] Baker, C. H., Jordan, D. A. & Norris, P. M. Application of the wavelet transform to nanoscale thermal transport. *Phys. Rev. B* **86**, 104306 (2012).

[84] Dragoman, D. Phase-space interferences as the source of negative values of the wigner distribution function. *J. Opt. Soc. Am.* **17**, 2481 (2000).

[85] Wertz, E. *et al.* Spontaneous formation and optical manipulation of extended polariton condensates. *Nat. Phys.* **6**, 860 (2010).

[86] Daskalakis, K., Maier, S. & Kéna-Cohen, S. Spatial coherence and stability in a disordered organic polariton condensate. *Phys. Rev. Lett.* **115**, 035301 (2015).

[87] Garanovich, I. L., Longhi, S., Sukhorukova, A. A. & Kivshar, Y. S. Light propagation and localization in modulated photonic lattices and waveguides. *Phys. Rep.* **518**, 1 (2012).

[88] Gerace, D. & Andreani, L. C. Quantum theory of exciton-photon coupling in photonic crystal slabs with embedded quantum wells. *Phys. Rev. B* **75**, 235325 (2007).

[89] Huang, S. C., Kato, M., Kuramochi, E., Lee, C. P. & Notomi, M. Time-domain and spectral-domain investigation of inflection-point slow-light modes in photonic crystal coupled waveguides. *Opt. Express* **15**, 3543 (2007).

[90] Amo, A. *et al.* Collective fluid dynamics of a polariton condensate in a semiconductor microcavity. *Nature* **457**, 291 (2009).

[91] Voronych, O., Buraczewski, A., Matuszewski, M. & Stobińska, M. Exciton-polariton x-waves in a microcavity. *http://arxiv.org/abs/1510.05429* (2015).

[92] McMorran, B. J. *et al.* Electron vortex beams with high quanta of orbital angular momentum. *Science* **6014**, 192 (2011).

[93] Blatter, G. *et al.* Vortices in high-temperature superconductors. *Rev. Mod. Phys.* **66**, 1125 (1994).

[94] Matthews, M. R. *et al.* Vortices in a Bose–Einstein condensate. *Phys. Rev. Lett.* **83**, 2498 (1999).

[95] Weiler, C. N. *et al.* Spontaneous vortices in the formation of bose–einstein condensates. *Nature* **455**, 948 (2008).

[96] Abo-Shaeer, J. R., Raman, C., Vogels, J. M. & Ketterle, W. Observation of vortex lattices in bose-einstein condensates. *Science* **292**, 476 (2001).

[97] Anderson, B. P., Haljan, P. C., Wieman, C. E., & Cornell, E. A. Vortex precession in bose-einstein condensates: Observations with filled and empty cores. *Phys. Rev. Lett.* **85**, 2857 (2000).

[98] Yao, A. M. & Padgett, M. J. Orbital angular momentum: origins, behavior and applications. *Advances in Optics and Photonics* **3**, 161 (2011).

[99] Franke-Arnold, S., Allen, L. & Padgett, M. Advances in optical angular momentum. *Laser Photon. Rev.* **2**, 299 (2008).

[100] Uchida, M. & Tonomura, A. Generation of electron beams carrying orbital angular momentum. *Nature* **464**, 737 (2010).

[101] Lagoudakis, K. G. *et al.* Quantized vortices in an exciton-polariton condensate. *Nat. Phys.* **4**, 706 (2008).

[102] Lagoudakis, K. G. *et al.* Observation of half-quantum vortices in an exciton-polariton condensate. *Science* **326**, 974 (2009).

[103] Rubo, Y. G. Half vortices in exciton polariton condensates. *Phys. Rev. Lett.* **99**, 106401 (2007).

[104] Dominici, L. *et al.* Vortex and half-vortex dynamics in a nonlinear spinor quantum fluid. *Sci. Adv.* **1** (2015).

[105] Leach, J. *et al.* Quantum correlations in optical angle–orbital angular momentum variables. *Science* **5992**, 662 (2010).

[106] Yan, Y. *et al.* High-capacity millimetre-wave communications with orbital angular momentum multiplexing. *Nat. Comm.* **5**, 4876 (2014).

[107] Wang, J. *et al.* Terabit free-space data transmission employing orbital angular momentum multiplexing. *Nat. Phys.* **6**, 488 (2014).

[108] Franchetti, G., Berloff, N. G. & Baumberg, J. J. Exploiting quantum coherence of polaritons for ultra sensitive detectors. *http://arxiv.org/abs/1210.1187* (2012).